Electron paramagnetic resonance approaches to study biologically relevant reactions: examples from amyloid aggregation to enzymes

Passerini, L.

Electron Paramagnetic Resonance Approaches to Study Biologically Relevant Reactions: Examples from Amyloid Aggregation to Enzymes

PhD Thesis

Leonardo Passerini

Electron Paramagnetic Resonance Approaches to Study Biologically Relevant Reactions: Examples from Amyloid Aggregation to Enzymes

Proefschrift

ter verkrijging van

de graad van doctor aan de Universiteit Leiden,

op gezag van rector magnificus prof.dr.ir. H. Bijl,

volgens besluit van het college voor promoties

te verdedigen op dinsdag 2 september 2025

klokke 16:00 uur

door

Leonardo Passerini

geboren te Trento, Italië

in 1994

Promotores	dr. M. Huber
	Prof.dr. M. Ubbink
Promotiecommissie	dr. Marco Bortolus (Università degli Studi di Padova)
	Prof.dr. B. de Bruin (Universitat van Amsterdam)
	Prof.dr. S.J. van der Molen
	Prof.dr. J.M. van Ruitenbeek
	Prof.dr. T. Schmidt
	dr. A.S. Wentink

HOLLAND RESEARCH SCHOOL
OF MOLECULAR CHEMISTRY

The work presented in this thesis was funded by the Netherlands Organization for Scientific Rsearch (NWO/OCW).

An electronic version of this thesis is available at https://scholarlypublications.universitetleiden.nl/.

Table of Contents

Chapter 1.
Introduction

Electron Paramagnetic Resonance (EPR), also known as Electron Spin Resonance (ESR), is a powerful technique to study materials with unpaired electrons. It was first observed by the Soviet physicist Yevgeny Zavoisky in 1944 [1, 2], and since then has become an essential tool for probing the electronic and structural properties of paramagnetic systems.

EPR is a magnetic resonance spectroscopy particularly valuable for studying paramagnetic ions, organic radicals, transition metal complexes and biological macromolecules. Since its discovery, EPR rapidly expanded its applications and is now well-established across diverse fields such as solid state physics, biochemistry, chemical catalysis, environmental sciences, and many more.

A typical commercial EPR spectrometer consists of a magnet, microwave resonator, controlling console, and microwave components, that are necessary for excitation of the sample and detection of the signal. The information obtained from the sample depends on the field strength and microwave radiation frequency, as measurements at different fields and frequencies can highlight distinct aspects of the electronic structure. For the studies shown in this thesis, both a commercial and a homebuilt spectrometer [3] were used, that are shown in figure 1.

In this thesis, the goal is to explore EPR approaches to improve the study of biochemically relevant problems, and to learn about the mechanisms of biochemical reactions. One important problem is amyloid aggregation, where difficult-to-study intermediates are considered active in neurodegenerative diseases. In chapter 3 we explore in-depth how EPR can contribute to this research. In the course of the investigation related to chapter 3, we encountered a problem that has been around for at least four decades of spin-labelling EPR, which we were able to solve in chapter 2. In all physiological events involving proteins that catalyze chemical reactions, so called enzymes, efficiency and specificity is determined by the reaction mechanism. Chapter 4 shows how a new method relying on very-high field EPR enables to determine a short-lived intermediate of such a reaction. In chapter 5, a model system is studied that targets distances in multi-spin systems expanding the technique to Cu(II) spins. Multispin interactions in Cu(II) and related spin systems are important in many biological systems.

In this introductory chapter, the fundamental concepts of EPR are presented, along with the necessary information to understand the scientific studies in chapters 2 through 5. The background of EPR is described in several monographies [4-6]. Here specifically [6] is used, in addition to the references mentioned for specific points.

Figure 1. Spectrometer used for electron paramagnetic resonance (EPR). Left: Bruker Elexsys E580 9 GHz EPR spectrometer, operating magnetic field 0-0.5 T. Right: Homebuilt 275 GHz EPR spectrometer, operating magnetic field 0-11 T. Here the magnet is a superconducting coil immersed in liquid helium.

1.1 The Spin Hamiltonian

The information obtained with EPR can be described by the spin Hamiltonian, which represents the total energy of the spin-system and provides the theoretical support for interpreting EPR spectra. The spin Hamiltonian relevant to this thesis for a two electron- one nucleus system can be expressed as:

$$\hat{H} = \sum_{n=1,2}(\mu_B \boldsymbol{g}\boldsymbol{B_0}\widehat{\boldsymbol{S}_n} + \hat{\boldsymbol{I}}\boldsymbol{A}_n\widehat{\boldsymbol{S}_n}) + \widehat{\boldsymbol{S}_1}\boldsymbol{D}\widehat{\boldsymbol{S}_2} + J\widehat{\boldsymbol{S}_1}\widehat{\boldsymbol{S}_2} \quad (1)$$

Here, $\mu_B \boldsymbol{g}\boldsymbol{B_0}\widehat{\boldsymbol{S}_n}$ is the electron Zeeman interaction between the unpaired electron and the applied magnetic field $\mathbf{B_0}$, with $\hat{\boldsymbol{S}}$, the electron spin vector operator and **g** the g-tensor. $\hat{\boldsymbol{I}}\boldsymbol{A}_n\widehat{\boldsymbol{S}_n}$ is the hyperfine interaction between the unpaired electrons and a coupled magnetic nucleus, with $\hat{\boldsymbol{I}}$, the nuclear spin vector operator and $\boldsymbol{A}_n$ the hyperfine tensors. $\widehat{\boldsymbol{S}_1}\boldsymbol{D}\widehat{\boldsymbol{S}_2}$ and $J\widehat{\boldsymbol{S}_1}\widehat{\boldsymbol{S}_2}$ are the dipole-dipole and exchange interaction, respectively, between the unpaired electron and other nearby unpaired electrons. Here, **D** is the dipolar tensor and J the isotropic exchange interaction. The origin of these terms and their impact on the EPR spectrum is discussed in the following sub-chapters. It is convenient to describe these energy terms in frequency units. In this thesis, the hyperfine interaction **A**, dipole-dipole interaction **D**, and exchange interaction J will be given in units of Hz.

1.2 Continuous wave EPR and the Electron Zeeman Interaction

This section focuses on continuous wave EPR (CW-EPR), where the sample is continuously irradiated with microwaves while the field is varied. The foundation of EPR spectroscopy lies in the interaction of the magnetic dipole moment of the electron spin with an applied static magnetic field B_0. During a CW-EPR experiment, the magnetic field lifts the degenerancy between the spin-energy levels of the unpaired electron (spin quantum number $S = 1/2$, magnetic quantum number $m_s = \pm 1/2$ for an isolated electron) while the sample is irradiated with microwaves (figure 2). The microwave-radiation frequency is kept constant during the experiment. This allows to place the sample in a microwave resonator, whose dimension is tuned to the microwave-radiation wavelength. If the energy difference between the spin states matches the energy of the microwave radiation, a transition occurs, producing an EPR signal. In EPR, the selection rule for allowed transition is $\Delta m_s = \pm 1$, meaning that the magnetic quantum number m_s can only change by one unit. The EPR spectrum is usually displayed as the first derivative of an absorption signal due to the use of lock-in detection, see figure 2.

A fundamental parameter in EPR is the g-factor, which determines the proportionality between the magnetic field strength and the energy of the electron spin transition:

$$\hat{H} = \mu_B \boldsymbol{g} \boldsymbol{B_0} \hat{\boldsymbol{S}} \tag{2}$$

where $\hat{\boldsymbol{S}}$ is the electron spin vector operator, $\mathbf{g}$ the g-tensor, μ_B is the Bohr magneton, and $\boldsymbol{B_0}$ is the static magnetic field vector. The resonance condition for a free electron is given by:

$$h\nu = \mu_B g_e B_0 \tag{3}$$

where h is the Planck constant and ν is the microwave frequency. For a free electron, the g-value (g_e) is 2.0023. However, in atoms and molecules deviations arise that depend on the spin-orbit coupling and chemical environment. These effects cause the g-factor to deviate from g_e and to become anisotropic, meaning it varies depending on the molecule's orientation relative to the magnetic field. This anisotropy is expressed as the g-tensor $\mathbf{g}$. The principal values of $\mathbf{g}$ are [g_{xx} g_{yy} g_{zz}], can be resolved in solid-state EPR and single-crystal studies.

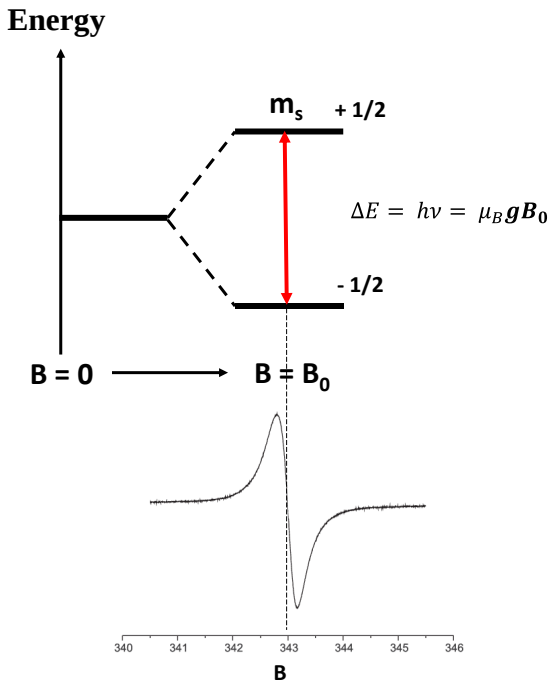

Figure 2. When the microwave-radiation frequency matches the energy difference between spin energy levels, a transition occurs. The EPR spectrum is depicted as first derivative of an absorption spectrum.

1.3 The Hyperfine Interaction

The hyperfine interaction is the interaction of the electron spin with the magnetic moment of a coupled nucleus. The degenerancy of the spin-energy levels of the nuclei is lifted in the presence of a magnetic field by the nuclear Zeeman interaction, generally weaker than the electron Zeeman interaction. The coupling of an unpaired electron with a nucleus with spin quantum number I, is given by the second term in the equation:

$$\hat{H} = \mu_B \boldsymbol{g} \boldsymbol{B_0} \hat{\boldsymbol{S}} + \hat{\boldsymbol{I}} \boldsymbol{A} \hat{\boldsymbol{S}} \quad (4)$$

where **A** is the hyperfine tensor with principal values [A_{xx} A_{yy} A_{zz}] and $\hat{\boldsymbol{I}}$ is the nuclear spin vector operator. The hyperfine interaction manifests in the EPR spectrum as a splitting of the signal in $(2I+1)$-lines. In figure 3, the energy-level scheme for an electron coupled to a ^{14}N ($I=1$) nucleus is shown, which results in the three transitions shown in red. In chapter 4 and 5, systems with copper ions are studied. The Cu(II) nucleus has nuclear spin quantum number $I=3/2$, and the signal is split into four lines. In this thesis, chapter 2 and 3 focus on measurements on liquid samples, where the anisotropy of **g**- and **A**-tensors is averaged by the rapid tumbling of the molecule in solution. For very fast motion, the observed g and A-values are $g_{iso}=\frac{g_{xx}+g_{yy}+g_{zz}}{3}$ and $A_{iso}=\frac{A_{xx}+A_{yy}+A_{zz}}{3}$. In chapter 4 and 5, samples in frozen solutions are measured. In this case, a powder pattern is observed, due to the statistical distribution of all possible orientations of the molecules in the magnetic field, which has characteristic features of the principal values of the tensors.

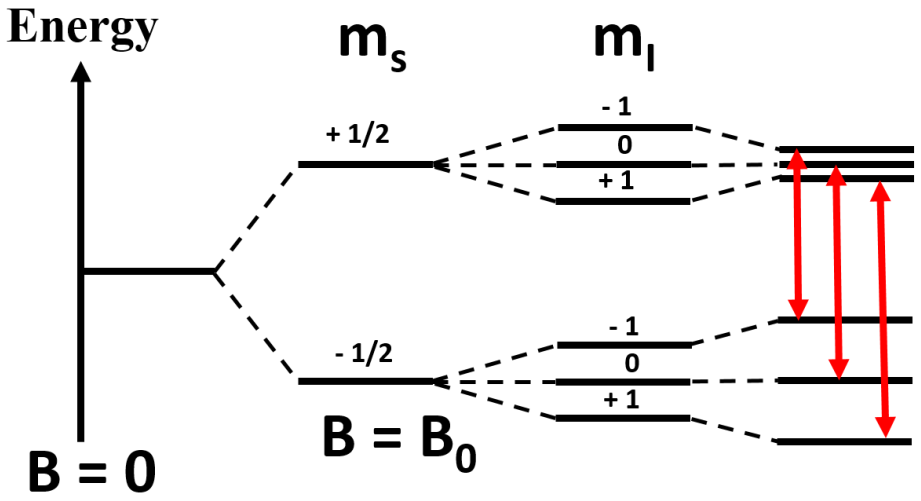

Figure 3. Energy level scheme for an electron coupled with a ^{14}N nucleus, I = 1. The magnetic field induces a splitting of the electron spin energy levels by electron Zeeman interaction, and a splitting between nuclear spin energy levels by nuclear Zeeman interaction. The hyperfine interaction results in 2I+1 transitions, shown in the figure as red arrows.

1.4 Dipole-Dipole Interaction

The electron-electron-dipole-dipole interaction in EPR arises when two unpaired electrons are sufficiently close that each one's magnetic field influences the other. This interaction depends on the distance between the two spins and on the orientation of the vector connecting them with respect to the field vector (see sub-section 1.8).
The spin Hamiltonian for a system with two interacting spins, describing the combined effects of the electron Zeeman, hyperfine, and dipole-dipole interactions, is expressed as:

$$\hat{H} = \sum_{n=1,2}(\mu_B \boldsymbol{g}\boldsymbol{B_0}\widehat{\boldsymbol{S}_n} + \hat{\boldsymbol{I}}\boldsymbol{A}_n\widehat{\boldsymbol{S}_n}) + \widehat{\boldsymbol{S}_1}\boldsymbol{D}\widehat{\boldsymbol{S}_2} \quad (5)$$

The dipole-dipole interaction is given by the **D**-tensor. Adopting the point-dipole approximation, the **D**-tensor has axial symmetry and is traceless ($D_{xx} + D_{yy} + D_{zz} = 0$).
In CW-EPR spectra, the dipole-dipole interaction can broaden or split signals depending on its magnitude and orientation relative to the magnetic field. In pulsed EPR experiments, such as those performed in chapter 5, the distance dependence of this interaction is used to extract inter-spin, intramolecular distances. The relation between **D** and the distance between the two spins is discussed in subchapter 1.8.

1.5 Exchange Interaction

The exchange interaction arises in systems containing two or more unpaired electrons and is described by $H_{exchange} = J\widehat{\boldsymbol{S}_1}\widehat{\boldsymbol{S}_2}$ with J being the isotropic exchange coupling constant. Unlike the dipole-dipole interaction, which depends on the spatial separation and orientation of spins, the exchange interaction is a quantum-mechanical effect related to the overlap of electron-spin wavefunctions [7].

In this thesis the exchange coupling interaction is relevant in chapter 2 and in chapter 4. In chapter 2, two exchange coupled nitroxides (see figure 4) are measured at room temperature. In this situation, the relative magnitude of J with respect to the isotropic hyperfine interaction A_{iso} of the electron spin with the nitrogen nuclei is the main factor to determine the EPR spectral shape. To use the same words as in [7], for strong exchange

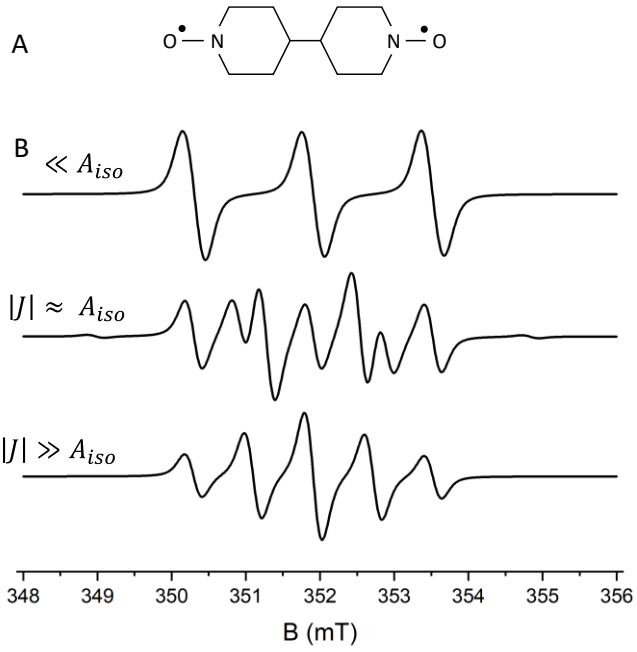

Figure 4. Exchange coupling in nitroxide biradicals. A) Example of a nitroxide biradical. The unpaired electrons are coupled to the ^{14}N nuclei. B) Simulated EPR spectra for different values of J, for A_{iso} = 45 MHz. B): top spectrum: for small magnitude of J, the spectrum is the same as a nitroxide mono-radical. Bottom: for large magnitude of J with respect to A_{iso}, a five line spectrum appear, while complicated line shapes appear when the values of J and A_{iso} are of similar magnitude.

coupling ($J>>A_{iso}$), "strong exchange results in the electron interacting equally with both ^{14}N nuclei, but for half of the time", resulting in the five-line spectrum in figure 4B (bottom). For weak exchange ($J<<A_{iso}$) the spectrum will be the same as a single nitroxide radical, and relatively complicated spectral shapes are observed when J and A_{iso} are of similar magnitude. An extensive overview of exchange coupled nitroxide systems is given in [8].

In chapter 4, a protein is studied in which a Cu(II) ($3d^9$, $S = {}^1/_2$) ion is coupled to an organic radical ($S = {}^1/_2$). The two unpaired electrons are coupled into a triplet state, and this example illustrates how a multi frequency EPR approach aids to fully characterize the spin

Hamiltonian. In figure 5 the energy-level scheme, EPR transitions and EPR spectra for an exchange-coupled Cu(II)-radical system are given (J = -19 GHz), for 9 GHz and 275 GHz EPR. For clarity, the hyperfine coupling to the Cu nucleus is not included in the simulation. At 9 GHz (figure 5A) the energy separation between singlet and triplet state is larger than the

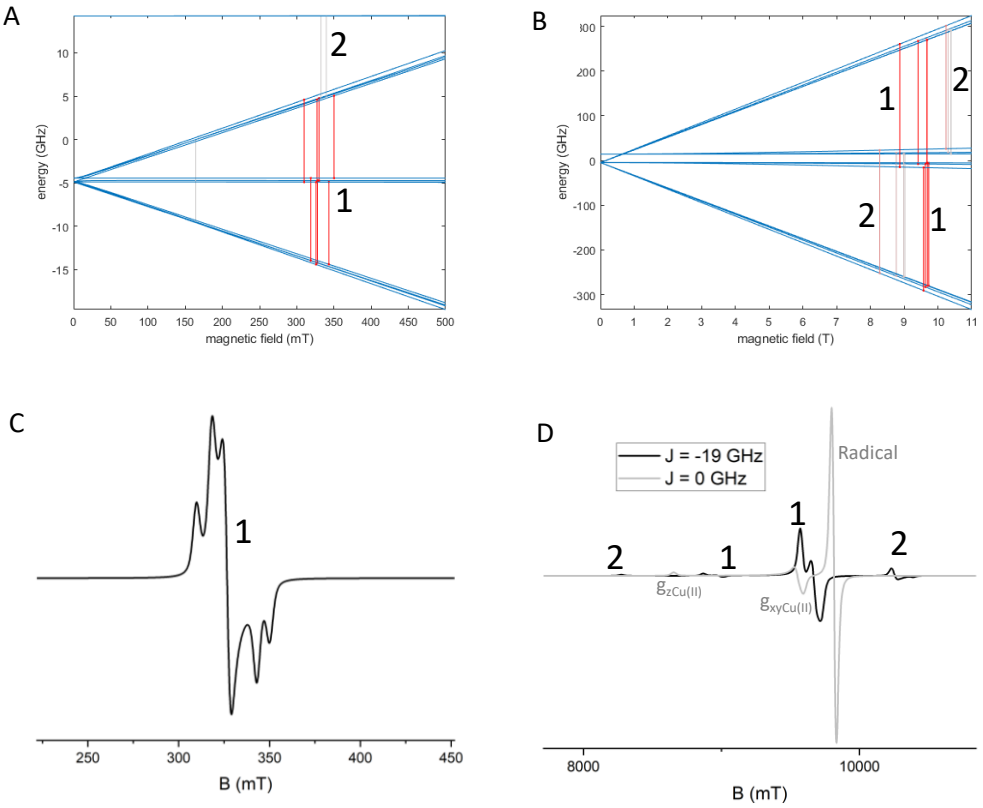

Figure 5. Effect of exchange coupling J on a coupled Cu(II)-organic radical system. The two unpaired electrons are coupled into a triplet ground state. A) Energy-level scheme for 9 GHz EPR. B) Energy-level scheme for 275 GHz EPR. C) 9 GHz EPR spectrum. D) 275 GHz EPR spectrum. Black: 275 GHz EPR for J = -19 GHz. Grey: 275 GHz EPR spectrum for J = 0 GHz. The spectrum is the one of a separated Cu(II) spectrum with axial symmetry (gx=gy≠gz) and an organic radical spectrum. In absence of magnetic field, the energy levels are separated into a triplet and a singlet ground state. These levels are mixed in the presence of a strong magnetic field. Transition 1: transition happening between the (original) triplet state sublevels. Transition 2: transition occurring between singlet and original triplet state. In the energy level scheme, the blue lines are the energy levels. The color of the transition lines indicates their probability: red: high, light grey: partially allowed

microwave quantum. Each triplet sublevel is split into four levels by the g-anisotropy, and the EPR spectrum has a complicated structure with six visible lines, and more lines hidden in the linewidth, but revealed in the energy levels scheme. In this condition, the magnitude of the exchange coupling is so large that values of |J| higher than 19 GHz would not affect the EPR spectrum further, as higher |J| would only introduce a larger separation of the triplet and singlet states, without affecting the transitions visible in the EPR spectrum. For this reason, the magnitude of J cannot be determined for such a system at 9 GHz EPR. The 275 GHz EPR energy level diagram is shown in figure 5B and the spectrum in figure 5D. In presence of a strong magnetic field, the triplet state is no longer a well-defined state as the energy levels undergo mixing. However, for simplicity, it is convenient to refer to them as "original triplet sublevels". It can be seen in figure 5C that transitions between these original triplet-sublevels and the singlet state are clearly visible in the 275 GHz EPR spectrum (transition 2 in figure 5B and 5D) whereas they do not appear in the 9 GHz EPR spectrum. The high-frequency spectrum is dominated by a signal split into two lines, situated between the transition of an isolated Cu(II) g_x and g_y resonance and an isolated organic radical, and a lower-intensity peak situated between the g_z of the Cu(II) and the radical (transitions labelled as 1). In this case the transitions (2) are diagnostic of the magnitude of the exchange coupling, which can be determined combining 9 and 275 GHz EPR. A multi-frequency EPR approach allows to fully characterize the spin Hamiltonian: It enables to determine the **D**-tensor principal values by 9 GHz EPR, and the J value by a combination of 9 and 275 GHz EPR.

1.6 EPR of Nitroxides and Site-directed-spin-labeling

Site-directed-spin-labeling (SDSL) is a technique that uses the attachment of spin labels to cysteine residues in proteins. In chapter 3, SDSL is used to study the aggregation of the intrinsically disordered protein α-Synuclein, a process that is linked to neurodegeneration (see below). In combination with site-directed mutagenesis, which allows to insert cysteine residues in selected protein sites while removing native unwanted ones, SDSL coupled with EPR allows to obtain site-specific information on biomolecules. The most commonly used spin labels are nitroxide radicals. The most well-known, MTSL ((1-Oxyl-2,2,5,5-tetramethylpyrroline-3-methyl) methanethiosulfonate), is shown in figure 6. In nitroxides, the unpaired electron spin interacts with the nitrogen (^{14}N, $I = 1$) nucleus, with an hyperfine coupling in the order of 100 MHz along the A_z direction and 10 MHz along A_x and A_y, which results in the characteristic splitting of the EPR signal into three lines. The EPR spectral shape of nitroxides at room temperature depends on their rotational correlation time τ_r (figure 6). The τ_r observed reflects the rotameric motion of the label and of the bonds connecting it to the protein backbone (figure 6B left). In specific circumstances, also the tumbling of the

molecule or the mobility of specific parts of the protein are influencing the spectral shape, especially when the molecular tumbling is faster than the rotameric motion of the label [9, 10] (figure 6B, right). In figure 6C, spectral simulations for different rotational correlation times show the relation between spectral shape and molecular motion. In the solid-state spectrum, figure 6C, the anisotropy of the A- and g-tensor is evident, while in liquid state the rapid tumbling of the free label in solution averages the anisotropy, resulting in the three-line spectrum for τ_r = 0.01 ns. When the label is attached to a protein, the tumbling will slow down, affecting the spectrum, because of the larger dimensions of the object. Site-specific structural and dynamical information in CW-EPR are obtained from the τ_r of the label. Changes in the spectral lineshape can give insights into interaction with partners, conformational changes, or environmental effects [11-14]. In chapter 3, SDSL coupled to CW-EPR is used to study the aggregation of the protein α-Synuclein, a process involved in Parkinson's disease. When in monomeric form, the protein tumbling in solution is fast, and results in a spectrum similar to the τ_r = 0.3 ns simulation in figure 6C. Inside aggregates, the motion is slower, and the spectrum looks like the τ_r = 7.94 ns simulation. By measuring changes in spectral shape over time, the aggregation process can be followed. When combined with pulsed EPR techniques, SDSL is an even more powerful method: if two labels are present within a nanometer range inside a protein, their distance can be measured using the EPR method described in subchapter 1.8.

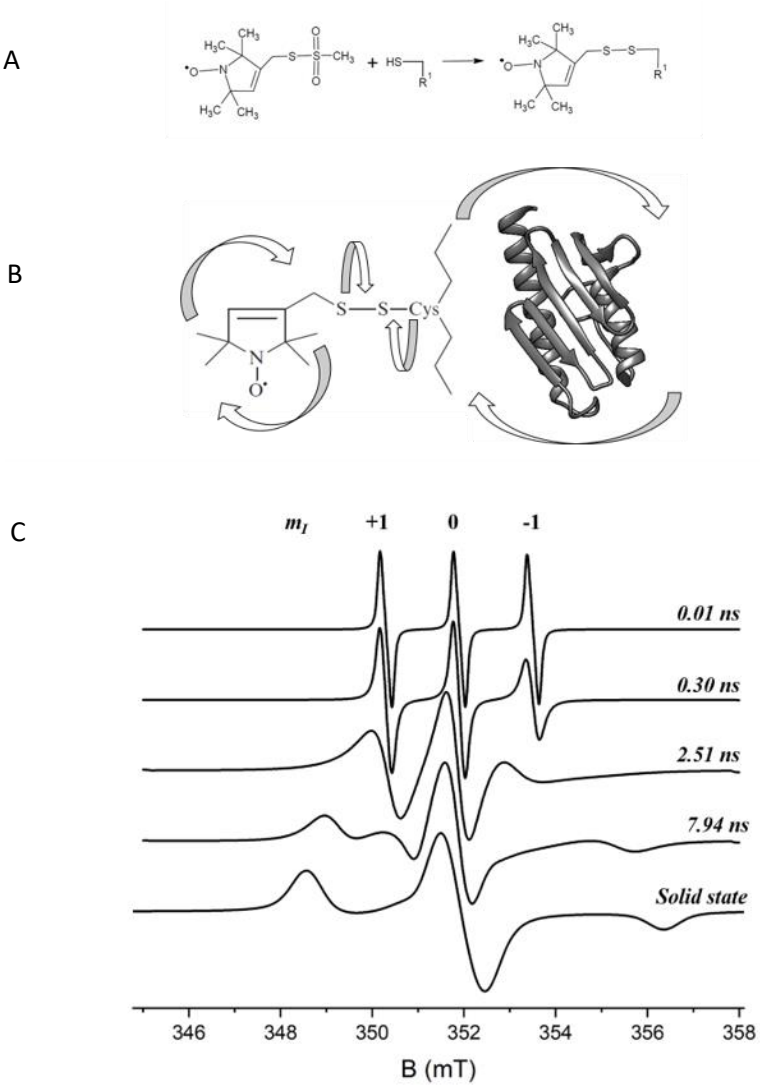

Figure 6. Site directed spin labeling (SDSL) and effect of spin label rotation on nitroxide EPR spectra. A) Reaction scheme of the attachment of MTSL spin label to a cysteine residue on a protein. B) The EPR spectrum will depend on the motion of the label, i.e. by the rotameric motion of the label (arrows indicating rotation of the bonds and of the proxyl ring) and by the molecular tumbling of the protein in solution (arrows around the protein structure). The protein shown in grey, Frataxin, is a small globular protein (14 KDa) and an increase in solution viscosity was necessary to slow the molecular tumbling and probe site-specific dynamics [10]. C) Simulated EPR spectra of a nitroxide spin label for different rotational correlation time.

1.7 Multifrequency EPR

By looking at the spin Hamiltonian (eq. 1), it is evident that only one term, the Zeeman interaction, depends on the field $\mathbf{B_0}$. By varying the magnetic field at which the experiment is performed – together with the operating frequency of the microwave radiation – different aspects of the spin Hamiltonian can be explored. For instance, the g-tensor anisotropy is better resolved at higher magnetic fields, due to the increased separation of energy levels. An example is illustrated in figure 7, where the solid state spectrum of a nitroxide is given at 9 and 275 GHz EPR. At 9 GHz EPR, the hyperfine coupling A_z dominates the spectrum, and the **g**-tensor is poorly resolved. At 275 GHz EPR, the **g**-tensor anisotropy can be accurately measured, and is dominating the spectral shape, while only the A_z component of the hyperfine is resolved. In chapter 4, a Cu(II) system is analyzed at different frequencies. Copper in the 9 GHz EPR solid-state spectrum (figure 8) appears as an axially symmetric spectrum (g_x and g_y not resolved). The hyperfine splitting with the Cu(II) nucleus into four

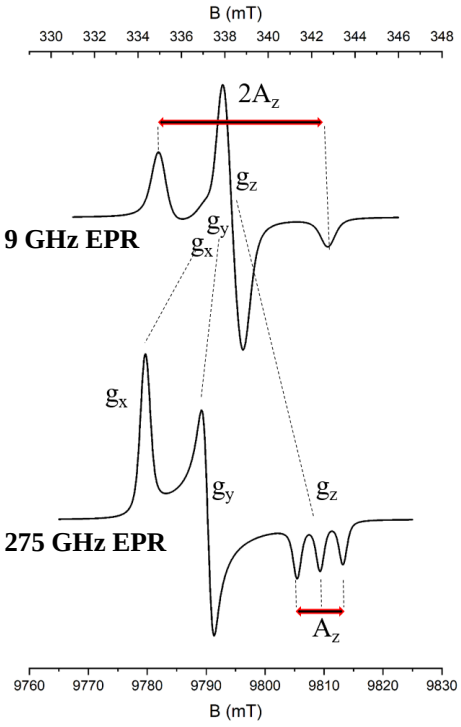

Figure 7 Examples of multifrequency EPR on a nitroxide system: the nitroxide spectrum at 9 GHz is dominated by the large A_z, and the g-tensor is poorly resolved. At 275 GHz, the g-tensor is well resolved.

lines ($I_{Cu} = {}^{3}/_{2}$) is resolved along the z-direction. At 275 GHz EPR small deviations from axial symmetry, i.e. small differences between g_x and g_y components, are resolved. At the same time, the hyperfine splitting A_z is hidden in the broader linewidth, and can't be accurately measured.

A combination of measurements at different frequencies offers unique insights into the electronic properties of complex systems and allows to fully evaluate their spin Hamiltonian parameters. This approach enhances the versatility of EPR, as multiple frequencies can also be applied to pulsed methods, allowing detailed characterization of paramagnetic systems.

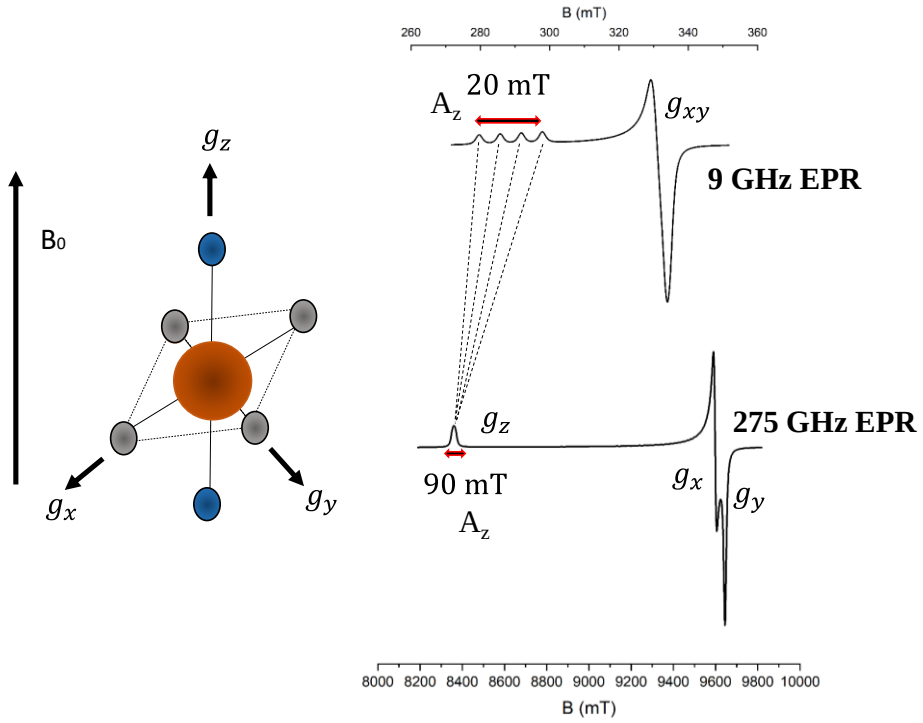

Figure 8 Example of multifrequency EPR on a Cu(II) complex. Right: EPR simulations show that in the 9 GHz EPR spectrum of a copper system with minor deviation from axial symmetry, the difference between g_x and g_y is not resolved, with $g_x \approx g_y$, and the A_z hyperfine splitting resolved along the g_z direction. At 275 GHz, the difference between g_x and g_y is resolved, but information on hyperfine coupling is masked by the linewidth. Left: structure scheme illustrating the copper center (orange) on which the unpaired electron is localized, coordinated in an octahedral geometry by the ligands (grey and blue spheres). The arrows indicate approximate g-tensor directions. The x and y coordination are nearly identical. Subtle deviations from axial symmetry, i.e. differences between g_x and g_y induced by slightly different coordination or tilting of the ligands, can only be resolved at high frequency EPR.

1.8 Double Electron Electron Resonance (DEER)

Double electron electron resonance spectroscopy is a pulsed EPR method designed to measure dipole-dipole interactions between unpaired electrons within a nanometer distance (typically 1.5-10 nm) [15]. From the dipole-dipole interaction, the distance between the spins can be extracted. This method is particularly powerful to obtain distance constraints in doubly spin-labelled proteins, providing insight into their structure and function. Due to fast relaxation times of the electron spins, DEER experiments are performed at cryogenic temperatures.

The pulse sequence used in chapter 5 for DEER spectroscopy is shown in figure 9. Microwaves are applied in pulses, whose length, power and timing depends on the specific applications and samples. A detailed description is provided in [16]. To describe DEER, here we follow the lines of [17]. The DEER technique is a double frequency experiment: the observer frequency is used to detect a signal from spin A, and the pump frequency will excite the second spin, B, that is coupled to A. During the experiment, the observer sequence is kept constant, while the timing of the pump pulse is varied. The resulting data (see figure 9) will consist of a time trace which shows the intensity of the signal detected for A as a function of pump pulse's position in the sequence.

The primary DEER data contains information about intramolecular interactions, and a background decay that depends on intermolecular interactions (figure 9B). After removal of the background decay, the form factor is obtained (figure 9C). In the form factor the modulation depth Δ depends on the amount of pumped B spins, while the modulations contain information about the dipole-dipole interactions. From the form factor, a distance distribution plot is derived, giving the population of spin-pair distances as a function of the distance (figure 9D).

After background correction, the signal amplitude as a function of time for i pumped spins B_i is given by:

$$f(t) = \prod_i^N \{1 - \lambda_i [1 - cos(\omega_{dd,i} t)]\} \quad (6)$$

where λ is the inversion efficiency of the pump pulse (how effectively the pump pulse inverts the B spins), with Δ = λ for two spin systems, and ω_{dd} is the electron-electron coupling frequency, which relates to the distance between the spins and their relative orientation:

$$\omega_{dd,i} = \left({}^{C_i}/_{r_i^3} \right) (1 - 3cos^2\theta_i) \quad (7)$$

Here, θ is the angle between the inter-spin vector and the magnetic field, r is the distance between the spins, and $C_i = \frac{\mu_0 g_1 g_2}{4\pi h}$, where μ_0 is the vacuum permeability, g_1 and g_2 are the g-factors of the spins, and h is the Planck's costant. From here, there are several methods to obtain distance distribution, used in chapter 5 are Tikhonov regularization, Gaussian fitting, and the neural networks based method DEERNet [18-20].

Complications arise in systems with more than two coupled spins. In figure 9 an example is given for a three spin system with spins A, B and C. In such systems, the signal from A will not just be modulated by the pairwise dipole-dipole interaction frequencies (ω_{AB} and ω_{AC}), but also by the sum and difference of those frequencies [21]. The form factor for the three-spin system is obtained by summing over all N possible observer spins:

$$F(t) = \frac{1}{N}\sum_{A=1}^{N}\prod_{A\neq B}^{N} f_{AB}(t) \tag{8}$$

Here, $f_{AB}(t) = 1 - \lambda_B(1 - \cos(\omega_{AB}t))$ is the dipolar evolution of an individual spin pair. Additional modulations in the form factor introduce artifacts in the distance distribution, referred to as ghost distances. Several methods have been developed to minimize these artifacts to obtain pure pairwise distances from multispin systems. On one hand, the problem can be solved experimentally: by adjusting the power of the pump pulse, it is possible to pump less spins, thereby reducing multispin effects. An effect similar is achieved by using paramagnetic species with broad, anisotropic spectra, where only a smaller fraction of the pumped spins can be excited. In [21] a method was developed to suppress multispin effects during data processing. This method relies on applying the scaling exponent 1/(N-1) to the multispin form factor, where N is the number of spins contributing to the signal. This method is called "power scaling". In [22] a method to count how many spins are contributing to the DEER signal was designed. It is based on the fact that the modulation depth Δ observed for multispin systems and the modulation depth λ of a two-spin reference have the following relation:

$$\Delta_N = 1 - (1 - \lambda)^{N-1} \tag{9}$$

With N being the number of spins. Particular care has to be taken: the multispin and the two-spin systems need to be similar systems (the same paramagnetic species) and measured under identical experimental conditions. A detailed description of DEER spectroscopy is given in [17].

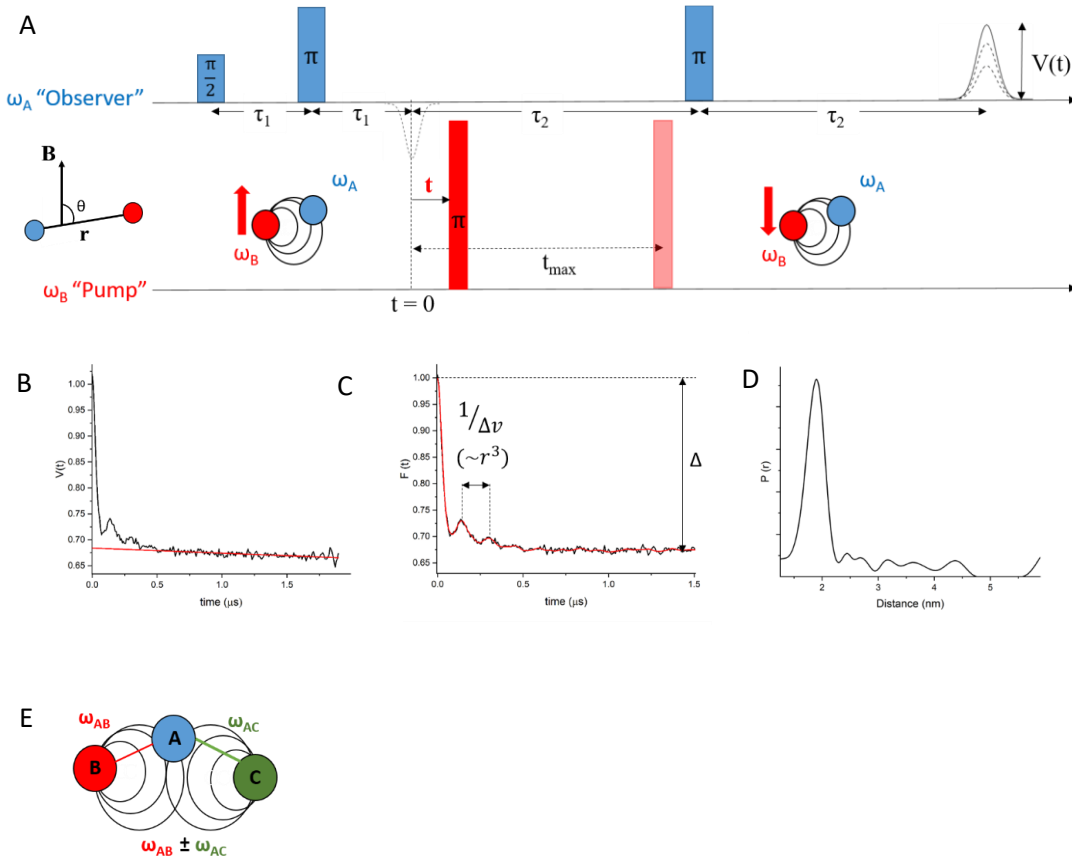

Figure 9. DEER spectroscopy. A) Pulse sequence. Blue: observer sequence. Red: pump sequence. Inset: in equation 7, θ is the angle between the field direction and the vector connecting the two spins. B) Primary data (black) and background decay (red). C) Form factor after background subtraction. F(t) contains information on number of spins (Δ) and the modulation contain information on dipolar interaction. D) Distance-distribution plot. E) In a three spin system, additional modulation come from sum and difference frequencies, producing artifacts in the distance distribution.

1.9 Overview of the thesis chapters

This thesis explores application of EPR methods on diverse systems. Chapter 2 examines how MTSL, the spin label (figure 6A) used to label and probe specific sites in bio-molecules, is forming dimers in aqueous solution. The dimerization process is limiting the efficiency of the labelling reaction. In chapter 2 the dimerization is studied in detail and a proposal is made for the dimer structure and the dimerization reaction mechanism. In chapter 3, EPR is used in combination with site-directed-spin-labeling (SDSL), to investigate the aggregation of the intrinsically disordered protein α-Synuclein. α-Synuclein aggregation is a process involved in Parkinson's disease. The goal is to develop an EPR method to identify the different species formed during the aggregation process, with a focus on the aggregation intermediates, the toxic species involved in the neurodegeneration [23]. Chapter 4 uses a multifrequency EPR approach to characterize a short lived intermediate formed in the reaction between Small LACcase (SLAC), an algae-derived enzyme, with oxygen. The protein SLAC is an interesting enzyme for industrial applications and characterization of its active site is crucial for bioengineering and development of biomimetic catalysts [24]. Finally, in chapter 5, a pulsed EPR method is applied to derive structural information from supramolecular, self-assembled metallo-organic complexes, giving a first example of the application of dipolar EPR spectroscopy to systems containing multiple Cu(II) ions.

1.10 References

[1] Zavoisky Y., Paramagnetic Absorption in Perpendicular and Parallel Fields for Salts, Solutions and Metals, Kazan State University., 1944.

[2] Zavoisky Y., Spin-magnetic resonance in paramagnetics, Fizicheskiĭ Zhurnal 9 (1945) 211-245.

[3] H. Blok, J.A.J.M. Disselhorst, S.B. Orlinskii, J. Schmidt, A continuous-wave and pulsed electron spin resonance spectrometer operating at 275GHz, Journal of Magnetic Resonance 166(1) (2004) 92-99.

[4] J.R. Bolton, J.A. Weil, Electron Paramagnetic Resonance - Elementary Theory and Practical Applications, John Wiley & Sons2007.

[5] N.M. Atherton, Electron Spin Resonance: Theory and Applications, Ellis Horwood1993.

[6] D. Goldfarb, S. Stoll, EPR spectroscopy. Fundamentals and Methods (Book), John Wiley & Sons, 2018.

[7] D. Goldfarb, S. Stoll, E.J.L. McInnes, D. Collison, Chapter 4, EPR Interactions - Coupled Spins, EPR spectroscopy. Fundamentals and Methods (Book), John Wiley & Sons, 2018.

[8] S.S. Eaton, L.B. Woodcock, G.R. Eaton, Continuous wave electron paramagnetic resonance of nitroxide biradicals in fluid solution, Concepts Magn Reson Part A Bridg Educ Res 47A(2) (2018).

[9] C.J. López, M.R. Fleissner, Z. Guo, A.K. Kusnetzow, W.L. Hubbell, Osmolyte perturbation reveals conformational equilibria in spin-labeled proteins, Protein Science 18(8) (2009) 1637-1652.

[10] D. Doni, L. Passerini, G. Audran, S.R.A. Marque, M. Schulz, J. Santos, P. Costantini, M. Bortolus, D. Carbonera, Effects of Fe2+/Fe3+ Binding to Human Frataxin and Its D122Y Variant, as Revealed by Site-Directed Spin Labeling (SDSL) EPR Complemented by Fluorescence and Circular Dichroism Spectroscopies, International Journal of Molecular Sciences, 2020.

[11] A. Czogalla, A. Pieciul A Fau - Jezierski, A.F. Jezierski A Fau - Sikorski, A.F. Sikorski, Attaching a spin to a protein -- site-directed spin labeling in structural biology, (0001-527X (Print)).

[12] P.G. Fajer, Electron Spin Resonance Spectroscopy Labeling in Peptide and Protein Analysis, Encyclopedia of Analytical Chemistry 2006.

[13] C.S. Klug, J.B. Feix, Methods and Applications of Site-Directed Spin Labeling EPR Spectroscopy, Methods in Cell Biology, Academic Press2008, pp. 617-658.

[14] M.R. Fleissner, D. Cascio, W.L. Hubbell, Structural origin of weakly ordered nitroxide motion in spin-labeled proteins, Protein Science 18(5) (2009) 893-908.

[15] G. Jeschke, DEER distance measurements on proteins, Annu Rev Phys Chem 63 (2012) 419-46.

[16] D. Goldfarb, S. Stoll, Chapter 11, Pulse EPR, EPR spectroscopy. Fundamentals and Methods (Book), John Wiley & Sons, 2018.

[17] D. Goldfarb, S. Stoll, G. Jeschke, Chapter 19, Dipolar Spectroscopy - Double-resonance Methods, EPR spectroscopy. Fundamentals and Methods (Book), John Wiley & Sons, 2018.
[18] S.S. G. Jeschke, DeerAnalysis User Manual - Version 2019, (2019).
[19] S.G. Worswick, J.A. Spencer, G. Jeschke, I. Kuprov, Deep neural network processing of DEER data, Science Advances 4(8) eaat5218.
[20] J. Keeley, T. Choudhury, L. Galazzo, E. Bordignon, A. Feintuch, D. Goldfarb, H. Russell, M.J. Taylor, J.E. Lovett, A. Eggeling, L. Fábregas Ibáñez, K. Keller, M. Yulikov, G. Jeschke, I. Kuprov, Neural networks in pulsed dipolar spectroscopy: A practical guide, Journal of Magnetic Resonance 338 (2022) 107186.
[21] T. von Hagens, Y. Polyhach, M. Sajid, A. Godt, G. Jeschke, Suppression of ghost distances in multiple-spin double electron-electron resonance, Phys Chem Chem Phys 15(16) (2013) 5854-66.
[22] D.M. Bela E. Bode , Jorn Plackmeyer , Gerd Durner, Thomas F. Prisner, Olav Schiemann, Counting the monomers in nanometer-sized oligomers by pulsed electron-electron double resonance, JACS 129 (2007) 6736-6745.
[23] A. Villar-Piqué, T. Lopes da Fonseca, T.F. Outeiro, Structure, function and toxicity of alpha-synuclein: the Bermuda triangle in synucleinopathies, Journal of Neurochemistry 139(S1) (2016) 240-255.
[24] M.u. Rahman, M.W. Ullah, J.A. Shah, S. Sethupathy, H. Bilal, S.A. Abdikakharovich, A.U. Khan, K.A. Khan, N. Elboughdiri, D. Zhu, Harnessing the power of bacterial laccases for xenobiotic degradation in water: A 10-year overview, Science of The Total Environment 918 (2024) 170498.

Chapter 2.
Identifying the Elusive Dimerization Product Interfering with Methylsulfonato-group Labelling of Cysteines in Proteins

This chapter will be submitted to Chemistry-A European Journal: L. Passerini, R. Dekkers, K.B.S.S. Gupta, M. Overhand, M. Huber. “Identifying the elusive dimerization product interfering with methylsulfonato-group labelling of cysteines in proteins”, to be submitted.

2.1 Introduction

The methanethiosulfonate (mts)-group is an often used functional group to couple an mts-label to a thiol-group, often from a cysteine of a protein. The mts-group is popular because of its high reactivity and selectivity. This group enables to selectively label proteins with spin- or fluorescent-labels. Often, labelling is the first step to obtain structural or biochemical information, because it opens up a way to apply a variety of techniques in biochemical research, such as electron paramagnetic resonance (EPR), super-resolution-microscopy-techniques, or *Förster*-resonance-energy-transfer (FRET) based distance measurements. Spin labeling is universally applied to investigate proteins by EPR or paramagnetic NMR [1, 2]. It enables structure determination by nanometer-distance constraints by EPR methods [3-6] or the elucidation of protein dynamics or protein-partner interactions, in vitro or in cells [7-13].

Yet the reaction has a major disadvantage: under standard conditions, when cysteine groups of proteins are labelled with the well-known spin label MTSL ((1-Oxyl-2,2,5,5-tetramethyl-Δ-3-pyrroline-3-methyl) methanethiosulfonate) [14], a side reaction occurs that limits the reaction yield. A characteristic EPR signal shows that the side product is a molecule in which two nitroxide radicals are coupled, i.e. a nitroxide-biradical. To suppress this reaction, the MTSL concentrations has to be kept below 200 µM [15], which limits protein concentrations to 20 µM at the typical 10:1 excess of spin label.

In spite of four decades of site-directed-mutagenesis spin labelling, pioneered by the Hubbell group [10, 11], the underlying reaction is not known. Here, we study the formation of the

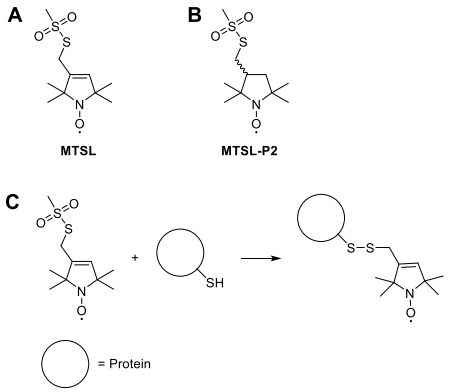

Figure 1. Structure of methylsulfoxide spin label (MTSL) investigated (A), MTSL-P2 (B), and labelling-reaction scheme of the reaction of the label with a cysteine in the protein (C).

side-product under typical spin-labelling conditions for the most-used variants of the methanethiosulfonate spin label (Fig. 1A and 1B) and determine the structure of the biradical-side product by a combination of EPR and mass spectrometry, solving a puzzle that was plaguing labelling reactions for the last four decades.

2.2 Materials and methods

Description of experiment

MTSL ((1-Oxyl-2,2,5,5-tetramethyl-Delta-3-pyrroline-3-methyl)Methanethiosulfonate) and MTSL-P2 ((1-Oxyl-2,2,5,5-tetramethylpyrrolidin-3-yl) methyl methanethiosulfonate) were purchased from Toronto Research Chemicals. Stock solutions were prepared in DMSO, MTSL concentration 24 mM, and stored at -20 °C. The samples were prepared by diluting the stock solutions in 10 mM TRIS-HCl buffer, pH 7.4, for a final MTSL concentration of 100 µM. Incubation was performed on a thermomixer (Eppendorf, Thermomixer comfort) at a temperature of 24°C and shaking at 1000 rpm. A volume of 20 µL was extracted at selected time points for EPR measurement. TCEP (tris(2-carboxyethyl)phosphine) was purchased from Sigma Aldrich. To test reduction, a five molar excess of TCEP was added to the incubating solution, the reaction was allowed to proceed for 30 minutes before EPR measurement. The EPR signal intensity (double integral) was measured before adding TCEP and after the end of the incubation time to be sure that no radical decay occurred after addition of TCEP and during the incubation time. For preparation of the ESI-MS samples, the stock in DMSO was diluted in ammonium acetate (NH_4Ac) buffer, pH 7.4, and incubated in the same conditions (24 °C, 1000 rpm). Dimer formation and effect of TCEP were checked with EPR measurements before ESI-MS analysis.

EPR measurement conditions

EPR spectra were acquired on an EMX EPR spectrometer (Bruker, Rheinstetten, Germany). Glass micropipettes of a volume of 50 µL (Blaubrand Intramark, Wertheim, Germany) were filled with 20 µL of sample for each measurement. Measurement conditions were: microwave frequency: 9.88 GHz, modulation amplitude: 0.2 mT, modulation frequency: 100 KHz, power: 0.63 mW, time constant: 10.24 ms, conversion time: 10.24 ms. All measurements were performed at room temperature.

EPR spectra simulation

MATLAB (R2019a, The MathWorks, Inc., Natick, MA,USA) and the EasySpin package (5.2.35)[16] were used for simulations of the EPR spectra. Spectra were simulated as the sum

of monoradical and biradical nitroxides using the "pepper" function with isotropic g and hyperfine tensors, since biradical spectra can only be simulated by "pepper". Parameters used for the simulation can be found in table 1. The contribution (weight) of the monomer and biradical components to the simulation was adjusted to match the experimental spectral shape. Errors were determined by manually adjusting the contributions of the components until the simulation were visibly deviating from the experimental lineshape.

ESI-MS

ESI-MS samples were prepared as described in the "description of experiment" section above. Measurements were performed with an Q-Exactive HF Orbitrap (Thermo Scientific) equipped with an electrospray ion source (ESI), injection of 2 µl of a 1 µM solution via Ultimate 3000 nano UPLC (Dionex) system , with an external calibration (Thermo Scientific). Source voltage of 3.5 kV, capillary temperature 275 °C, no sheath gas, Resolution = 240.000 at m/z=400. Mass range m/z=160-2000 or until a maximum of 6000. Eluents used: MeCN:H_2O (1:1 v/v) supplemented with 0,1% formic acid.

2.3 Results

In a typical spin-labelling reaction the protein is incubated with a ten-fold excess of spin label in a suitable aqueous buffer solution using reaction times between two and 18 hours, either at room temperature or at 4 °C. Here we mirror these conditions, by studying the reaction systematically in the absence of the protein.

Figure 2 shows the EPR spectrum of (1-Oxyl-2,2,5,5-tetramethyl-Δ-3-pyrroline-3-methyl) methanethiosulfonate (MTSL) after nine hours of incubation in an aqueous solution (buffer), such as the conditions normally used for protein-spin labelling. The spectrum observed is the superposition of two components, shown separately in figures 2B and 2C. One is the classical three-line spectrum (fig. 2B) of nitroxide radicals at room temperature. The splitting into three lines arises from hyperfine interaction of the unpaired electron with the ^{14}N nucleus of the N-O bond. The second component is a five-line spectrum (fig. 2C), that originates from two coupled nitroxide radicals [17], which we will refer to in the following as biradical. A five-line pattern is observed, if the exchange interaction (J) is significantly larger than the hyperfine interaction A_{iso} ($J>2\ A_{iso}$)[17-19]. In table 1, the relevant spectral parameters are given, which are obtained from spectral simulations (see Materials and methods).

Spectra were acquired in time intervals over the course of two days. Figure 3 shows the relative contribution of the MTSL biradical and the monomer component as they develop over time. The biradical contribution increases over time and a maximum of 55% in the biradical component is observed after nine hours of incubation, followed by a decrease to a value of 23% after 51 hours of incubation. The total radical concentration, obtained from the

double integration of the EPR spectra, shows an initial decrease in the number of spins in the sample during the first three hours of incubation, possibly due to decay of the radical. Then the number of spins in the sample reaches a plateau and remains constant for the entire incubation time (green points in figure 3).

After a fair amount (43 %) of biradical had formed in the solution, a mild reductant, specific for disulfide bridges, TCEP (tris(2-carboxyethyl)phosphine), was added to the incubating MTSL solution in a five-fold excess relative to MTSL. This abolishes the biradical component in the EPR spectrum completely, see fig. 4A, suggesting that the biradical contains a disulfide bond.

To obtain information on the structure of the dimer, we used mass spectrometry (electron-spray-ionization mass spectrometry, ESI-MS). Mass spectrometry of the MTSL sample after three hours of incubation shows a base peak at 466 m/z. Simulation of the peak gives the element composition of the

species: $C_{19}H_{34}O_5N_2S_3$. Upon addition of TCEP to the sample, the 466 m/z peak disappears, and a new base peak of 267 m/z appears, corresponding to the oxidized TCEP. The peak of 267 m/z confirms that TCEP

reacts with a disulfide bond. Another new peak at 249 m/z is observed after reaction of the dimer with TCEP, possibly a breakdown product of the reaction between the MTSL dimer and TCEP, however, this peak could not be assigned to a specific chemical structure. Mass spectra are shown in fig. SI 5 and in table 2 the base peaks observed are listed.

For the analogous compound, MTSL-P2, similar results to MTSL were observed. In fig. 4B the EPR spectrum obtained after three hours incubation is shown. Also in this case, the spectrum originates from a superposition of the three-line-nitroxide spectrum with a biradical spectrum of two coupled nitroxides. For MTSL-P2, the shape of the biradical spectrum differs from that of MTSL. The spectrum can be simulated with J = 71 MHz, see table 1. This value of J, however, does not reproduce accurately the experimental spectrum, as the peaks at 345 and 356 mT in the simulation are not observed in the spectrum (see fig SI1). The time course of the reaction (fig. SI 4) closely parallels that of MTSL. Also in the case of MTSL-P2, addition of TCEP completelely abolished the biradical component in the EPR spectrum, see fig. 4 B.

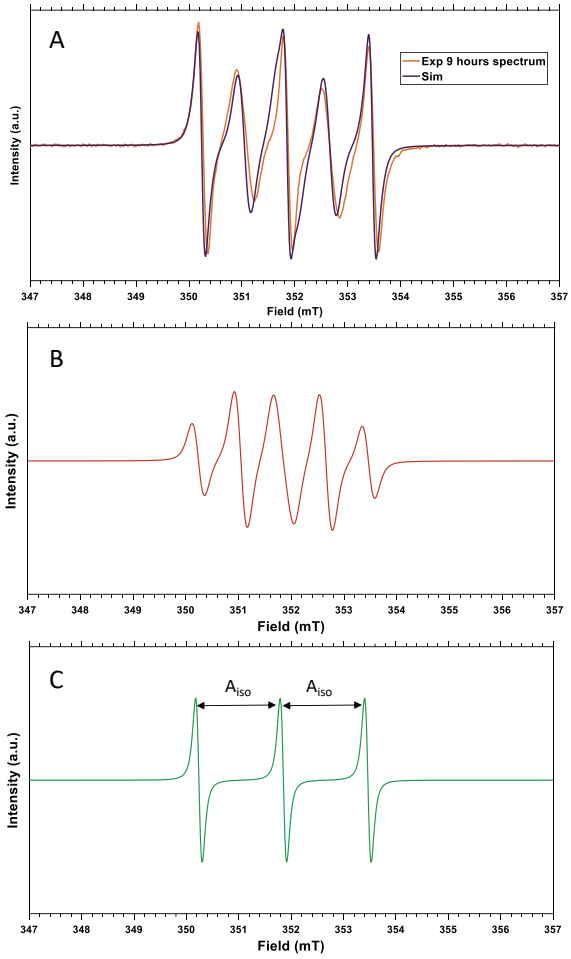

Figure 2. Formation of the MTSL biradical monitored by EPR. A) Spectrum, after nine hours of incubation in aqueous buffer. Purple: experimental spectrum, black: total simulation, orange: biradical component, green : mono-radical component. B) Biradical component from A). C) Mono-radical component. EPR spectra recorded as first derivative of absorption.

Mass spectra of the MTSL-P2 solution after three hours of incubation show a base peak at 470 m/z and, as observed for MTSL, addition of TCEP causes the disappearance of the 470 m/z peak and appearance of the peak corresponding to oxidized TCEP, at 267 m/z.

The similar behaviour of MTSL and MTSL-P2 with respect to dimer formation, the reaction with TCEP, and the base peaks of the mass spectra of the dimers observed, indicates that the same chemical dimerization reaction is happening for both labels.

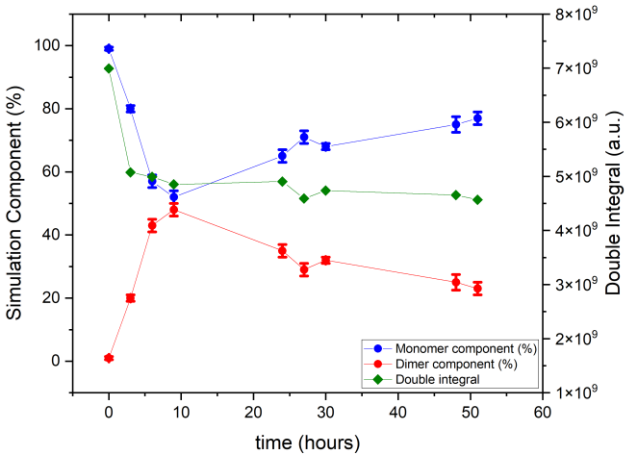

Figure 3. Development of mono- and biradical components for MTSL over time. Blue: monoradical contribution, red: biradical contribution, green: total intensity of the EPR spectrum (double integral). For details about error estimation, see Materials and methods.

Table 1. Parameters used for simulation of mono- and biradical EPR spectral components of MTSL and MTSL-P2. For details, see Materials and methods

	Monomer		Biradical		
	g_{iso}	A_{iso} (MHz)	g_{iso}	A_{iso} (MHz)	J (MHz)
MTSL	2.0059	45.3	2.0059	45.3	600
MTSL-P2	2.0059	45.3	2.0059	45.3	71

Table 2. Mass spectrometry results: base peaks observed in the mass spectra of MTSL and MTSL-P2 after 24 hours incubation and after TCEP addition to the sample. Mass spectra are shown in S.I. For details, see Materials and methods

	During incubation			After TCEP addition	
	Mass**		Sum formula	Mass	
MTSL	466.16210	100%	$C_{19}H_{34}O_5N_2S_3$	267.06245*	100%
MTSL-P2	470.19340	100%	$C_{19}H_{38}O_5N_2S_3$	267.06240*	100%

*oxidized TCEP. ** contain extra O-atom because of cysteine oxidation [20]

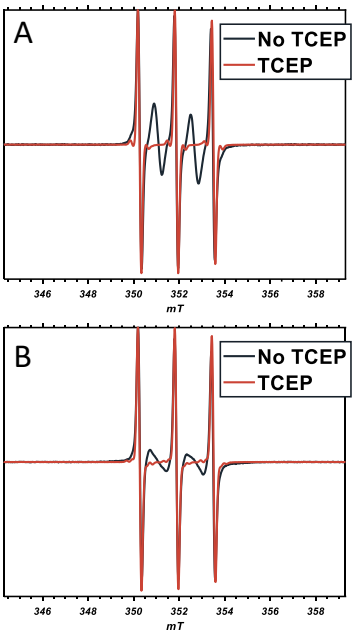

Figure 4. Reductant TCEP (tris(2-carboxyethyl)phosphine) abolishes biradical component. Effect of TCEP on biradical component of MTSL (A) and MTSL-P2 (B). Black: spectrum after three hours of incubation, orange: spectrum obtained after addition of excess TCEP.

2.4 Discussion

In this study, we investigate an unwanted side reaction that interferes with spin labelling of cysteine-proteins. The goal of the study was to understand the reaction and determine the product. To do so, we investigated conditions of product formation for two different spin labels, MTSL and MTSL-P2 (Fig. 1A and B) and propose structures for the products. For both compounds, we show that the product of the side reaction is a nitroxide-dimer, in which the two nitroxide moieties are covalently linked in a reaction that irreversibly converts the mts-group of the MTSL molecule. a.

Within the first nine hours of incubation about 55% of the MTSL is converted to biradical. The biradical contribution to the spectra remains constant (MTSL-P2) or decays after the initial growth period (MTSL). We attribute the decay in the latter case to the breakage of the biradical product or to a biradical decay, i.e. one of the nitroxides on the biradical becomes diamagnetic.. The amount of biradical formed in these experiments is higher than one could

expect, considering that in spin-labelling reactions the concentration of MTSL can be twice as large [15] as in the experiments described here, and also often longer reaction times are used. In the experiments presented here, however, the cysteine-bearing protein (see Fig. 1) is absent. We suggest that in standard spin-labelling reactions the mts-group reacts faster with the electron-rich cysteine SH-group of the protein than with another mts-group (see below), explaining that in protein-labelling dimer formation occurs at significantly higher MTSL concentrations than observed here.

Dimer structure

The EPR spectrum of the biradical contribution shows that two nitroxide moieties interact, and the magnitude of the exchange coupling (J) suggests effective through-space or through-bond coupling of the two nitroxide groups [17]. The biradical of MTSL-P2 has a smaller J than MTSL, suggesting a weaker nitroxide-nitroxide interaction than in the case of MTSL. As described in the SI, some spectral features do not agree with the precise J-value used suggesting that the difference in J could also be due to differences in the biradical-conformational dynamics, as described for other nitroxide biradicals before [17, 19]. Therefore, the difference in the EPR spectra of MTSL and MTSL-P2 cannot be further interpreted. Generally, the exchange interaction cannot easily be related to molecular structure, therefore in order to derive the structure of the dimer, additional information is needed. Chemical evidence comes from the reactions tested here: The pyrroline double bond cannot be involved in the dimerization reaction, because the biradical-rate-of formation and -yield for MTSL is similar to that of MTSL-P2, even though MTSL-P2 lacks this double bond. Also, for MTSL and MTSL-P2, the product must have a reducible disulfide bond, as the biradical EPR spectrum is abolished by TCEP. According to literature, TCEP is selective for disulfides, and does not reduce the nitroxide group [21]. Our experiments confirm this (see Materials and methods), proving that the disappearance of the biradical spectrum is not caused by partial nitroxide reduction in the biradical.

The proposed structure of the dimer (figure 5) agrees with the base peaks from mass spectrometry. Consequently, the asymmetric dimer shown in figure 5 fulfills all the criteria stated above and can be explained by the reaction pathway shown in figure 5.

The reaction starts with the nucleophilic attack of a carbanion at the mesyl group of one MTSL molecule on the mesylated sulfur atom of a second MTSL molecule. The reaction proceeds with the mesyl-group of the second MTSL as the leaving group, forming the hypothesized product. This nucleophilic substitution can be explained by the fact that the methanesulfoxide-group is relatively acidic, while methanesulfinate is known to be an excellent leaving group. The reaction leads to a product that has the expected chemical

properties and agrees with the sum formula from mass spectrometry of the reaction product.

Given that the reaction mechanism does not involve a radical step, the reaction is likely to occur also in other labelling reactions, thus also when fluorescent labels are attached to a cysteine-bearing protein by a methanethiosulfoxide group, yet it was never reported. The reasons could be that fluorescent labels are more often linked by other groups, like the maleimide group, and that the labelling is often carried out at lower concentrations than spin-labelling reactions. Also, there would be no clear signature of a dimer, unlike the biradical in EPR. Ultimately, any dimer product would be removed in the final labelling step

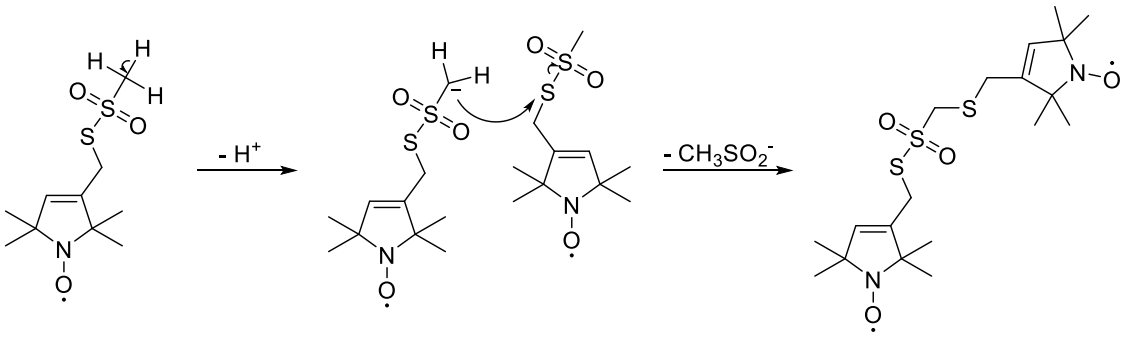

Figure 5 Proposed reaction mechanism for MTSL and structure of the dimer product (right). Note: The additional oxygen-atom mass of the base peak (table 2) is attributed to an cysteine oxidation .

when unreacted label is removed from the protein.

The question that remains is if the side reaction can be suppressed or avoided in spin-labelling reactions. The disulfide linkage of the dimer makes this unlikely as breaking the disulfide bond of the dimer by a reductant would also decouple already coupled spin label from the protein, so it would not be useful.

In conclusion, we show that the unwanted biradical reaction that hampers spin-labelling reactions of proteins is an irreversible process, in which the unwanted product is formed in high yields. We propose a structure for this product that agrees with the mass obtained from mass spectrometry and the chemical properties observed in this study. So after four decades of mystery we have elucidated the reaction that causes the formation of the biradical product in spin-labelling reactions of proteins. We show that this biradical is a covalently bound dinitroxide, linked via a disulfide bond.

Supplementary information

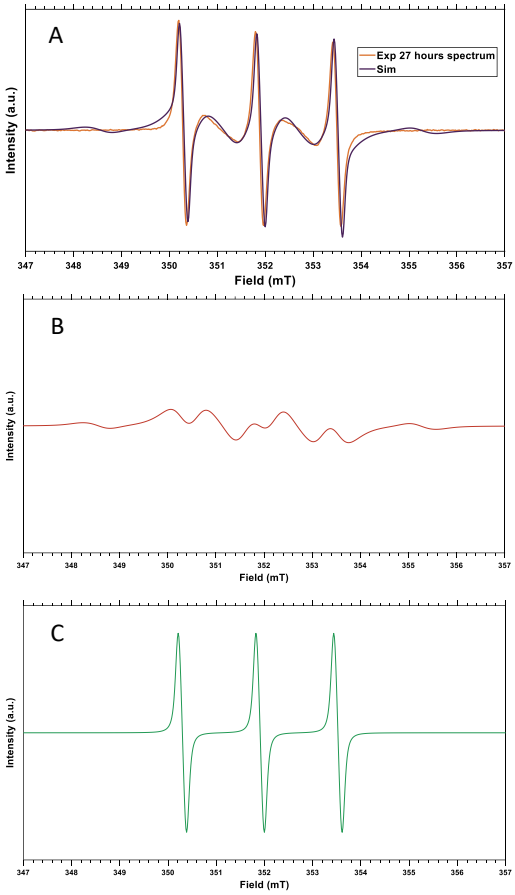

Figure SI.1. Formation of MTSL-P2 biradical monitored by EPR. EPR spectrum after incubation of MTSL-P2 in aqueous buffer. A) Spectrum, after nine hours. Purple : experimental spectrum, black : total simulation, orange : biradical component, green: mono radical component. B) Biradical component from A). C) Monoradical component. EPR spectra recorded as first derivative of absorption. The value of J used was selected solely to reproduce the spectrum between 350 and 354 mT. The simulation shows additional lines at 348 and 356 mT that are not experimentally measured, suggesting the J value used is not accurate.

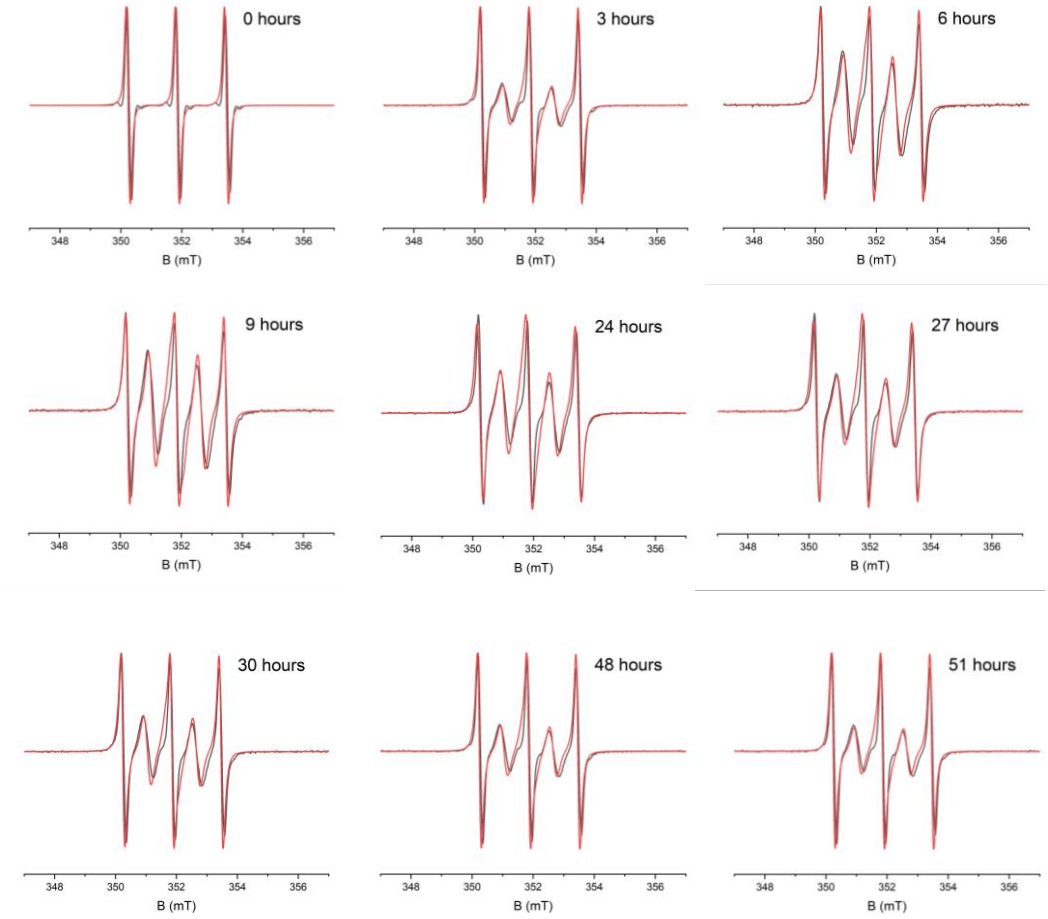

Figure SI.2. EPR spectra of MTSL acquired at different time points. Black: experimental spectrum. Red: simulation.

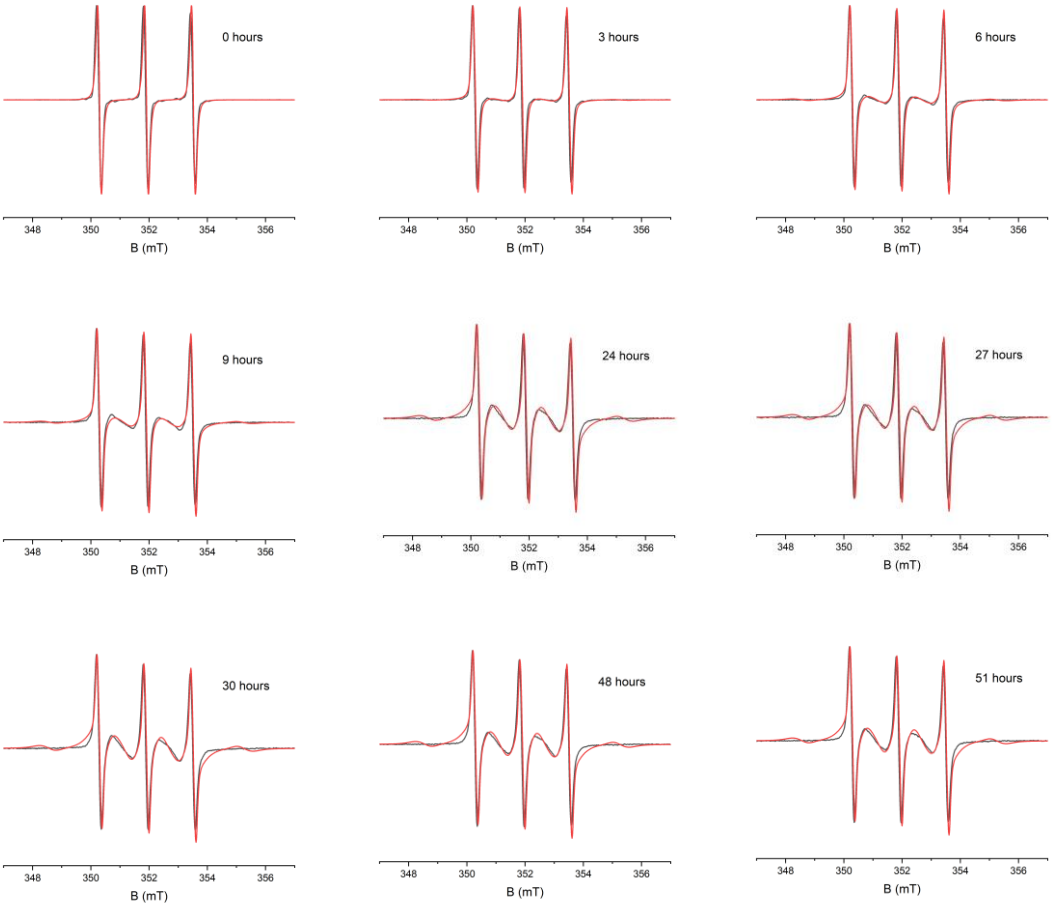

Figure SI.3. EPR spectra of MTSL-P2 acquired at different time points. Black: experimental spectrum. Red: simulation.

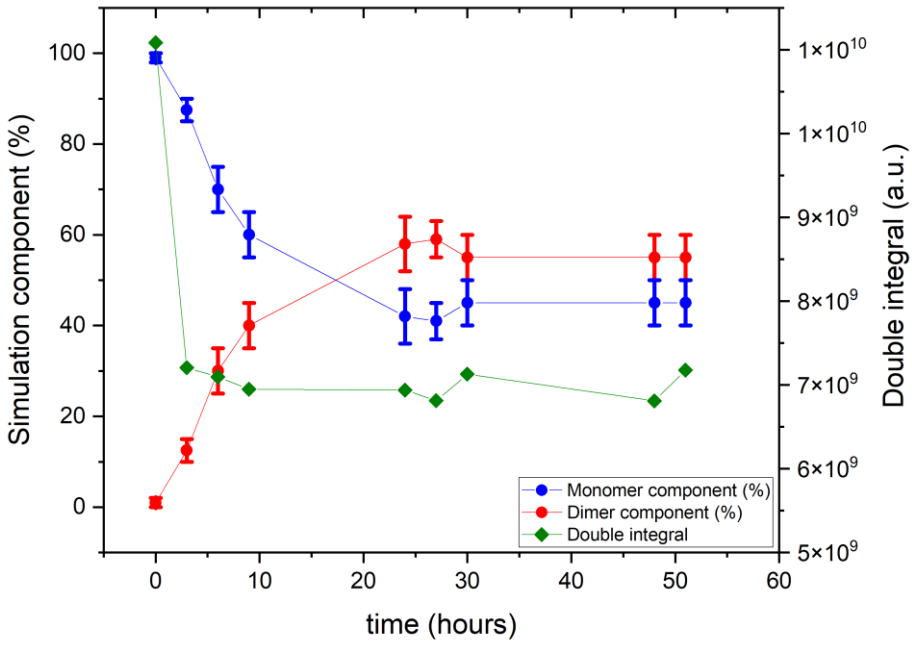

Figure SI.4. Development of MTSL-P2 biradical component over time. Contribution of the mono- and biradical component over the 51 hours of incubation. Blue : monoradical contribution, red : biradical contribution, green : total intensity of the EPR spectrum (double integral value). For details about error estimation, see materials and methods. Given that the simulation of the MTSL-P2 biradical spectrum gives additional lines that are not experimentally observed, the contribution measured through simulation of the biradical for MTSL-P2 is overestimated, and the monomer contribution is underestimated as a consequence.

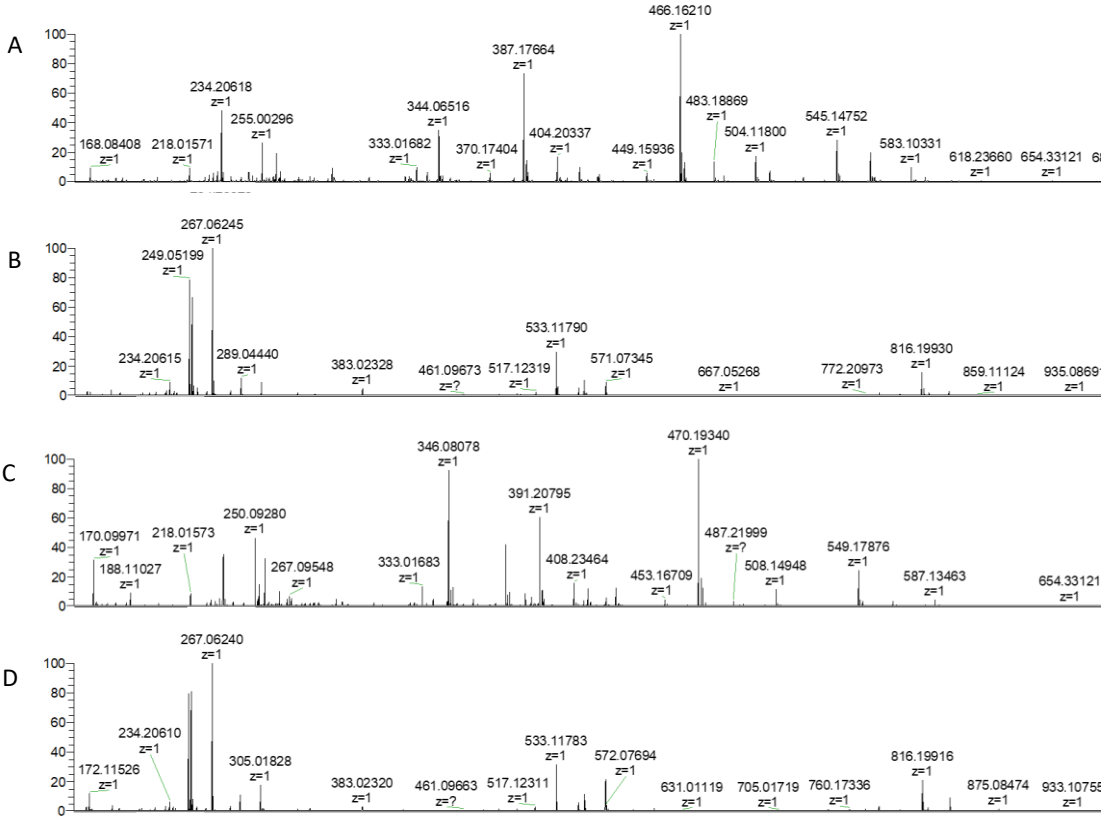

Figure SI.5. MS-ESI spectra of MTSL and MTSL-P2. A): MTSL after three hours incubation. B): MTSL after three hours incubation and reaction with TCEP. C): MTSL-P2 after three hours incubation. D): MTSL-P2 after three hours incubation and reaction with TCEP.

References

[1] P.S.N. Ishita Sengupta, and Christopher P. Jaroniec, Protein Structure Determination with Paramagnetic Solid-State NMR Spectroscopy, Acc. Chem. Res. 46 (2013) 2117-2126.
[2] D.S. Joel R. Gillespie, Characterization of long-range structure in the denatured state of staphylococcal nuclease. I. paramagnetic relaxation enhancement by nitroxide spin labels, Journal of Molecular Biology 268(1) (1997) 158-169.
[3] K. M. Salikhov, and A. M. Raitsimring, The Theory of Electron Spin-Echo Signal Decay Resulting from Dipole-Dipole Interactions between Paramagnetic Centers in Solids, jOURNAL OF MAGNETIC RESONANCE 42 (1981) 255 - 276.
[4] M. Pannier, S. Veit, A. Godt, G. Jeschke, H.W. Spiess, Dead-time free measurement of dipole-dipole interactions between electron spins. 2000, J Magn Reson 213(2) (2011) 316-25.
[5] G. Jeschke, DEER distance measurements on proteins, Annu Rev Phys Chem 63 (2012) 419-46.
[6] S.K. Milov AD, Shchirov MD, Use of the double resonance in electron spin echo method for the study of paramagnetic center spatial distribution in solids, Fiz. Tverd. Tela (Leningrad) 23 (1981) 975-982.
[7] L.C.a.W.L. Hubbell, A new spin on protein dynamics, TRENDS in Biochemical Sciences 27(6) (2002) 288-295.
[8] Y.E. Nesmelov, D.D. Thomas, Protein structural dynamics revealed by site-directed spin labeling and multifrequency EPR, Biophys Rev 2(2) (2010) 91-99.
[9] F. Torricella, A. Pierro, E. Mileo, V. Belle, A. Bonucci, Nitroxide spin labels and EPR spectroscopy: A powerful association for protein dynamics studies, Biochim Biophys Acta Proteins Proteom 1869(7) (2021) 140653.
[10] A.P. Todd, J. Cong, F. Levinthal, C. Levinthal, W.L. Hubbell, Site-directed mutagenesis of colicin E1 provides specific attachment sites for spin labels whose spectra are sensitive to local conformation, Proteins 6(3) (1989) 294-305.
[11] W.L. Hubbell, A. Gross, R. Langen, M.A. Lietzow, Recent advances in site-directed spin labeling of proteins, Current Opinion in Structural Biology 8(5) (1998) 649-656.
[12] A. Bonucci, O. Ouari, B. Guigliarelli, V. Belle, E. Mileo, In-Cell EPR: Progress towards Structural Studies Inside Cells, Chembiochem 21(4) (2020) 451-460.
[13] S. Kucher, C. Elsner, M. Safonova, S. Maffini, E. Bordignon, In-Cell Double Electron-Electron Resonance at Nanomolar Protein Concentrations, J Phys Chem Lett 12(14) (2021) 3679-3684.
[14] L.J. Berliner, J. Grunwald, H.O. Hankovszky, K. Hideg, A novel reversible thiol-specific spin label: Papain active site labeling and inhibition, Analytical Biochemistry 119(2) (1982) 450-455.
[15] E. Bordignon, EPR Spectroscopy of Nitroxide Spin Probes, eMagRes2017, pp. 235-254.
[16] S. Stoll, A. Schweiger, EasySpin, a comprehensive software package for spectral simulation and analysis in EPR, J Magn Reson 178(1) (2006) 42-55.

[17] S.S. Eaton, L.B. Woodcock, G.R. Eaton, Continuous wave electron paramagnetic resonance of nitroxide biradicals in fluid solution, Concepts Magn Reson Part A Bridg Educ Res 47A(2) (2018).
[18] M. Abe, Diradicals, Chem Rev 113(9) (2013) 7011-88.
[19] G.R. Luckhurst, Alternating linewidths. A novel relaxation process in the electron resonance of biradicals, Molecular Physics 10(6) (1966) 543-550.
[20] A. Scherer, X. Yao, M. Qi, M. Wiedmaier, A. Godt, M. Drescher, Increasing the Modulation Depth of Gd(III)-Based Pulsed Dipolar EPR Spectroscopy (PDS) with Porphyrin-Gd(III) Laser-Induced Magnetic Dipole Spectroscopy, J Phys Chem Lett 13(47) (2022) 10958-10964.
[21] E.B. Getz, M. Xiao, T. Chakrabarty, R. Cooke, P.R. Selvin, A Comparison between the Sulfhydryl Reductants Tris(2-carboxyethyl)phosphine and Dithiothreitol for Use in Protein Biochemistry, Analytical Biochemistry 273(1) (1999) 73-80.

Chapter 3.

Investigating α-Synuclein Aggregation In Situ Using Site-Directed Spin Labeling and EPR

3.1 Introduction

α-Synuclein (αS) is an intrinsically disordered protein with 140 aminoacid residues, which is of major interest due to its involvement in neurodegeneration, particularly in Parkinson's disease (PD) [1-4]. Under pathological conditions, αS aggregates into β-sheet rich structures, called fibrils, whose presence is the histological hallmark in the brain of PD patients.

The aggregation of αS is a complex process that involves the formation multiple intermediates, including oligomers, identified as the toxic species taking part in the neurodegeneration, before the mature fibrils are formed [3, 5, 6].

While fibrils are particularly stable structures, and have been extensively characterized by CryoEM and ssNMR [7-13], characterization of oligomers is challenging due to their transient nature and structural heterogeneity [14, 15]. Methods for oligomer characterization often involve chemical modification or dilution for single-molecule experiments [14, 16-21], which can stabilize only specific structures, and potentially distort the natural equilibrium of the aggregation process.

A widely used method to monitor αS aggregation is the Thioflavin T (ThT) fluorescence assay, which allows to specifically detect β-sheet-rich fibrillary aggregates, but does not provide direct information on monomers or early stage intermediates like oligomers [5, 22-24]. A typical ThT fluorescence curve follows a sigmoidal trend: It begins with a lag phase, during which no fluorescence is detected and oligomers and intermediates are forming. The lag phase is followed by an exponential increase as the β-sheet fibrils start to assemble, and ending in a plateau where the system reaches equilibrium [5, 22]. However, since ThT fluorescence only tracks fibrils, it lacks the ability to resolve non-fibrillar species, making it unsuitable to monitor early aggregation events.

Recently, Zurlo et al. [25], developed an approach to investigate αS aggregation in situ using site-directed-spin-labeling (SDSL) and continuous wave electron paramagnetic resonance (CW-EPR) (figure 1)[25]. The key advantage of this method is that it directly measures the mobility of the protein in solution, with different species giving distinct EPR spectral shapes. By measuring the aggregating solution directly, the EPR spectra contain information on all species present, from monomers to oligomers and fibrils. By simulating the EPR spectra with three components, each with a different rotational correlation time (τ_r), the contributions of the different species were disentangled and quantified, giving quantitative information on the amount of monomers, oligomers and fibrils in solution. The study identified an early oligomeric population in equilibrium with monomers, leading to a kinetic model in which oligomers could either serve as precursors to fibrils or dissociate back into monomers [25]. The oligomers identified had a relatively fast dissociation rate, making them impossible to detect with techniques that require separation of species or dilution, making in situ EPR a powerful method for the identification of such metastable, short lived species.

To ensure comparability between different aggregation assays, ThT fluorescence assays must be run in parallel with EPR measurements, allowing direct correlation between fibril formation and EPR spectral changes. Another challenge in applying this method is that the EPR spectral components from different species overlap, making it difficult to unambiguously distinguish the spectral contribution of oligomers from that of fibrils [26]. Also, a three-component simulation may be overfitting the data that suffer from low resolution, especially when the intensities of the long-τ_r components are low, such as at the beginning of the aggregation. In this study, we simplify the analysis by employing a two-component model, where the τ_r of monomers is obtained from monomeric αS and the τ_r of aggregates is determined from fibril-enriched samples. This approach reduces potential fitting bias and improves reproducibility while still allowing the detection of early aggregates. Additionally, we introduce confidence intervals in quantifying component contributions, providing a more robust assessment of the species present in solution.

Another challenge in in situ EPR analysis is label dissociation, which can complicate spectral interpretation [25, 26]. The most commonly used nitroxide spin label, MTSL, forms a disulfide bond with cysteine residues (figure 2) that is susceptible to reduction over time, resulting in a considerable amount of free label contributing to the spectral shape. To address this, we compare multiple spin labels with different chemical linkages, assessing their stability during aggregation (figure 2).

To probe structural features of aggregates, we introduce spin labels at different positions in the αS sequence. By monitoring the time evolution of EPR spectral components for spin labels at position 9, 27 and 56, we show that in situ EPR can reveal how specific regions of αS integrate into aggregates, providing valuable insights into early-stage oligomerization.

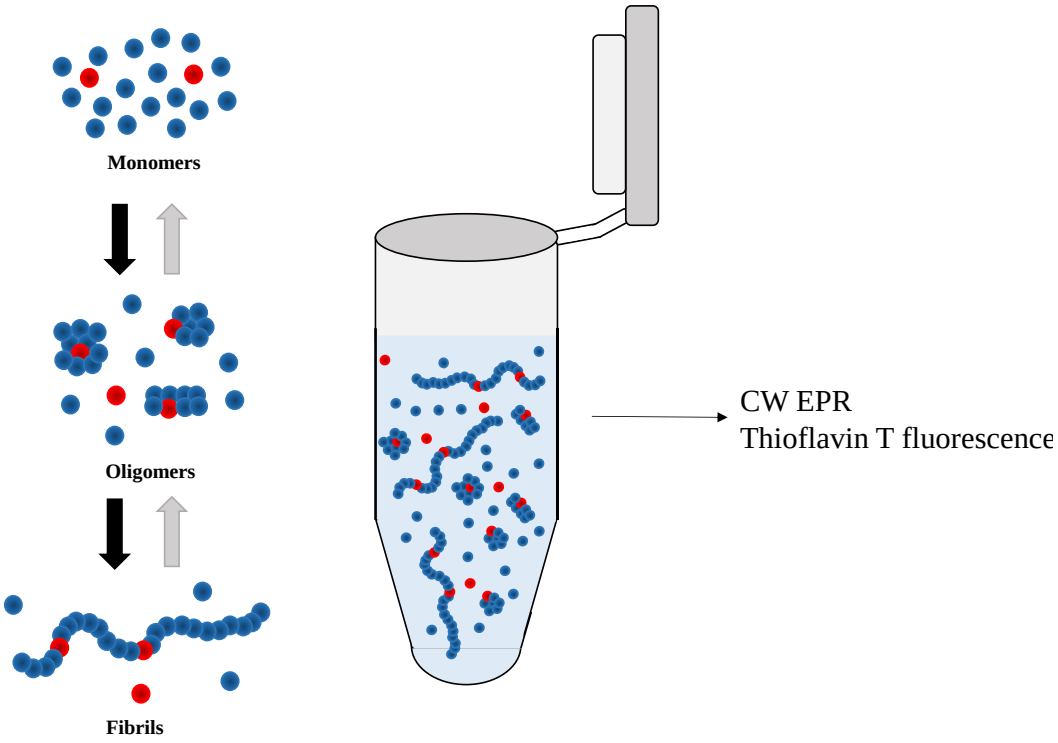

Figure 1. Overall aggregation pathway and depiction of in situ EPR method. Spin labelled αS (red dots) is diamagnetically diluted with wt αS (blue dots). The aggregating sample, containing monomers, oligomers and fibrils is measured directly with CW EPR and ThT fluorescence.

3.2 Materials and Methods

Protein Labeling, Preparation, Aggregation Conditions

Protein expression and purification were as described in Zurlo et al [25]. The spin labels were all purchased by Toronto Research Chemicals. The spin labels used were: MTSL (*S*-(1-oxyl-2,2,5,5-tetramethyl-2,5-dihydro-1H-pyrrol-3-yl)methyl methanesulfonothioate), IAP (3-(2-Iodoacetamido)-2,2,5,5- tetramethyl-1-pyrrolidinyloxy) and MAP (3-Maleimido,2,2,5,5-tetramethyl-1-pyrrolidinyloxy). The labeling was performed as described in Zurlo et al. [25], with variation on the incubation conditions with the label: the incubation with the labels was performed overnight at 4 °C with gentle shaking. Although the protein stocks were purified and monomeric, this was not tested immediately before starting the aggregation experiment, and therefore a small population of multimeric species cannot be excluded. Description of experiment: a stock solution of spin-labeled α-synuclein was diluted into 1 mL

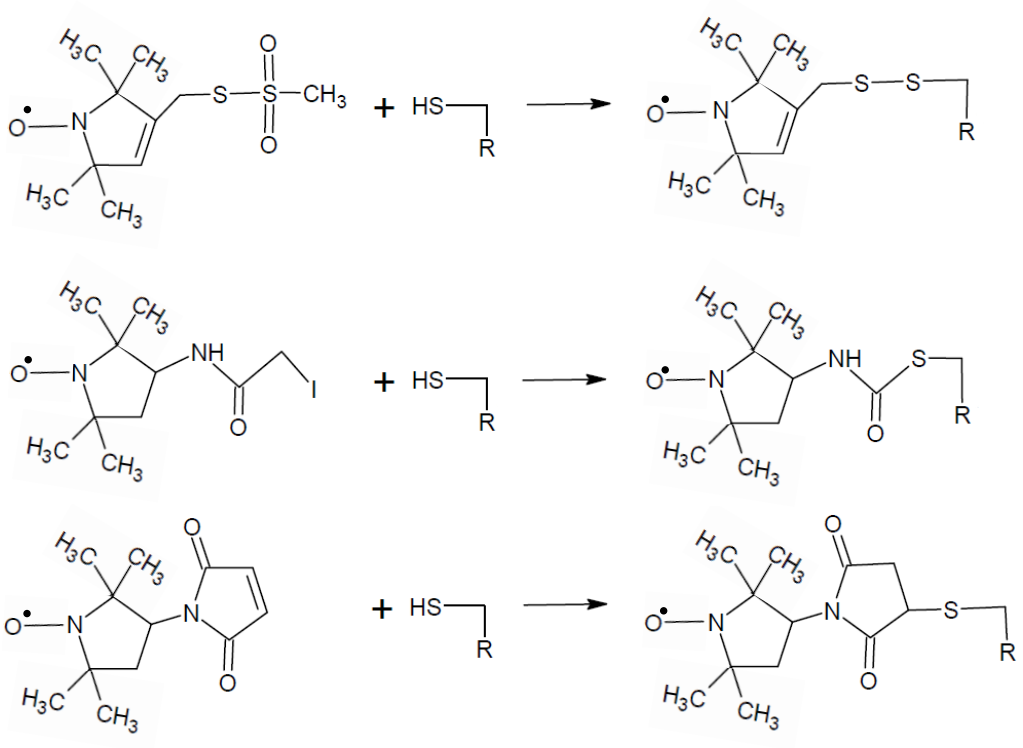

Figure 2. Structures and labeling reactions of the spin labels used in this work. A) MTSL (R1) B) MAP (R2) C) IAP (R3).

of assay buffer (10 mM Tris–HCl, pH 7.4, 0.01% NaN_3), to a final spin concentration of 10 µM. The solution also contained wild-type α-synuclein (wt-αS) for a total α-synuclein concentration of 100 µM. The solutions were prepared in 1.5 mL low bind Eppendorf tubes. After an initial EPR and fluorescence measurement was taken at the time the spin labeled protein was diluted, the samples were allowed to aggregate on a thermomixer (Eppendorf, Thermomixer comfort) with a speed of 1000 rpm at 37 °C. At each time point, 30 µL samples were drawn from the aggregation solution and used for EPR and Thioflavin T (ThT) fluorescence assay. Samples needed to be measured once extracted, as storage at room temperature might allow aggregation to proceed, and fibril denaturation has been proved at low temperatures [27]. This ultimately limits to one, maximum two, aggregating samples that can be run simultaneously.

Diamagnetic Dilution

To suppress changes in the EPR lineshape by spin–spin interactions, all samples were made with a mixture of 9:1 wild type αS: spin-labelled αS, as described in [25].

Thioflavin T fluorescence assay

Thiofavin T (ThT) fuorescence measurements were made by diluting 10 µL of the aggregating solution in 1 mL assay buffer with 5 µM ThT. Measurement were carried out on a Varian Cary Eclipse Fluorescence Spectrophotometer (Varian, Palo Alto, US). Excitation wavelength was set to 440 nm and emission spectra were recorded between 460 and 600 nm. The fluorescence intensity at the 485 nm maximum was recorded. ThioT fluorescence measurement can be subject to fluctuations once the plateau phase is reached. To improve readability of the time traces shown in main text, some of the ThioT fluorescence time points were removed from the plots. This was only done once the curve reached the plateau phase, so the time points in the lag phase and exponential growth phase are not affected.

EPR Measurement Conditions

For the EPR measurements, glass micropipettes of a volume of 50 µL (Blaubrand Intramark, Wertheim, Germany) were filled with 20 µL of the sample for each measurement. The 9 GHz, continuous-wave EPR spectra were recorded using an EMX Plus spectrometer (Bruker, Rheinstetten, Germany). The measurements conditions were: room temperature, microwave power 2.0 mW, modulation amplitude 0.25 mT or 0.5 mT, modulation frequency 100 kHz, time constant 20.48 ms. The high modulation amplitude (0.5 mT) was in some cases used to enhance broad, low intensity components. The time spent on each measurement was adapted according to the spectral lineshape, i.e., the aggregation time, and they could last from 20 minutes to 1 hour. The spin concentration was determined by comparing the double integral of the EPR spectra with the double integral of a reference sample in buffer (label concentration 100 µM). The spin concentrations were ≈ 10 µM for a total protein concentration of 100 µM.

Preparation of fibril enriched sample

To prepare a fibril enriched sample, 300 µL of the aggregating solution were centrifuged with an airfuge (Beckman Coultier, Brea, USA) at 65000 rpm for ten minutes. The surnatant was removed, and the pellet re-suspended in assay buffer. The procedure was repeated three times, after which most of the monomers and free label were removed from the solution. Finally, 20 µL of the re-suspended pellet were used for EPR measurement as described in “EPR measurement conditions”.

Simulations of EPR Spectra

EPR spectra were baseline corrected using WinEPR software (Bruker, Reinstetten, Germany). MATLAB (version 9.4.0.813654, R2019a, The MathWorks, Inc., Natick, MA, USA) and the EasySpin package (5.3.5) were used for simulations of the EPR spectra [28]. The simulations were performed as described by Zurlo et al. [25]: the parameters of the simulation were manually adjusted to agree best with the experimental spectra. For all simulations, an isotropic rotation of the nitroxide (S=1/2) and a common set of g- and A-tensor principal values were used: g = [2.0090 2.0068 2.0030], A = [13 13 109] MHz. A superposition of three components was used, simulated with the "chili" function and differing based on rotational correlation time. The τ_r obtained at t=0 was kept constant for all other simulations as the correlation time for the fast (monomer) fractions. The τ_r for aggregates was derived from spectra acquired from fibril enriched samples. The error margins on the correlation time used for simulation of the slow component are determined by manually adjusting the τ_r, until the simulation was not a good fit for the experimental spectrum anymore. A very fast component was assigned to free label. The τ_r values of each of the fractions were kept constant for the entire series. For each time point, the relative contribution of the components was optimized. In [25], a component was used to define medium sized aggregates. In this work, the approach presented in Zurlo [25] is simplified to include two components, eliminating the component with intermediate τ_r. In the early stages of the aggregation, the signal-to-noise ratio of the broad component is low, and a wide range of τ_r can be used to simulate the spectrum, including the τ_r used for simulation of fibril enriched spectra. Error margins on τ_r and on the contribution of the EPR component to the spectrum were derived by manually adjusting the simulation parameters, until they would not reproduce the experimental spectrum anymore. The data presented in this work for aS56R1 were collected in our laboratory and previously published in [25], and were reanalyzed in the present study with the updated analysis method.

3.3 Results

The aggregation of α-Synuclein (αS) is probed by site-directed-spin-labeling (SDSL)-EPR and Thioflavin T (ThT) fluorescence, as described in Materials and methods. The protein was labelled with MTSL (*S*-(1-oxyl-2,2,5,5-tetramethyl-2,5-dihydro-1H-pyrrol-3-yl)methyl methanesulfonothioate) in position S9 (αS9R1), A27 (αS27R1) and A56 (αS56R1). Also two other labels, MAP (3-Maleimido,2,2,5,5-tetramethyl-1-pyrrolidinyloxy) and IAP (3-(2-Iodoacetamido)-2,2,5,5- tetramethyl-1-pyrrolidinyloxy), were probed, in position 56. The two spin-label variants are referred to αS56R2 (IAP) and αS56R3 (MAP). All experiments are performed with a 9:1 mixture of αS wt and the spin labelled αS variant, respectively. To

illustrate the overall behavior of the spectra and the analysis, we first describe the results for αS56R1, next, the results of the different label positions and the different labels are described.

Figure 3 shows the spectra acquired at different time points of the aggregation of αS56R1. The spectra are dominated by the classical three-line component observed for nitroxides in fast motion, where the three lines arise from the interaction of the unpaired electron spin with the nearby ^{14}N nucleus. Over time, a spectral component with a broader linewidth appears, coming from species with larger rotational correlation times (τ_r), and the intensity of broad component relative to the narrow line component increases during the incubation. Spectral simulation was performed to determine the correlation time and the relative contribution of such components to the EPR lineshape. The spectra were simulated using two components, designated as “fast” and “slow”, which are shown in figure 4A. The fast component is attributed to monomeric αS, and its τ_r was obtained from the EPR spectrum acquired before the start of the aggregation. The slow component is assigned to aggregates, and its τ_r was determined from a fibril- enriched sample, prepared as described in Materials and methods (see SI for fibril spectra). All the spectra acquired for different mutants and labels were simulated with this two-component model. The rotational correlation times for the different spectral components in all samples are given in table 1, and the remaining parameters in Materials and methods. All experimental spectra and simulations are shown in the SI.

By simulating the spectra acquired over the time of the incubation, the time developments of the contribution for the fast and slow components were extracted. Figure 4B shows the time development of the EPR components for αS56R1, alongside the ThT fluorescence intensity. In figure 4B, the contribution of the fast component decreases over time, while the slow component increases, reaching a plateau at later stages of aggregation. It can be noticed that the slow component is already present at early times of the incubation, in the first 15 hours, when the ThT assay is not detecting any fibrillary aggregates yet. A similar time evolution was observed for αS9R1 and αS27R1 as shown in figure 5.

A direct comparison of the development of the slow component over time of αS56R1, αS9R1 and αS27R1 is given in figure 6A. During the early stages of aggregation (first ten hours), the

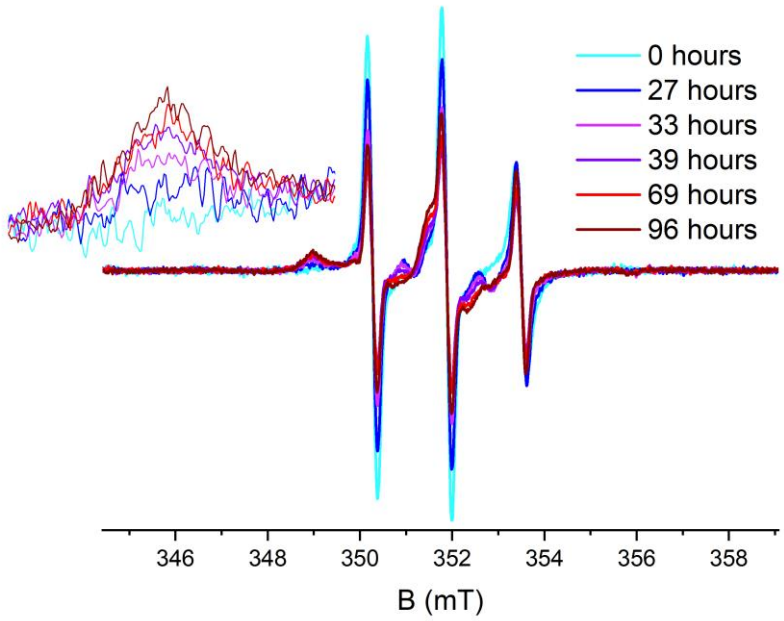

Figure 3. EPR spectra obtained at different time points during the aggregation of aS56R1. In the inset, a zoom-in of the broad spectral component arising from aggregates. Spectra are normalized to double

slow- component contribution is higher for αS27R1, compared to αS56R1 and αS9R1. However, at later stages of aggregation, αS9R1 reaches a plateau after 75 hours, later than αS27R1 and αS56R1, for which the plateau is developed after 50 hours of incubation. The ThT fluorescence curves for all mutants (figure 6C), show no significant differences.

Figure 6B and D show the comparison of the development of slow components and ThT curves for different labels (MTSL-R1, MAP-R2 and IAP-R3) for the A56C mutant. No significant differences are observed between αS56R1 and αS56R2. In contrast, deviations occur in the case of αS56R3, where the exponential growth phase stops after 20 hours of incubation, to resume and reach a plateau after 75 hours of incubation. For αS56R3, ThT shows that the aggregation itself is delayed relative to R1 and R2. As all samples contain only 10% of the labelled protein, the delay for R3 is unlikely related to the spin-label structure and we attribute it to a random change in aggregation.

In all samples, an additional very fast (very short τ_r) component is present in the EPR spectrum. The τ_r is such that it can only be due to free label. In figure 7, the time development of the free-label component is given for the different labels used, and in the SI it is given also for αS9R1 and αS27R1. For αS56R1, the free-label component increases over time, suggesting detachment of the label from the protein. This effect is even more pronounced for αS56R3, where the free label component accounts for almost 60% of the spectral lineshape after 200 hours of aggregation. In contrast, for αS56R2, the free label component remains constant during the incubation, suggesting that free spin label was already present at the start of the incubation, rather than detaching over time.

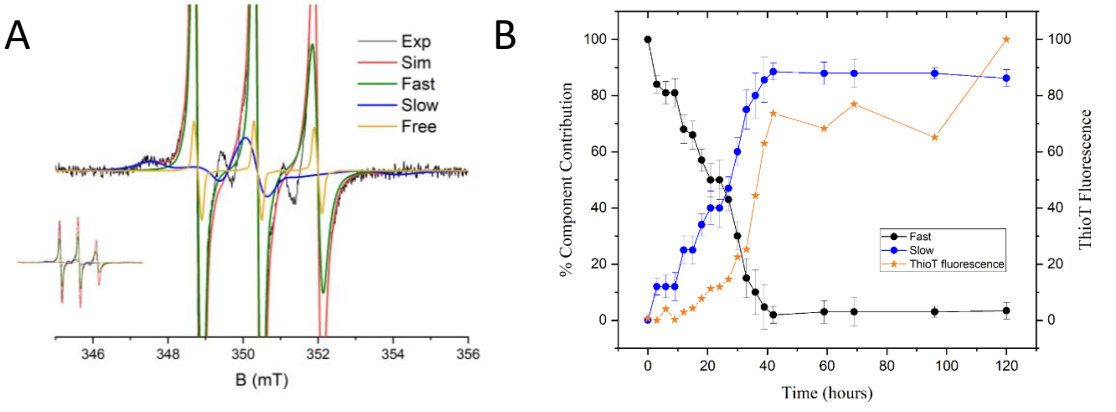

Figure 4. Overview of the aggregation process. EPR spectra, simulation components and time development of simulation components for αS56R1. The experimental spectrum simulated here is obtained after 18 hours of incubation. A) Simulation performed with fast and slow components. Inset: full spectrum. B) Time development of the fast and slow components shown in A). An additional component with the correlation time of free label in solution appears over time, and is added to the simulation. A): black: experimental spectrum. Red: total simulation. Green: fast (monomer) component. Blue: slow (aggregates) component. Yellow: free label component. The data presented in this figure were collected in our laboratory and previously published in [25].

Table 1. Rotational correlation times used for simulation of fast, medium and slow components. The monomer correlation times are obtained from monomer spectra. The correlation times of fibrils are obtained from a fibril enriched sample. For details, see main text

	Monomer τ_r (ns)	**Fibril τ_r (ns)**
αS56R1	0.41	7.28 ± 1.34*
αS56R3	0.31	7.04 ± 1.45
αS56R2	0.38	6.6 ± 1.86
αS27R1	0.40	6.35 ± 1.46
αS9R1	0.37	7.94 ± 0.7

*The rotational correlation time used in [25] for the slow fraction is 10 ns.

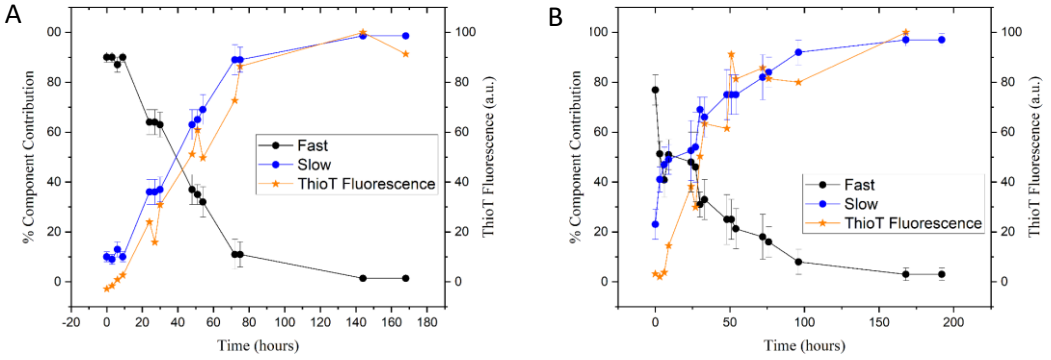

Figure 5. Development of ThioT fluorescence and EPR simulation components over time, for αS9R1 mutant (A) and αS27R1 mutant (B). The solid lines are a guide to the eye.

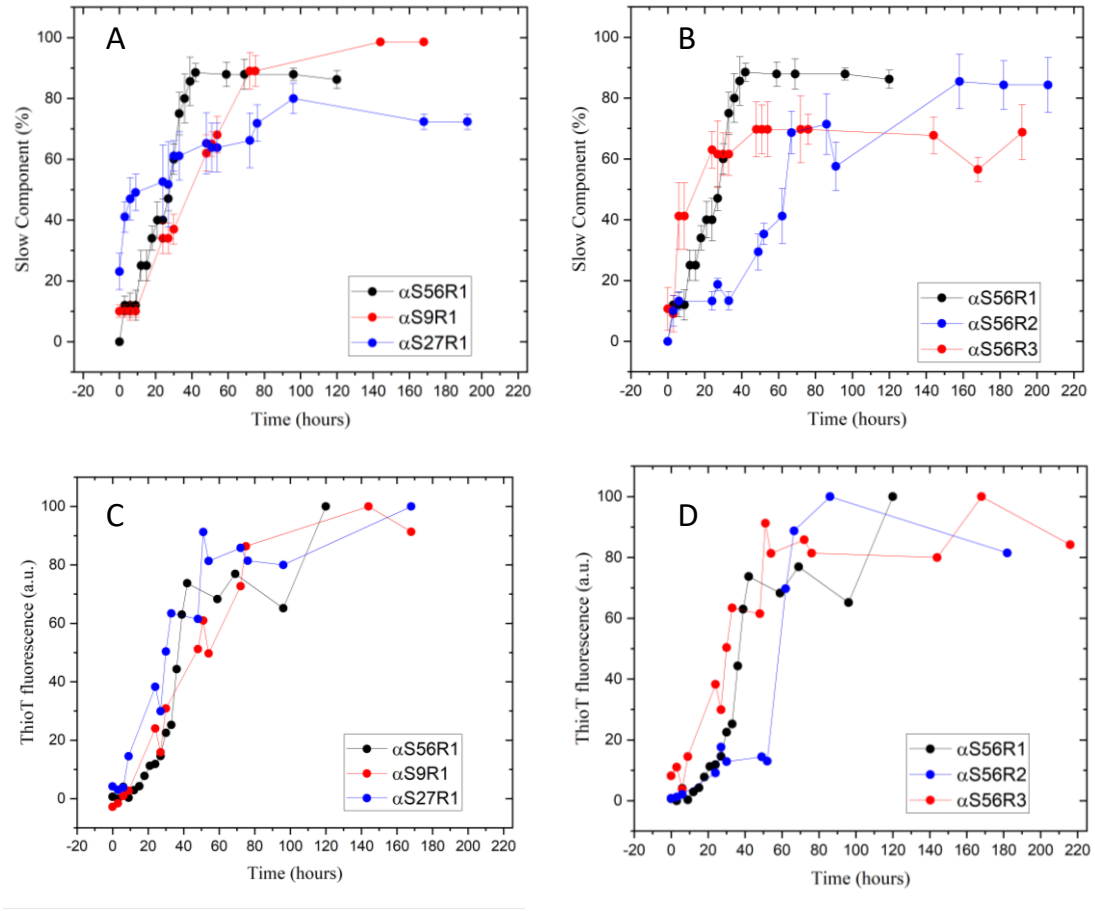

Figure 6. Comparison of the time development of slow component for different mutants (A) and labels (B). Comparison of ThioT fluorescence curves for different mutants (C) and different labels (D).

3.4 Discussion

The method of monitoring αS aggregation in situ with EPR was first reported by Zurlo et al, with αS labelled in position 56 [25]. Here, we extended the investigation to probe the positions 9 and 27, and two additional types of spin labels. In addition, the data were analyzed with improved simulations, providing a more systematic investigation of the in situ αS aggregation by SDSL EPR.

The aggregation is monitored by the CW EPR spectrum, which is sensitive to the τ_r of the nitroxide moiety. The local mobility of the bonds linking the nitroxide to the protein backbone, see figure 2, together with the flexibility of αS, are dominating the spectral line shape. In its monomeric form, αS has a spectrum characteristic of a relatively fast rotating nitroxide (see figure 3). If αS aggregates, the nitroxide rotation becomes hindered by the interaction of the label with other monomers, leading to a longer τ_r and spectral broadening. During aggregation, spin labels may come in close proximity within the aggregates, leading to spectral broadening due to spin-spin interactions, such as exchange coupling. To prevent this effect and ensure that spectral changes reflect differences in mobility rather than label-label interactions, the labeled protein is diluted with wild-type αS (diamagnetic dilution), increasing the average nitroxide-nitroxide distance within the aggregates.

Figure 1 shows that amyloid aggregation involves the formation of multiple aggregate species that differ in structure and size. In the course of incubation, aggregates form and the spectra will be a superposition of the spectra of all these different aggregates present in solution. As the spectra of these aggregates are expected to differ, at least three different mobility components (figure 1), with distinct τ_r, corresponding to monomers, intermediates and fibrils are expected. For two of these components, τ_r values can be determined experimentally (monomers and fibrils, see results). In Zurlo et al. [25] three components were used, one for monomers, one for intermediates and one for fibrils. However, the τ_r for intermediate species cannot be directly extracted from experimental data, and, as shown in [26], the τ_r values of intermediates and fibrils overlap within uncertainty margins, making their spectral contributions interchangeable.

Extensive analysis of the data and testing different simulation parameters revealed that the τ_r experimentally determined from fibrils can be used to simulate the spectral component observed at early time points, where its contribution is weak relative to the overall spectrum. Given the larger dataset obtained in the present study and the need to streamline the analysis while avoiding bias, we opted for this more robust model. By using the τ_r obtained from fibrils to represent all aggregated species, both intermediates and fibrillary aggregates contribute to the same EPR spectral component. However, only fibrils show ThT

fluorescence, so by monitoring the aggregation with ThT in parallel to the EPR experiments, the non-ThT active contribution of the oligomers is identified.

Structural information from in situ EPR

In principle, EPR can provide local structural information by revealing how specific regions of a protein are incorporated into an aggregate. Therefore, by labeling different positions (9, 27 and 56) in the present study, variations in immobilization within the aggregates can be observed and offer insights into structural features of the aggregates.

As for fibrils there is independent information on structure [7-13], we test the ability of the EPR approach to obtain such structural information. It is known [7-13], that in the fibril state position 56 is situated in the fibril core, while 9 and 27 are positioned on the outside of the fibrils, suggesting that the αS positions studied in the present work reflect these differences. For this reason, position 9 and 27 were expected to have a higher mobility in EPR, i.e. shorter τ_r, than position 56. However, the τ_r of the slow (fibril) component is, within error margins, the same for the different mutants analyzed (see table 1 for correlation times, and SI for spectra). This suggests that EPR at 9 GHz does not have sufficient resolution to differentiate between the αS positions investigated here.

What we observed, however, is that the time development of the slow component is different in the different mutants, suggesting that the time course of the development of the

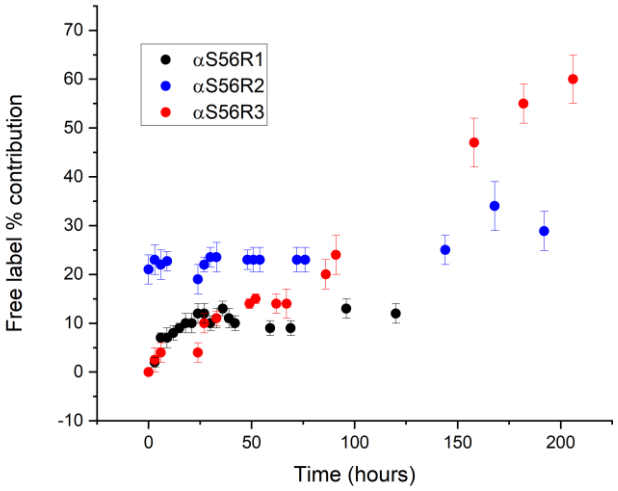

Figure 7. Free label contribution to the αS aggregation EPR spectra over time. Amount of free label in each spectrum is obtained by spectral simulation, see main text and materials and methods. Black: αS56R1. Red: αS56R2. Blue: αS56R3.

EPR spectral contributions can be used to obtain structural information. This requires that the aggregation-time course is not influenced by the label position. That is the case is proven by the ThT curves, where the aggregation process has the same time course, unaffected by the labels, proving that this condition is met (fig. 6C). Therefore, the observation that the slow component of αS9R1 reaches a plateau later than αS56R1 and αS27R1 suggests that position 9 does not take part in the initial fibrillization. Position 9 in fibrils is reported to be in the highly mobile tail end, outside of the fibril core, in agreement with this observation. On the other hand, position 27, which is closer to the fibril core but still outside of it, does not exhibit the same behavior as position 9. Perhaps its position close to the fibril core plays a role, however, the ultimate reason is unknown so far.

Next, we turn to the intermediates. As the fibril results suggest that time development of the EPR components can be used to obtain structural information, we apply it to the much more difficult to study intermediates of aggregation. In the time frame where oligomers occur, i.e. in the first 10-20 hours of the aggregation, αS27R1 is more immobilized than αS9R1 and αS56R1. This suggests that the region of αS around 27 is incorporated into the oligomers first, only to be followed by the regions around positions 9 and 56. Expanding this initial set of positions to other regions of αS could be expected to give a first indication about the location of residues in the oligomers, a first step to obtaining oligomer structure information.

Comparison of different labels

To probe spin labels with different linking groups, position 56 was labelled also with IAP (aS56R2) and MAP (aS56R3). Their respective linking groups have different chemical stabilities. While MTSL forms a disulfide bond that can be reduced, MAP and IAP form non-reducible bonds with the cysteine of the protein. Therefore, they can be used in the presence of reducing agents, like TCEP, required for some biomolecules to function in vitro. In MAP the bond is a thioether bond, in IAP a thioamide group (figure 2). Our results show that MTSL progressively detaches from the protein during the incubation, which is somewhat unexpected, because no reducing agent is added to the solution. While MAP behaves as expected, as it does not detach, it is unclear why IAP would detach in the time course of the aggregation. These results suggest to use MAP in situations where long incubations at relatively high temperature (37˚ C) are needed. Due to its higher stability, MAP is also a better choice for studies in reducing environments, like in cell studies, or partner interaction assays [29].

3.5 Conclusions

Overall, the data obtained so far highlight the strength of the in situ EPR approach in obtaining structural information on the intermediates of αS aggregation. This includes meta-stable, short lived species that would otherwise be removed from the solution with different approaches that involve chemical modification or dilution [14, 16-21]. By systematically applying in situ EPR with different label positions and comparing them, it could be possible to obtain site specific structural information on oligomeric species.

An additional possibility to gain more information is by allowing some exchange interaction to occur, if diamagnetic dilution is reduced. In this case exchange coupling becomes a major interaction in aggregates, and different degrees of diamagnetic dilution can be used to gain structural information as shown in [30, 31]. It is also possible that extending the method to higher EPR frequency, that provide better spectral resolution, would allow to observe τ_r differences between different label positions inside aggregates, and also to detect other mobility components that are hidden in the 9 GHz EPR nitroxide spectrum [32].

We demonstrate that the in situ EPR approach is a promising tool for studying αS aggregation, and for investigating transient intermediates that are otherwise difficult to capture. Future work could extend this method to higher EPR frequencies and additional label positions in αS, enhancing the capability to obtain site-specific structural insights into oligomeric species.

Supplementary Information

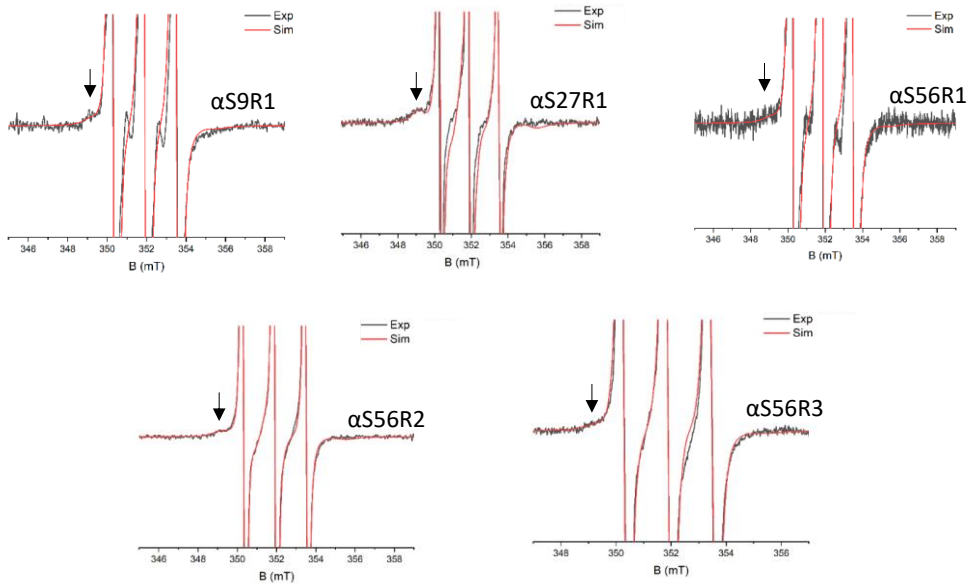

Figure SI.1. Zoom in on room temperature continuous wave EPR spectra of the different αS variants studied in this work. All spectra shown were acquired after six hours of aggregation. Black: experimental spectrum. Red: simulation. The arrows indicate the broad component, attributed to aggregates.

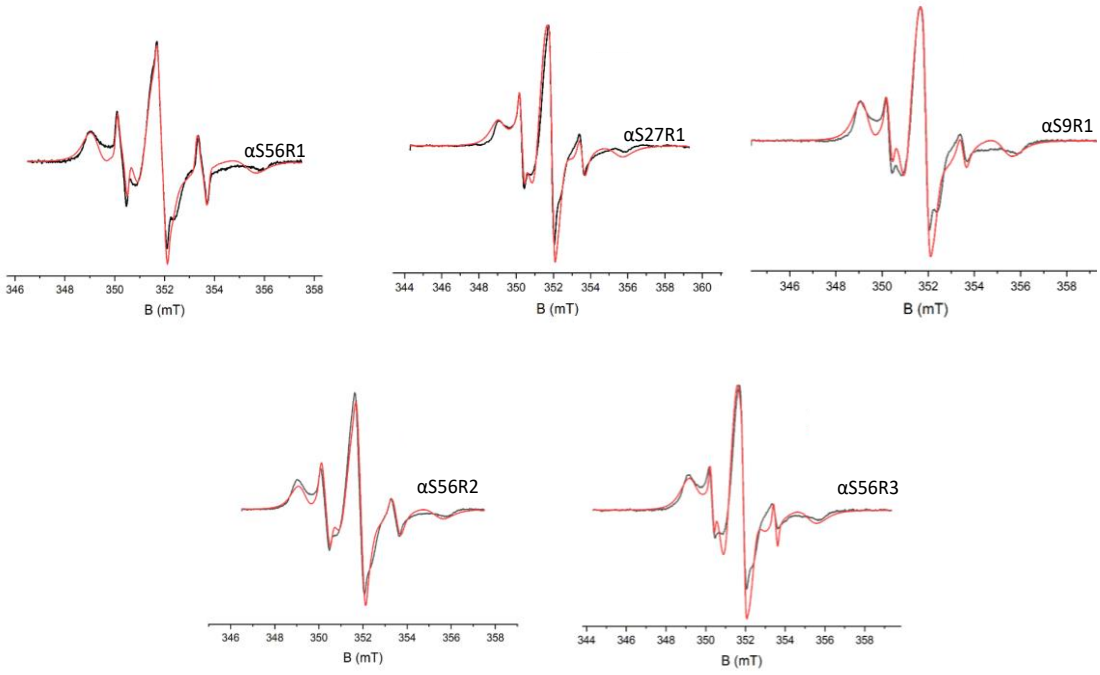

Figure SI.2. CW-EPR spectra obtained from fibril enriched samples. Black: experimental spectrum, red: simulation. For details, see main text.

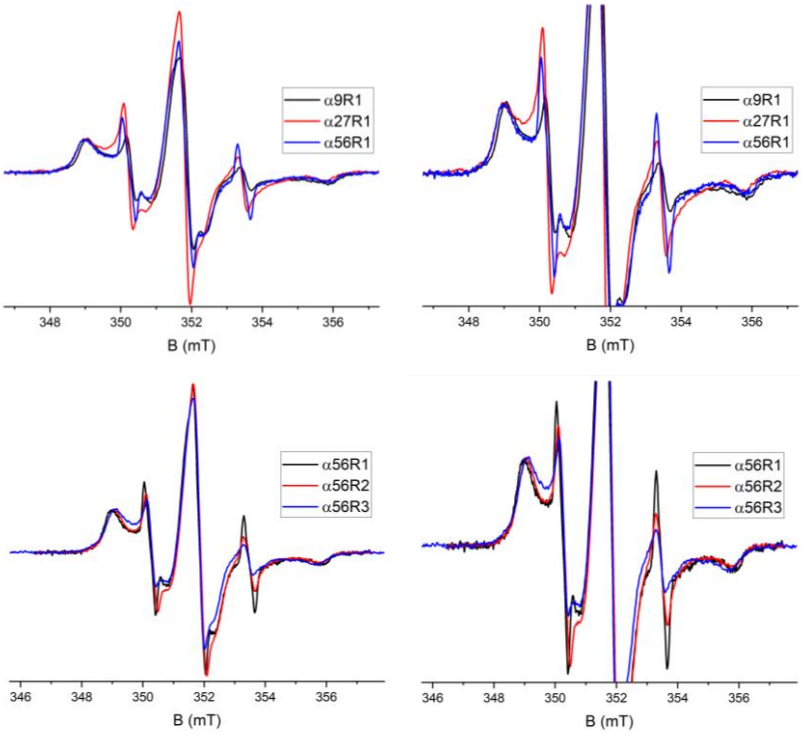

Figure SI.3. Comparison of experimental spectra obtained from fibril enriched samples from different mutants (upper two spectra) and different labels (lower two). The spectra are normalized to the intensity of the broad component around 349 mT. Left: full spectra, right: zoom in for better visualization.

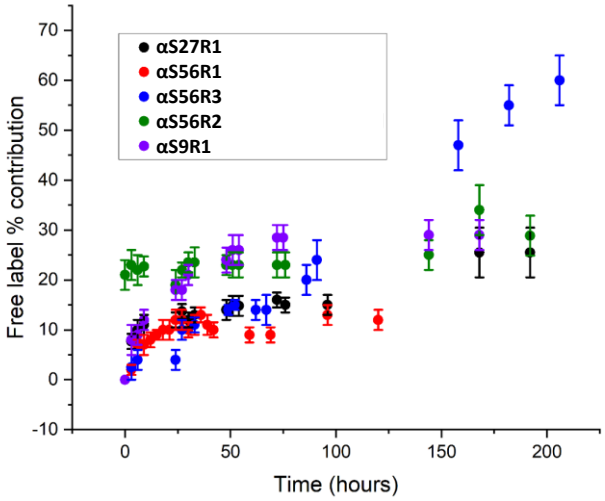

Figure SI.4 Free label contribution to the αS aggregation EPR spectra over time. Amount of free label in each spectrum is obtained by spectral simulation, see main text and materials and methods. Black: αS27R1. Red: αS56R1. Blue: αS56R3. Green: αS56R2. Purple: αS9R1

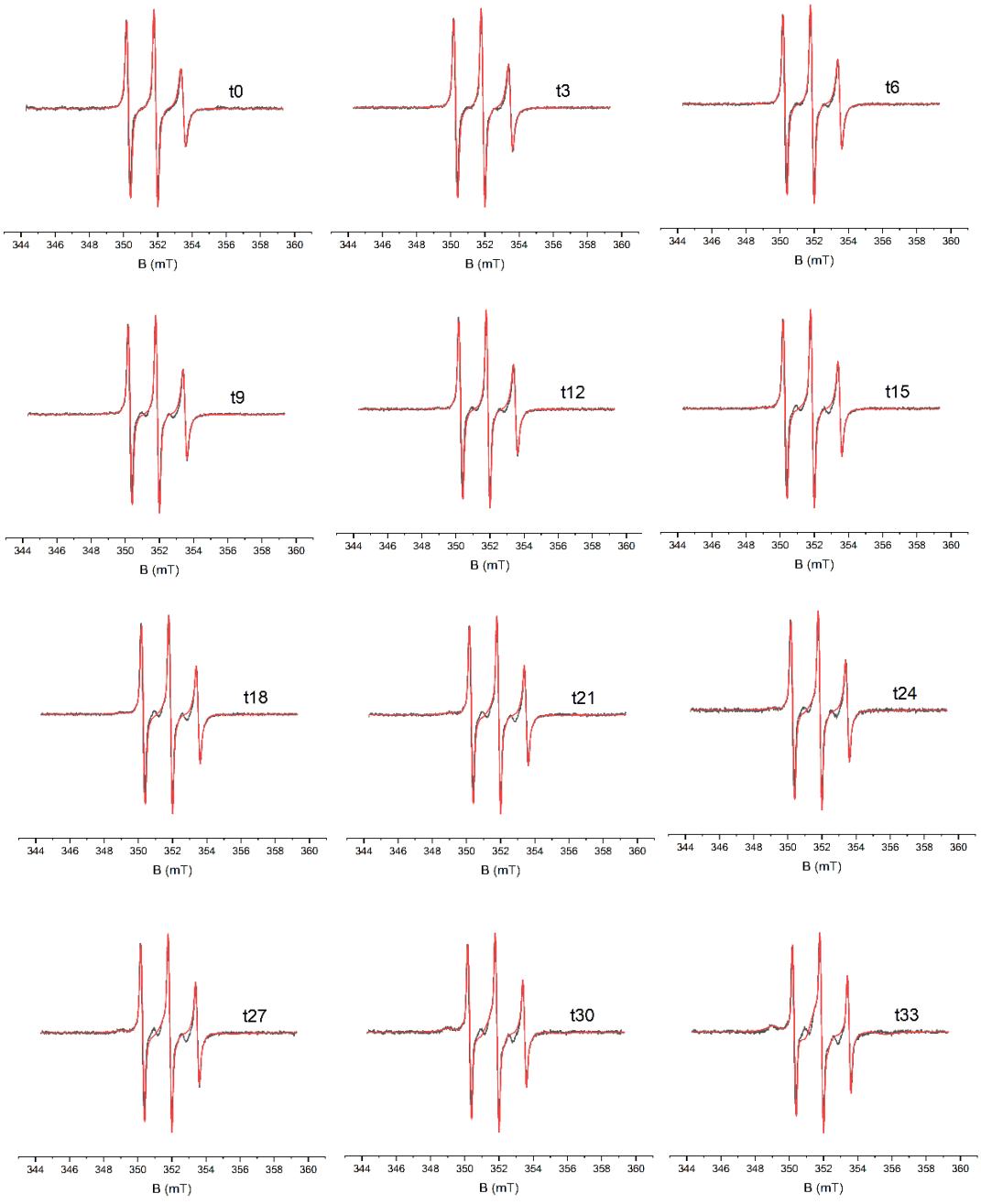
t0
t3
t6
t9
t12
t15
t18
t21
t24
t27
t30
t33
344 346 348 350 352 354 356 358 360
B (mT)

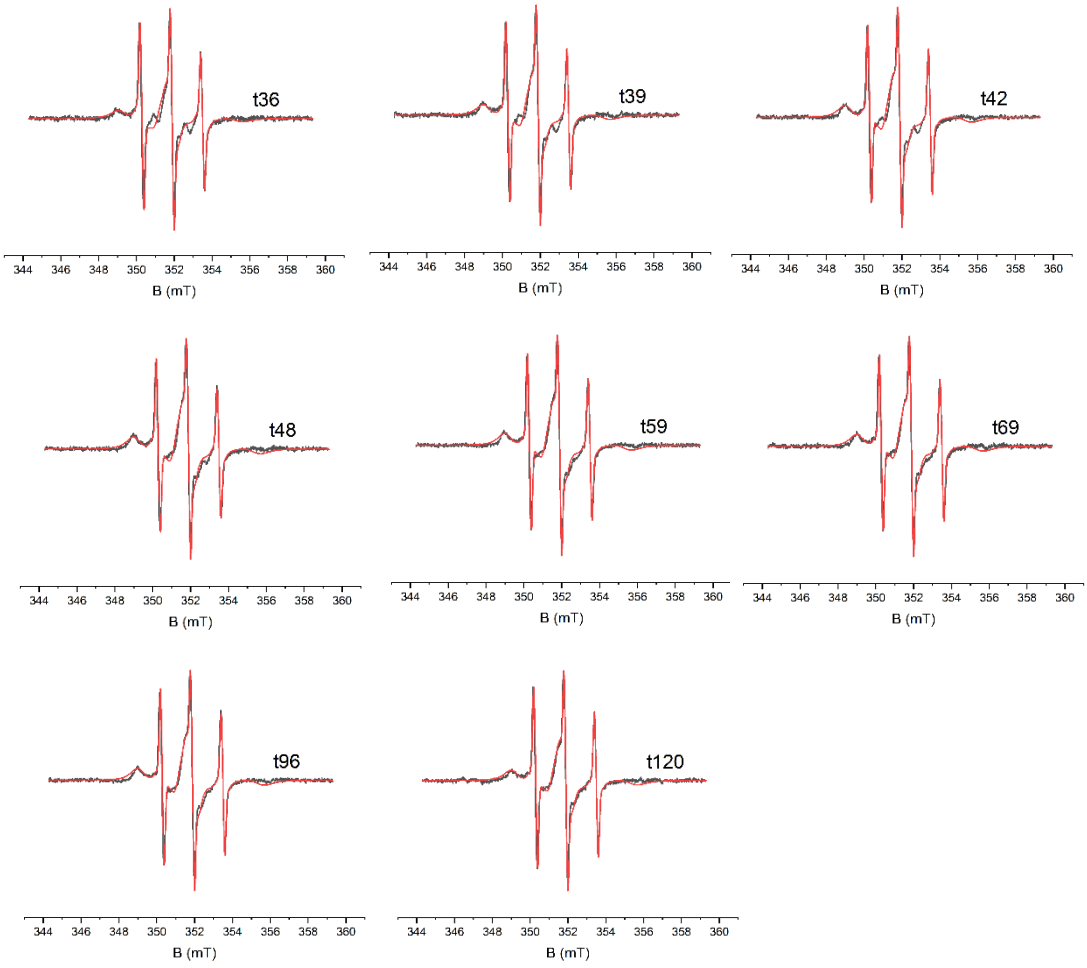

Figure SI.5. CW-EPR spectra obtained for αS56R1. Black: experimental spectrum. Red: simulation. The spectra presented for αS56R1 are the same as published in [25]. The simulations are updated to the method described in main text.

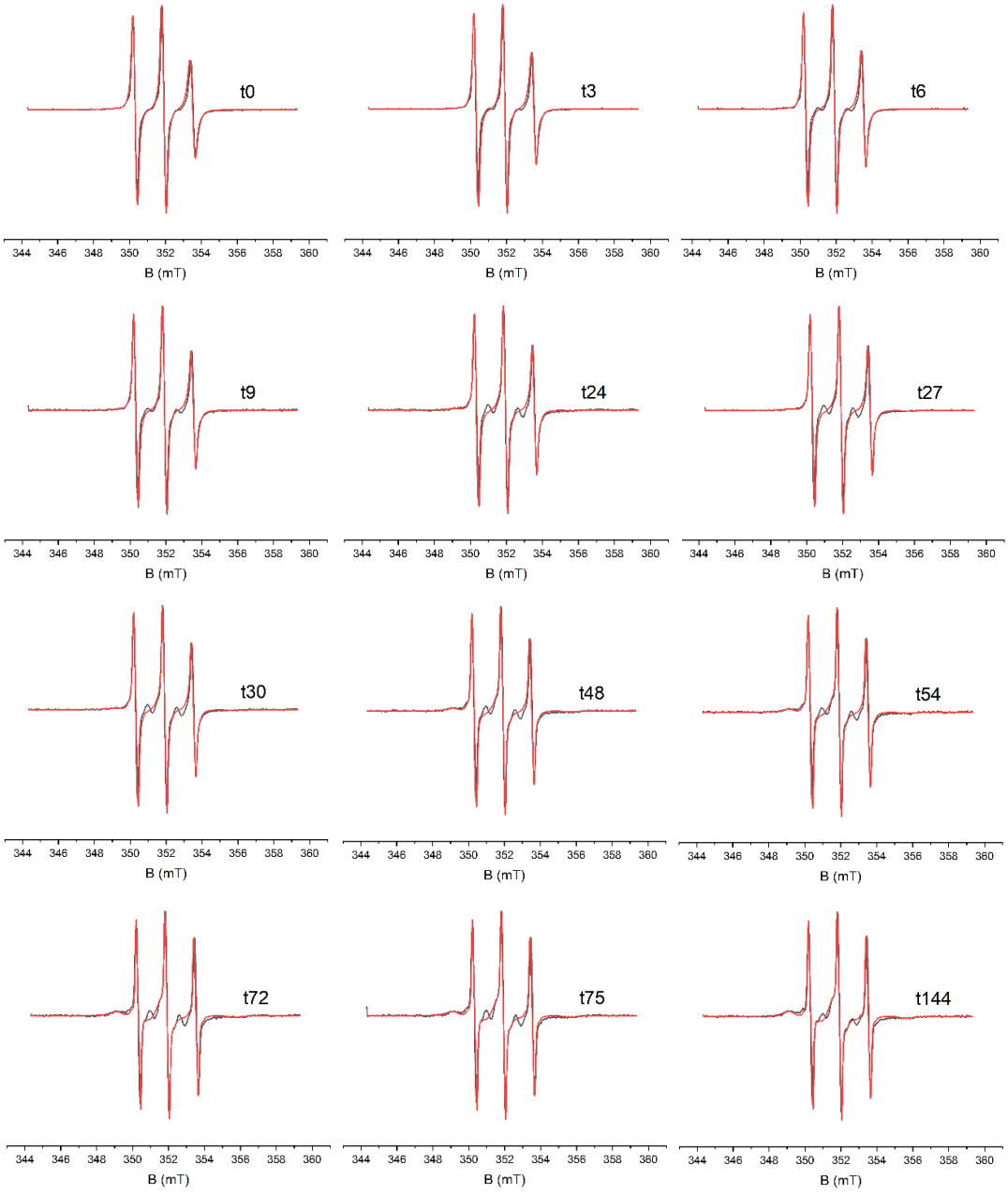
t0
t3
t6
t9
t24
t27
t30
t48
t54
t72
t75
t144
344 346 348 350 352 354 356 358 360
B (mT)

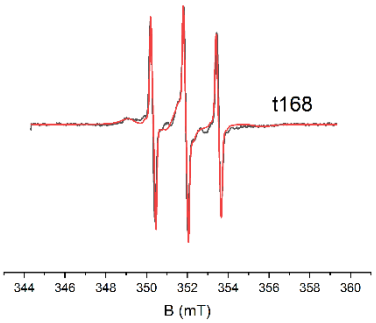

Figure SI.6. CW-EPR spectra obtained for αS9R1. Black: experimental spectrum. Red: simulation.

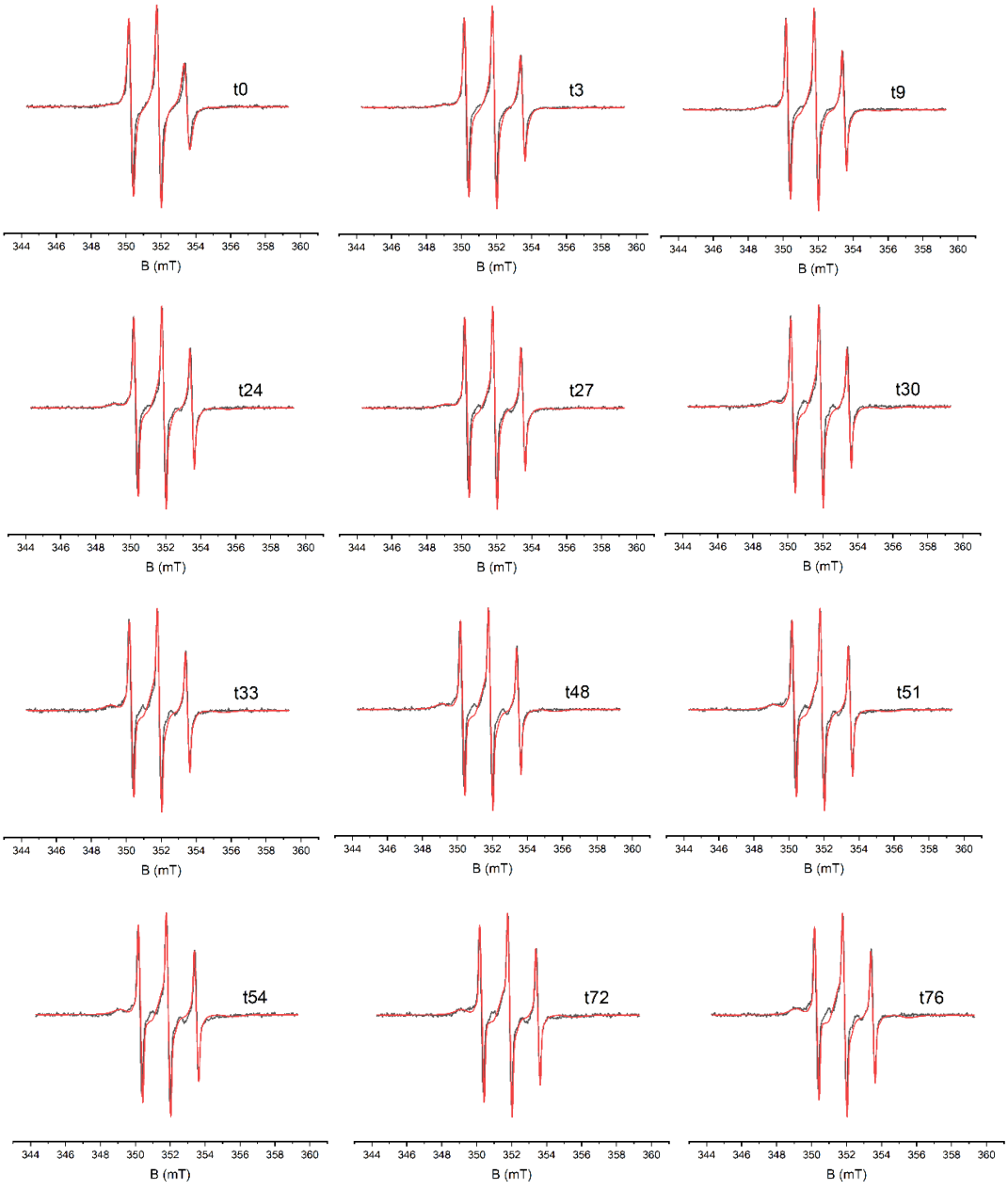
t0
t3
t9
t24
t27
t30
t33
t48
t51
t54
t72
t76
344 346 348 350 352 354 356 358 360
B (mT)

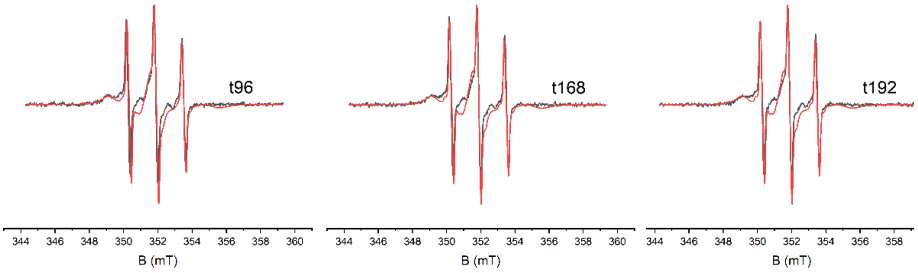

Fig. SI 7. CW-EPR spectra obtained for αS9R1. Black: experimental spectrum. Red: simulation.

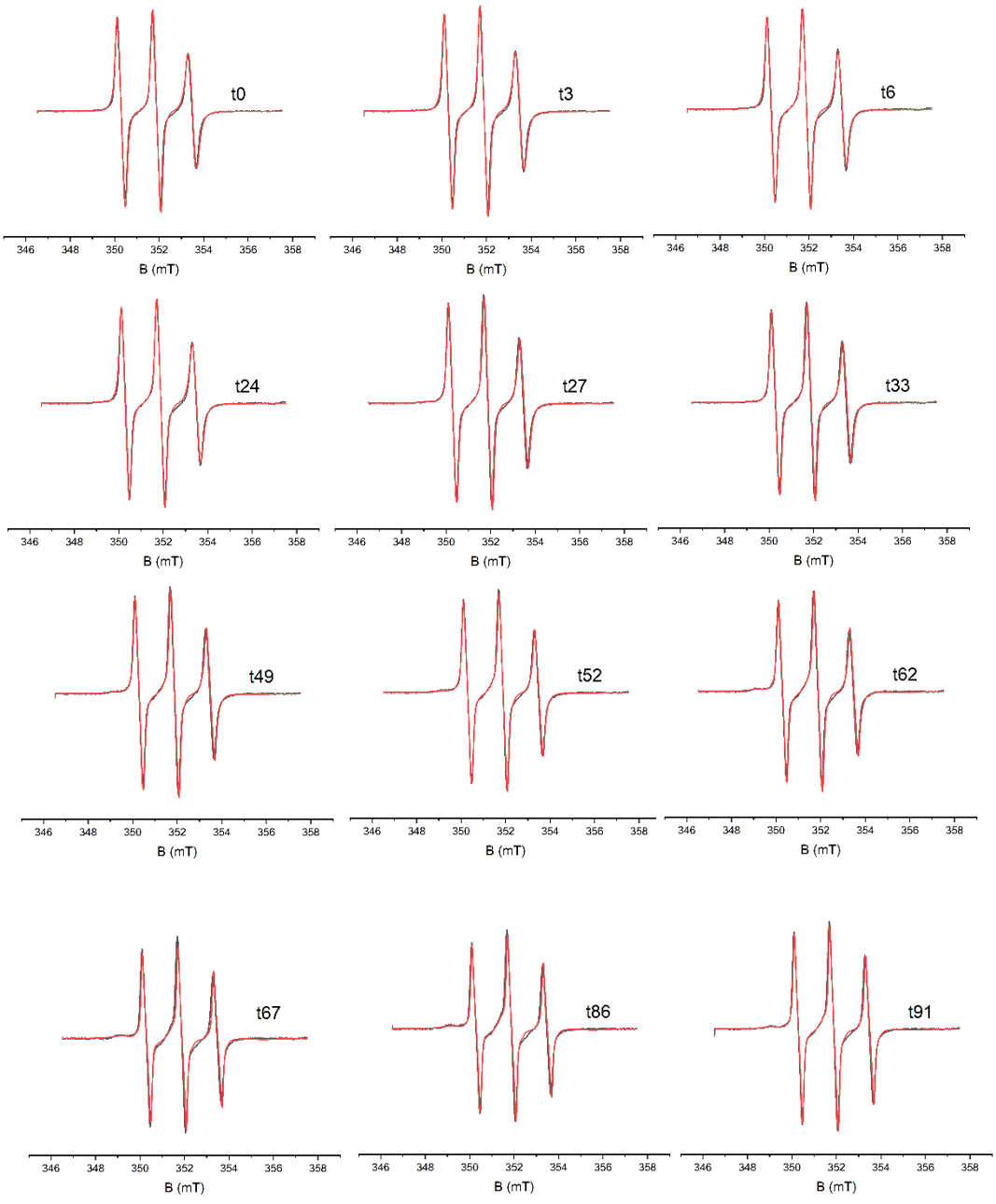
t0
t3
t6
t24
t27
t33
t49
t52
t62
t67
t86
t91
346 348 350 352 354 356 358
B (mT)

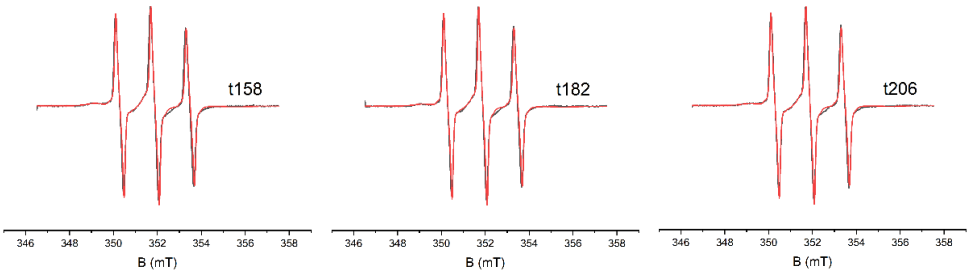

Figure SI.8. CW-EPR spectra obtained for αS56R2. Black: experimental spectrum. Red: simulation.

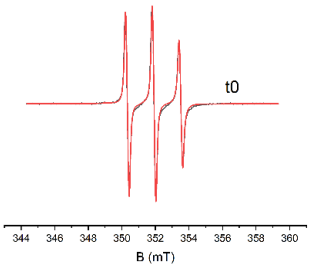
t0
344 346 348 350 352 354 356 358 360
B (mT)

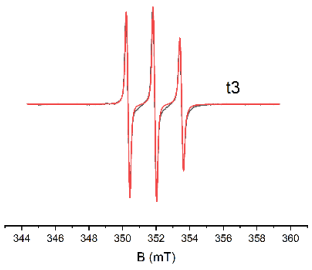
t3
344 346 348 350 352 354 356 358 360
B (mT)

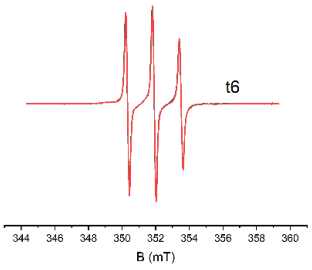
t6
344 346 348 350 352 354 356 358 360
B (mT)

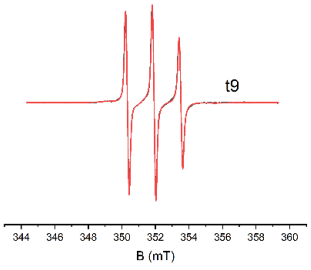
t9
344 346 348 350 352 354 356 358 360
B (mT)

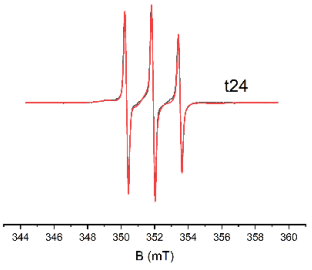
t24
344 346 348 350 352 354 356 358 360
B (mT)

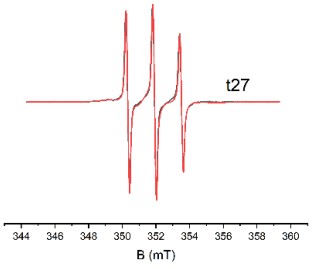
t27
344 346 348 350 352 354 356 358 360
B (mT)

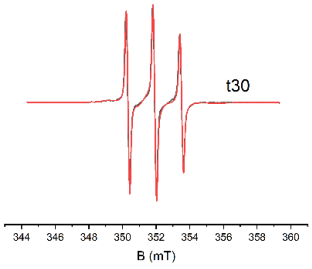
t30
344 346 348 350 352 354 356 358 360
B (mT)

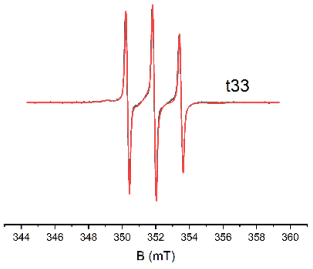
t33
344 346 348 350 352 354 356 358 360
B (mT)

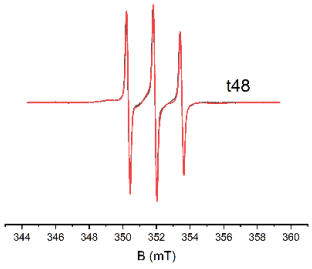
t48
344 346 348 350 352 354 356 358 360
B (mT)

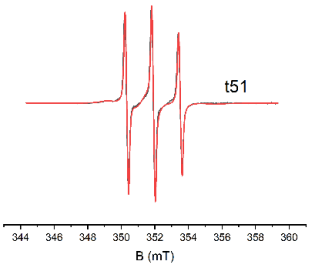
t51
344 346 348 350 352 354 356 358 360
B (mT)

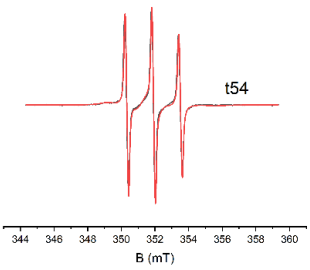
t54
344 346 348 350 352 354 356 358 360
B (mT)

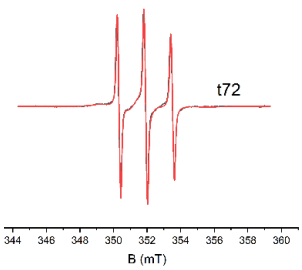
t72
344 346 348 350 352 354 356 358 360
B (mT)

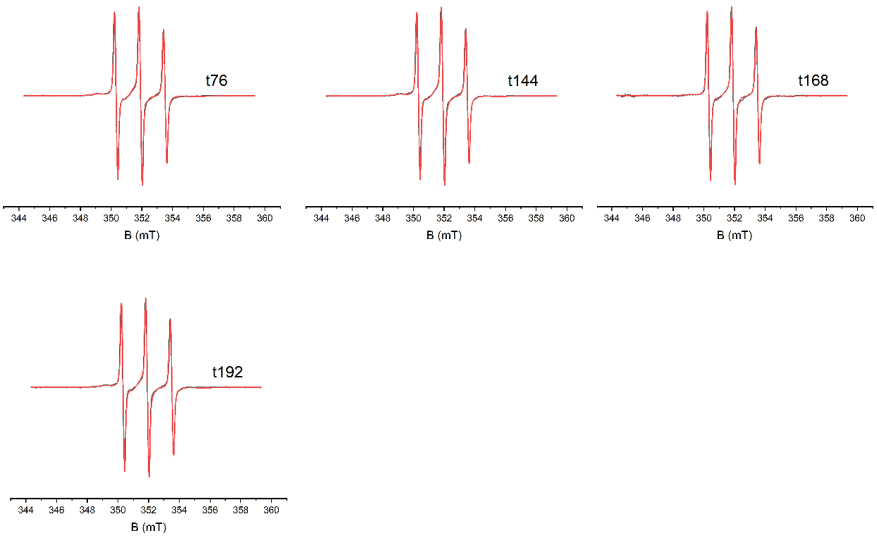

Figure SI.9. CW-EPR spectra obtained for αS56R3. Black: experimental spectrum. Red: simulation.

References

[1] L.M.A. Oliveira, T. Gasser, R. Edwards, M. Zweckstetter, R. Melki, L. Stefanis, H.A. Lashuel, D. Sulzer, K. Vekrellis, G.M. Halliday, J.J. Tomlinson, M. Schlossmacher, P.H. Jensen, J. Schulze-Hentrich, O. Riess, W.D. Hirst, O. El-Agnaf, B. Mollenhauer, P. Lansbury, T.F. Outeiro, Alpha-synuclein research: defining strategic moves in the battle against Parkinson's disease, npj Parkinson's Disease 7(1) (2021) 65.

[2] P. Calabresi, G. Di Lazzaro, G. Marino, F. Campanelli, V. Ghiglieri, Advances in understanding the function of alpha-synuclein: implications for Parkinson's disease, Brain 146(9) (2023) 3587-3597.

[3] A. Villar-Piqué, T. Lopes da Fonseca, T.F. Outeiro, Structure, function and toxicity of alpha-synuclein: the Bermuda triangle in synucleinopathies, Journal of Neurochemistry 139(S1) (2016) 240-255.

[4] P. Calabresi, A. Mechelli, G. Natale, L. Volpicelli-Daley, G. Di Lazzaro, V. Ghiglieri, Alpha-synuclein in Parkinson's disease and other synucleinopathies: from overt neurodegeneration back to early synaptic dysfunction, Cell Death & Disease 14(3) (2023) 176.

[5] P. Arosio, T.P.J. Knowles, S. Linse, On the lag phase in amyloid fibril formation, Physical Chemistry Chemical Physics 17(12) (2015) 7606-7618.

[6] N. Bengoa-Vergniory, R.F. Roberts, R. Wade-Martins, J. Alegre-Abarrategui, Alpha-synuclein oligomers: a new hope, Acta Neuropathologica 134(6) (2017) 819-838.

[7] M.D. Tuttle, G. Comellas, A.J. Nieuwkoop, D.J. Covell, D.A. Berthold, K.D. Kloepper, J.M. Courtney, J.K. Kim, A.M. Barclay, A. Kendall, W. Wan, G. Stubbs, C.D. Schwieters, V.M.Y. Lee, J.M. George, C.M. Rienstra, Solid-state NMR structure of a pathogenic fibril of full-length human α-synuclein, Nature Structural & Molecular Biology 23(5) (2016) 409-415.

[8] J. Gath, L. Bousset, B. Habenstein, R. Melki, B.H. Meier, A. Bockmann, Yet another polymorph of alpha-synuclein: solid-state sequential assignments, Biomol NMR Assign 8(2) (2014) 395-404.

[9] J. Gath, B. Habenstein, L. Bousset, R. Melki, B.H. Meier, A. Böckmann, Solid-state NMR sequential assignments of α-synuclein, Biomolecular NMR Assignments 6(1) (2012) 51-55.

[10] J. Verasdonck, L. Bousset, J. Gath, R. Melki, A. Bockmann, B.H. Meier, Further exploration of the conformational space of alpha-synuclein fibrils: solid-state NMR assignment of a high-pH polymorph, Biomol NMR Assign 10(1) (2016) 5-12.

[11] R. Guerrero-Ferreira, N.M. Taylor, A.A. Arteni, P. Kumari, D. Mona, P. Ringler, M. Britschgi, M.E. Lauer, A. Makky, J. Verasdonck, R. Riek, R. Melki, B.H. Meier, A. Bockmann, L. Bousset, H. Stahlberg, Two new polymorphic structures of human full-length alpha-synuclein fibrils solved by cryo-electron microscopy, Elife 8 (2019).

[12] R. Guerrero-Ferreira, L. Kovacik, D. Ni, H. Stahlberg, New insights on the structure of alpha-synuclein fibrils using cryo-electron microscopy, Curr Opin Neurobiol 61 (2020) 89-95.

[13] R. Guerrero-Ferreira, N.M. Taylor, D. Mona, P. Ringler, M.E. Lauer, R. Riek, M. Britschgi, H. Stahlberg, Cryo-EM structure of alpha-synuclein fibrils, Elife 7 (2018).
[14] N. Lorenzen, S.B. Nielsen, A.K. Buell, J.D. Kaspersen, P. Arosio, B.S. Vad, W. Paslawski, G. Christiansen, Z. Valnickova-Hansen, M. Andreasen, J.J. Enghild, J.S. Pedersen, C.M. Dobson, T.P. Knowles, D.E. Otzen, The role of stable alpha-synuclein oligomers in the molecular events underlying amyloid formation, J Am Chem Soc 136(10) (2014) 3859-68.
[15] P. Alam, L. Bousset, R. Melki, D.E. Otzen, α-synuclein oligomers and fibrils: a spectrum of species, a spectrum of toxicities, Journal of Neurochemistry 150(5) (2019) 522-534.
[16] N. Cremades, Samuel I.A. Cohen, E. Deas, Andrey Y. Abramov, Allen Y. Chen, A. Orte, M. Sandal, Richard W. Clarke, P. Dunne, Francesco A. Aprile, Carlos W. Bertoncini, Nicholas W. Wood, Tuomas P.J. Knowles, Christopher M. Dobson, D. Klenerman, Direct Observation of the Interconversion of Normal and Toxic Forms of α-Synuclein, Cell 149(5) (2012) 1048-1059.
[17] S.W. Chen, S. Drakulic, E. Deas, M. Ouberai, F.A. Aprile, R. Arranz, S. Ness, C. Roodveldt, T. Guilliams, E.J. De-Genst, D. Klenerman, N.W. Wood, T.P. Knowles, C. Alfonso, G. Rivas, A.Y. Abramov, J.M. Valpuesta, C.M. Dobson, N. Cremades, Structural characterization of toxic oligomers that are kinetically trapped during alpha-synuclein fibril formation, Proc Natl Acad Sci U S A 112(16) (2015) E1994-2003.
[18] I. Pérez-Pi, D.A. Evans, M.H. Horrocks, N.T. Pham, K.S. Dolt, J. Koszela, T. Kunath, M. Auer, α-Synuclein–Confocal Nanoscanning (ASYN-CONA), a Bead-Based Assay for Detecting Early-Stage α-Synuclein Aggregation, Analytical Chemistry 91(9) (2019) 5582-5590.
[19] L. Zhou, D. Kurouski, Structural Characterization of Individual α-Synuclein Oligomers Formed at Different Stages of Protein Aggregation by Atomic Force Microscopy-Infrared Spectroscopy, Analytical Chemistry 92(10) (2020) 6806-6810.
[20] F. van Diggelen, D. Hrle, M. Apetri, G. Christiansen, G. Rammes, A. Tepper, D.E. Otzen, Two conformationally distinct alpha-synuclein oligomers share common epitopes and the ability to impair long-term potentiation, PLoS One 14(3) (2019) e0213663.
[21] J.I. Gallea, M.S. Celej, Structural Insights into Amyloid Oligomers of the Parkinson Disease-related Protein α-Synuclein*, Journal of Biological Chemistry 289(39) (2014) 26733-26742.
[22] K. Gade Malmos, L.M. Blancas-Mejia, B. Weber, J. Buchner, M. Ramirez-Alvarado, H. Naiki, D. Otzen, ThT 101: a primer on the use of thioflavin T to investigate amyloid formation, Amyloid 24(1) (2017) 1-16.
[23] H. Naiki, K. Higuchi, M. Hosokawa, T. Takeda, Fluorometric determination of amyloid fibrils in vitro using the fluorescent dye, thioflavine T, Analytical Biochemistry 177(2) (1989) 244-249.
[24] H. LeVine, [18] Quantification of β-sheet amyloid fibril structures with thioflavin T, Methods in Enzymology, Academic Press1999, pp. 274-284.

[25] E. Zurlo, P. Kumar, G. Meisl, A.J. Dear, D. Mondal, M.M.A.E. Claessens, T.P.J. Knowles, M. Huber, In situ kinetic measurements of α-synuclein aggregation reveal large population of short-lived oligomers, PLOS ONE 16(1) (2021) e0245548.
[26] E. Zurlo, L. Passerini, P. Kumar, M. Huber, In Situ Continuous Wave Electron Paramagnetic Resonance Investigation of the Amyloid Aggregation of Parkinson's Protein Alpha-Synuclein—the Second Spin-Label Position, Applied Magnetic Resonance 53(7) (2022) 1133-1150.
[27] T. Ikenoue, Y.-H. Lee, J. Kardos, M. Saiki, H. Yagi, Y. Kawata, Y. Goto, Cold Denaturation of α-Synuclein Amyloid Fibrils, Angewandte Chemie International Edition 53(30) (2014) 7799-7804.
[28] S. Stoll, A. Schweiger, EasySpin, a comprehensive software package for spectral simulation and analysis in EPR, J Magn Reson 178(1) (2006) 42-55.
[29] A. Bonucci, O. Ouari, B. Guigliarelli, V. Belle, E. Mileo, In-Cell EPR: Progress towards Structural Studies Inside Cells, Chembiochem 21(4) (2020) 451-460.
[30] H. Xiao, L. Duo, J. Zhen, H. Wang, Z. Guo, Static and dynamic disorder in Aβ40 fibrils, Biochemical and Biophysical Research Communications 610 (2022) 107-112.
[31] M. Chen, M. Margittai, J. Chen, R. Langen, Investigation of alpha-synuclein fibril structure by site-directed spin labeling, J Biol Chem 282(34) (2007) 24970-9.
[32] E. Zurlo, I. Gorroño Bikandi, N.J. Meeuwenoord, D.V. Filippov, M. Huber, Tracking amyloid oligomerization with monomer resolution using a 13-amino acid peptide with a backbone-fixed spin label, Physical Chemistry Chemical Physics 21(45) (2019) 25187-25195.

Chapter 4.
High-Frequency EPR investigation of a Short-Lived Reaction Intermediate in Small Laccase (SLAC)

A publication of the work described in this chapter is in preparation: L. Passerini, E.J.J. Groenen, M. Huber “High-frequency EPR investigation of a short-lived reaction intermediate in Small Laccase (SLAC)”, to be submitted.

4.1 Introduction

Laccases, or Multi-Copper-Oxidases (MCOs), are a class of multi-domain copper enzymes, which catalyze the oxidation of a variety of substrates coupled to the reduction of molecular oxygen to water [1-6]. Those enzymes play essential roles in all types of organisms, from iron metabolism in humans to lignin degradation in bacteria [1, 2, 7]. Especially bacterial laccases are interesting in industrial applications, due to the broad range of substrates and pH and thermal stabilities [6, 8, 9]. The common feature in MCOs is the presence of at least one of three characteristic copper sites: type-1-Cu (T1Cu), type-2-Cu (T2Cu) and type-3-Cu (T3Cu), each with distinct spectroscopic characteristics. The T1Cu shows a strong absorption at 600 nm in the UV-Vis spectrum, and a copper hyperfine splitting in the parallel direction of 100-180 MHz in the 9 GHz EPR spectrum [10, 11]. The T2Cu does not absorb in the UV, and the EPR spectrum shows a larger hyperfine splitting of 500-600 MHz in the parallel direction [3, 10, 11]. The T3Cu consists of two antiferromagnetically coupled copper atoms, rendering it EPR silent, and shows a weak band in the UV-Vis spectrum at 330 nm [3, 10]. For laccases, the T2Cu and T3Cu are in close proximity, forming the trinuclear cluster (TNC), where oxygen reduction occurs. In 2004, an MCO was isolated, with different architecture than conventional MCOs [12, 13]. This enzyme is a homotrimer with a molecular weight of only 38 kDa, and was named Small LACcase (SLAC) [14].

In figure 1A, the structure of wt SLAC is given, with a focus on the active site [12]. The TNC is situated at the interface between monomers, shown in the figure with different colors.Each monomer contains one T1Cu, and each functional homotrimer contains three active sites.

The reaction between MCOs and oxygen and has been extensively studied [15-20]. We refer to [20] for a comprehensive description of the reaction cycle.

Extensive analysis was performed by EPR spectroscopy on the T1 depleted form (T1D) of SLAC (T1D-SLAC) [20-24]. T1 depletion facilitates the spectroscopic study of the reaction between the TNC and oxygen because it removes the contribution of the strong T1Cu signals from the EPR and UV-Vis spectra. The T1D-SLAC is active in O_2 reduction, provided that reducing agents, such as ascorbic acid [21] or sodium dithionite [23], are added.

In figure 1B the catalytic cycle of T1D-SLAC, with a focus on the TNC, is summarized. As-synthesized, SLAC is in the resting oxidized state (RO). In the EPR spectrum only the T2Cu site is visible, as the T3Cu is EPR silent. In figure SI 1 and SI 5 the EPR spectra of the RO form are shown. Upon reduction, the copper atoms in the TNC are reduced, and all Cu-sites are EPR silent. This is known as the fully reduced state, FR. When the fully reduced protein is mixed with oxygen, the copper sites are reoxidized, and the tyrosine in position 108 is oxidized to form a tyrosyl radical. Here, we refer to this form as the reaction intermediate, RI. The RI

develops on a time scale of milliseconds, and fully decays to the RO state with a half-life of 20 minutes.

In 2009, the intermediate in the reaction between fully reduced T1D-SLAC and oxygen was identified as a copper-tyrosyl exchange-coupled biradical, forming a triplet state [21]. Later, aminoacid substitution studies confirmed the hypothesis of formation of the tyrosyl radical from the residue Y108, situated about 5 Å from the T2Cu [22]. Tyrosyl radicals appear in intermediate states of enzyme reactions for different systems, such as cytochrome oxidase and galactose oxidase [25-31].

Exchange-coupled metal ion-aminoacid radicals were identified in proteins, where they enhance the electron-transfer efficiency in reactions [32]. Studies on synthetic complexes provided insight into metal-radical exchange-coupled systems, showing how the relative orientation and the chemical environment of the involved orbitals can have significant impact on the nature of the coupling [28, 33-35]. For SLAC, the RI-state 9 GHz EPR spectrum revealed that it is a coupled Cu(II)-Tyr-radical system, be it that the magnitude of the exchange coupling could not be determined [24, 36]. Here, we use 275 GHz EPR, which in combination with 9 GHz EPR, enables to determine the exchange coupling. This study contributes to understanding the catalytic cycle of MCOs and the electronic properties of enzyme reaction intermediates, while demonstrating a method for studying short lived reaction intermediates of enzymes by high frequency EPR.

.

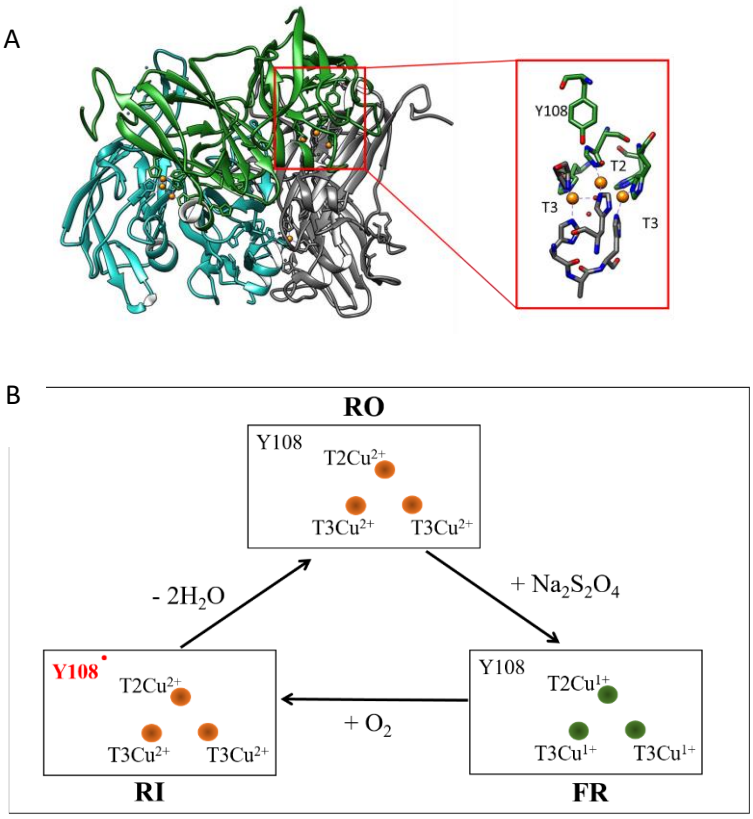

Figure 1. Structure of SLAC (PDB code: 3CG8) and of its oxygen reducing active site (A) and schematic of the reaction cycle at the TNC (B). In A), the three monomers forming the homo-trimer are colored in cyan, grey and green. The active site coppers are coordinated at the interface between monomers. In B), the oxidized copper ions (Cu(II)) are shown in orange, the reduced ones in green. RO : Resting oxidized state, FR: Fully reduced state, RI: Reaction intermediate state.

4.2 Materials and Methods

Protein Expression and Purification

Expression and purification of T1D SLAC was performed as previously described [14], with the only difference consisting in an additional size exclusion chromatography purification step after the anion exchange. The SEC was performed with a HiLoad 16/600, Superdex 200pg column in the same buffer used for elution from the anion exchange step: NaPi 100 mM, NaCl 100 mM, pH 6.8 (preparation buffer). Several batches of protein were prepared to

ensure reproducibility. Three individually prepared batches of protein were measured at 9 GHz and 275 GHz, and more samples of each batch were prepared for 9 GHz EPR measurement (for details, and to see spectra acquired for different batches, see SI).

Preparation for 9 GHz EPR samples

Sample preparation for 9 GHz EPR was performed in inert atmosphere inside a glove box at slight nitrogen overpressure at room temperature. The preparation buffer was exchanged by the nitrogen-saturated measurement buffer (NaPi 100 mM pH 6.8, 20% v/v glycerol) using 30 kDa cutoff amicon filters (Amicon Ultra Centrifugal Filter, 0.5 mL, 30 kDa cutoff, Millipore). The protein was incubated one hour in excess sodium dithionite ($Na_2S_2O_4$ sodium hydrosulphite, Sigma Aldricht) to reduce the copper sites. Desalting steps using 30 kDa amicon filters were done to remove the sodium dithionite from the sample. At this point, the concentrated sample was mixed with a 1:2 volume ratio of oxygen saturated measurement buffer (NaPi 100 mM pH 6.8, 65% v/v glycerol), quickly transferred into a 4 mm external diameter quartz tube and frozen in liquid nitrogen, with reaction times around 40 seconds. The final buffer composition is NaPi 100 mM, pH 6.8, 50% v/v glycerol. The sample was stored in liquid nitrogen until further use. Final protein concentration was in a range between 800 µM to 1 mM.

Preparation for 275 GHz EPR samples

The first step for 275 GHz EPR sample preparation is as described in the section "Preparation for 9 GHz EPR samples". After mixing the reduced T1D SLAC with oxygen saturated buffer, the sample was frozen in liquid nitrogen inside the same Eppendorf tube in which the mixing took place. Less than 30 seconds had passed when the protein and the oxygen saturated buffer were mixed and frozen. The sample was stored in liquid nitrogen until further use. Final sample concentration was in a range between 3 to 5 mM.

Sample transfer in the 275 GHz EPR tubes

Sample preparation is more complicated due to the small dimension of the capillary used at this frequency. To fill the 150 µm internal diameter tubes used for 275 GHz EPR measurements, the procedure described by Panarelli [23, 36] was adapted. The procedure was performed in a polystyrene box under constant flow of cold nitrogen gas, achieved with a N_2 temperature controller (variable temperature unit BVT3000, Bruker BioSpin GmbH), as described in Panarelli [23]. The temperature inside the box ranged between -40 and -15˚C, and was constantly monitored at different positions and heights by using three digital thermometers in combination with the N_2 temperature controller. A 50% v/v glycerol solution has a toothpaste-like viscosity in the temperature range between -30 and -20˚C, and

thereby can be manipulated. The EPR tube was attached to a syringe, and the sample was sucked into the tube by applying under-pressure with the syringe. Once full, the capillary was transferred onto a precooled lab-designed metal block and the sample loaded in the precooled (temperature 200 K) 275 GHz EPR insert with the same procedure as described in [37]. For measurement of the resting state of T1D SLAC, the sample could be manipulated at room temperature, and the sample is drawn in the EPR tube by capillary action.

Continuous wave 9 GHz EPR measurement

9 GHz EPR measurements were performed with an Elexsys E680 X-Band spectrometer from Bruker BioSpin GmbH, equipped with a He-Flow ESR900 cryostat from Oxford instruments. The 9 GHz spectrum was acquired at a temperature of 20 K, with the following parameters : modulation frequency 100 kHz, modulation amplitude 0.5 mT, time constant 327.68 ms, conversion time 81.92 ms, microwave power 20 µW, total measurement time: one hour.

Continuous wave 275 GHz EPR measurements

CW EPR measurements at 275 GHz were performed with a home-built spectrometer described in [38] equipped with a He-flow CF935 cryostat from Oxford instruments, and a laboratory-designed probe head with a single-mode cavity specifically designed for continuous wave measurements [39]. Measurements were performed at a temperature of 10 K, achieved with a continuous He flow. The measurement parameters for the resting-state spectrum are as follows : modulation frequency 1.7 kHz, modulation amplitude 2.4 mT, time constant 300 ms, microwave power: 0.51 µW. Parameters for RI state measurement: modulation frequency 1.7 KHz, modulation amplitude 4.7 mT, time constant 300 ms, microwave power 1.86 µW. The spectrum was acquired in the range between 8 and 11 T. Total measurement time: three to eight hours.

Simulation of EPR spectra

MATLAB (R2019a, The MathWorks, Inc., Natick, MA,USA) and the EasySpin package (5.2.35) were used for simulations of the EPR spectra. Spectra were simulated using the “pepper” function. The parameters used for simulations are listed in table 1. The error margins were generated by manually adjusting the simulation parameters until the simulation visibly differed from the experimental spectrum. The energy level diagrams were simulated with the “levelsplot” function in Easyspin. For a complete picture of the system, simulations were performed for different orientations of the external magnetic field relative to the Cu(II) g-tensor frame. The orientations used were: “x” (θ=90˚, ϕ=0 ˚), “y” (θ=90˚, ϕ=90 ˚), “z” (θ=0˚, ϕ=0˚), and “xyz” (θ=54.74˚, ϕ=45˚) with θ and ϕ as polar angles. In Easyspin the sign of J in $H_{exchange} = J\widehat{\boldsymbol{S}_1}\widehat{\boldsymbol{S}_2}$ is defined such that negative J values correspond to ferromagnetic

coupling (triplet ground state), and positive J values to anti-ferromagnetic coupling (singlet ground state).

4.3 Results

Figure 2 shows the 275 GHz CW-EPR spectrum of the RI state of T1D SLAC, for 9 GHz EPR spectra, see SI. The spectra were obtained by mixing the fully reduced sample with oxygen-saturated buffer (see Materials and methods). Unprocessed spectra, and details about processing, are given in the SI and fig. SI 7. The signal in fig. 2 is composed of two main lines, at 9.6 and 9.7 T. The linewidth of the signals (0.1 T) is such that eventual hyperfine and dipolar interactions remain unresolved. Additionally, broad featureless signals extend in the low field region, between 8.6 and 9.3 T, and could partly derive from background fluctuations, for details see SI. The spectrum is clearly not a superposition of a Cu(II) T2 spectrum and a tyrosyl radical spectrum, revealing that radical–pair interactions, such as exchange coupling J and dipolar interactions **D** play an important role.

To simulate the spectrum, magnetic resonance parameters from 9 GHz EPR, also obtained in this study, are taken into account, resulting in g-tensor (g_{Tyr} and g_{Cu}), hyperfine tensor and dipolar tensor parameters given in table 1.

The 275 GHz spectrum enables to determine the exchange interaction J. To that aim, a series of simulations is performed on the 275 GHz spectrum, see figure 3. Figure 3 shows that positive values of J above 10 GHz introduce intense lines in the high field region, between 10.2 and 10.7 T, see figure 3 A, marked as (2) in figure 3 A and B, that were not seen experimentally, ruling out those values, while values of J between +8 and -16 GHz were ruled out based on the 9 GHz simulations (in figure SI 9 and figure SI 11 the effects of values of J between +8 and -16 GHz on the 9 GHz EPR spectrum are illustrated, and discussed in SI text in “Strategy of simulation of EPR spectra”). As shown in figure 3, only J values between -18 and -19 GHz would provide a simulation that reproduces the experimental spectrum, while for magnitudes of J of -20 GHz or more negative values, there is clear disagreement with respect to the experimental spectrum, because the splitting between the two main signals is too large (compare figure 3 A and C). Therefore, J of the RI state is determined to be between -18 and -19 GHz.

Table 1. Spin Hamiltonian parameters used for the simulation of the SLAC intermediate spectra. The same parameters are used for both the 9 GHz and the 275 GHz simulation. α, β, γ Euler angles, define orientation of **D** relative to **g** and **A** tensor reference frame, using convention by Easyspin [40].

D_{xx} (MHz)	D_{yy} (MHz)	D_{zz} (MHz)	α (deg)	β (deg)	γ (deg)	J (MHz)
300 ± 15	300 ± 15	-600 ± 30	-90	-85	90	-19000 ± 1000

	g_x	g_y	g_z	A_x (MHz)	A_y (MHz)	A_z (MHz)
Copper	**2.042**	**2.052**	**2.26**	**30**	**40**	**626**
Tyrosyl	**2.009**	**2.0043**	**2.002**			

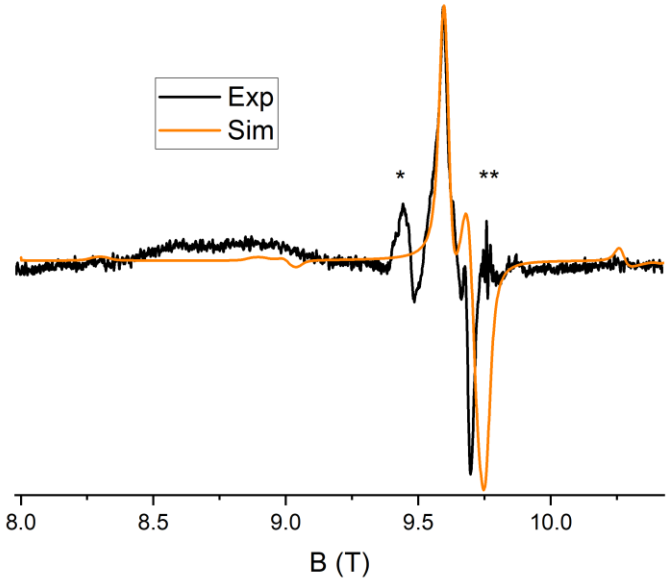

Figure 2. 275 GHz EPR spectrum of the intermediate of T1D SLAC. Black: experimental spectrum, orange: simulation. Experimental spectrum after subtraction of resting state spectrum obtained from the same protein batch. *Residual of resting state spectrum. Shape of resonance at 9.83 T is explained in detail in SI. For details about the subtraction, see fig. SI 7. ** Manganese impurity that overlaps with a radical signal, artifact remains after subtraction. For details about subtraction for the raw, unprocessed spectrum, see SI. Measurement temperature: 10K.

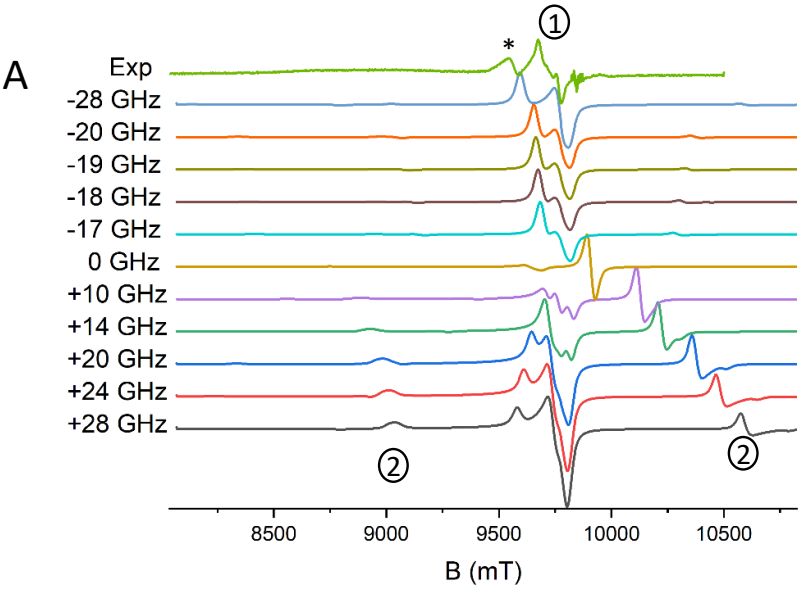
A
Exp
-28 GHz
-20 GHz
-19 GHz
-18 GHz
-17 GHz
0 GHz
+10 GHz
+14 GHz
+20 GHz
+24 GHz
+28 GHz
*
①
②
②
8500
9000
9500
10000
10500
B (mT)

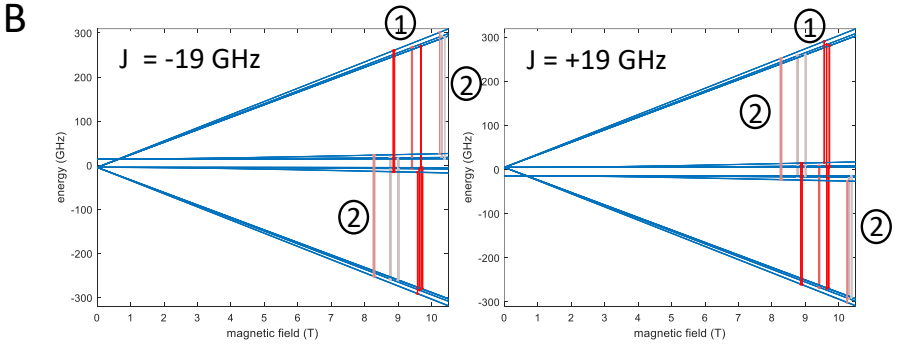
B
J = -19 GHz
J = +19 GHz
①
②
energy (GHz)
magnetic field (T)

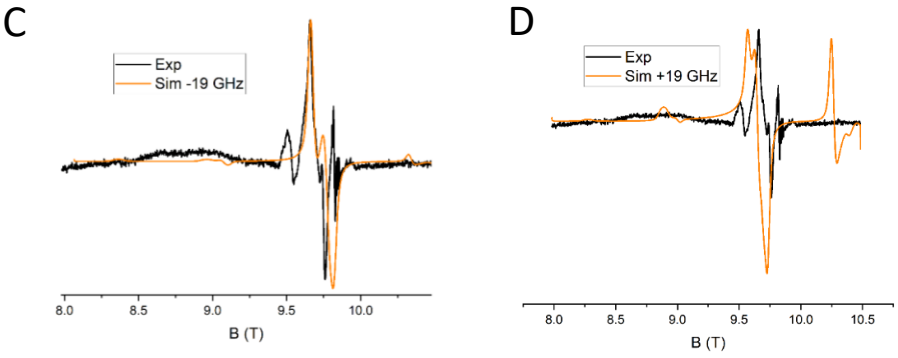
C
Exp
Sim -19 GHz
B (T)
D
Exp
Sim +19 GHz
B (T)

Figure 3. Effect of J on 275 GHz spectra of intermediate. A) Simulation of the 275 GHz spectrum for different values of J. Between 9.5 and 10 T the lineshape is sensitive to the value of J (lines marked 1) and additional transition, with smaller intensity, can occur between 8.5 and 10.5 T, depending on the value of J (lines marked as 2). For a positive value of J, between 10. 5 and 11 T, the transition (2) has much higher intensity for positive than for negative J. For negative values of J, the splitting of the main line increases with an increase of IJI. At J = -28 GHz, the simulation does not reproduce the experimental spectrum anymore. Values of J between 0 and -17 GHz are ruled out by the 9 GHz spectrum simulation, see fig. SI 9 and fig. SI 11. B) Energy levels plot for J = -19 GHz (left) and J = +19 GHz (right). Blue lines: energy levels, the color of the transition lines indicates their probability: red : high, light grey: low (partially allowed). C) and D) Experimental spectrum (black) after subtraction of the resting state is compared with simulation (orange) for C) J = -19 GHz and D) J = +19 GHz. Transition 2: intense lines for J = +19 GHz that are not observed. Those transition are less intense, and hidden in the linewidth, for J = -19 GHz. Asterisks: residual of resting state spectrum. The spectrum shown in C) and D) is shown after subtraction of the resting state contribution, but the manganese and the radical impurity are not subtracted, and evident, at 9.8 T.

4.4 Discussion

The intermediate state of T1D-SLAC (RI state) had been discovered using EPR and UV-Vis spectroscopy in 2009 [21]. The RI state is relatively short lived and is formed when the fully reduced protein is allowed to react with oxygen. This state decays with a half-life of about 20 minutes [21]. The 9 GHz EPR spectra were described as a biradical state, with one electron localized on the CuT2 site and the other on an amminoacid nearby, the Tyr 108 [21]. Here, we determine the EPR parameters of this short lived intermediate with very high field, 275 GHz EPR. The investigation is challenging because to obtain the RI, the reaction is performed in an inert-gas atmosphere, the reaction mixture has to be quickly frozen and kept at low temperature to keep the transformation back to the resting state (RO) of the enzyme at minimum. As RO formation cannot be completely avoided, RI spectra contain a varying fraction of RO state, which is subtracted from the raw spectra (see SI). Similar to previous studies we find variability of resting state (RO) spectra, the origin of which was discussed before and attributed to the presence of two components, which are present in different amounts in different protein batches [20]. In reference [20], the spectra were simulated by two components, showing different degrees of rhombicity and distinct copper g_z values for the two components.

From the combination of 9 and 275 GHz EPR spectra an exchange coupling J of -19 GHz is obtained (see results and SI “Detailed description of the strategy of simulation of 9 and 275 GHz EPR spectra”). With this value of J, now a consistent set of the remaining magnetic resonance parameters of the RI state can be determined. In the SI the steps taken are described in detail, see “Strategy of simulation of EPR spectra”. For a complete list of simulation parameters, see table 1.

The J-coupling observed here can be compared to J-values found for biradicals in biological protein systems and for covalently linked biradicals [25-30, 32-35]. The reported magnitudes of |J| range from 18 MHz [35] to 4800 GHz [34]. The largest J (4800 GHz) is found for a biradical with ten bonds between the radical centers. In enzymatic reactions in proteins, coupled biradicals often involve metal-ion-tyrosyl coupled biradicals [25-30, 33]. In other cases, thiyl- [32] and tryptophan [41] take the role of the tyr in the radical pair. In protein systems, measured |J| values range from 140 MHz [30] to 180 GHz [32]. In these systems the coupling can be ferromagnetic, like in the case of SLAC, or antiferromagnetic, like in the case of galactose oxidase [28, 33].
The J value of the RI in SLAC is in the high range for radical pairs in enzymes, which suggests a relatively strong overlap of the wavefunctions of the T2Cu and the Y108 in the RI state. This could stabilize the intermediate, so the RI could be a key part of the reduction of water to oxygen, and may confirm the role of Y108 in the stabilization of reactive oxygen species formed during the reaction.

The role of the RI state in the reaction of wt SLAC

Is the RI state relevant in the oxygen reduction reaction of wt-SLAC? In [22] the role of Y108 in the wt protein was studied extensively. Substituting Y108 with phenylalanine or alanine did not affect the second-order rate constant (k_{cat}/K_M), indicating that oxygen binding to the active site is unaffected. However, the turnover number (k_{cat}) decreased, suggesting impaired electron transfer to oxygen and a slower reaction than the wt-enzyme when Y108 is knocked out [22]. In the same work, substitution of Y108 led to the disappearance of the spectroscopic signature of the biradical, demonstrating that Y108 is providing the second electron in the RI state, both in the wt and T1D SLAC variants, thus confirming an active contribution of the RI to the reaction mechanism.
With the present study, the 275 GHz EPR spectrum of the RI state is reported. The exchange coupling provides insight into the electronic structure of the biradical and its realitively large value could indicate a role of Y108 in facilitating efficient electron transfer and stabilization of reactive intermediates in the catalytic mechanism of SLAC.

Supplementary Information

9 GHz EPR properties of the RO and the RI state

Figure SI 1 shows variability of RO spectra of different batches, the origin of which is attributed to the presence of different components, showing different rhombicity and different g_z values, present in different amounts in different batches [20]. The spectral part in the g = 4 region (figure SI 3) does not contain an RO contribution but suffers from cavity background.

The 9 GHz EPR spectrum of the RI state (Figure 2) consists of two signals: a more intense $\Delta m_s = 1$ transition (Figure SI 2, SI 4 and SI 12 B) and a weaker, partially allowed $\Delta m_s = 2$ transition (Figure SI 3 and SI 12 A). The $\Delta m_s = 1$ transition exhibits a complex multiline structure, arising from hyperfine and dipolar-coupling-derived splittings. The $\Delta m_s = 2$ transition, also known as the half-field transition, is split into four lines due to hyperfine coupling with the type 2-Cu(II) ion (T2Cu) in the active site, indicating a strongly coupled biradical or triplet (S = 1) state involving Tyr108 (Y108) [21, 22].

The as-measured RI spectrum (Figure SI 2) contains a residual contribution from the resting oxidized (RO) state, which is subtracted as described in Figure SI 4.

Preprocessing of 275 GHz RI spectra

Subtraction of the resting oxidized (RO) state:

It is known that the RI preparation contains some RO state, the amount of which depends on sample preparation details, i.e. mixing and freezing time, and can vary from sample to sample. Therefore, a certain amount of RO spectrum has to be subtracted from the raw RI spectrum. Since the resting state EPR spectrum of different T1D SLAC preparation batches can have different shapes [20], care is taken that for the subtraction, the 275 GHz RO spectrum is from the same batch as the RI preparation batch. There is evidence that the peak at 9.5 T in the RI spectrum (figure SI5) originates from the RO state: the resting-state spectrum has a pronounced peak at 9.5 T, see figure SI 5. Another indication is that in the RI spectra, the relative intensity of the peak at 9.5 T and with respect to the peak at 9.7 T varies for different RI spectra, see fig. SI 6, as expected if the signal at 9.5 T derives from the resting state. Also, the simulations performed, see fig. 3 main text, show that none of the simulations yield spectra with a signal at 9.5 T. Therefore, the amount of resting-state spectrum subtracted from the RI spectra is guided mostly by the amplitude of the 9.5 T peak and considering the overall lineshape, resulting in the spectra shown in figure SI 7. Figure SI 7A shows that the feature at 9.5 T does not exactly overlap in the RI the RO state spectrum. This explains the residual feature at 9.5 T in the processed RI spectrum (figure SI 7C). Also, the

overlap of the RO spectrum and the unprocessed RI spectrum makes the lineshape of the RI spectrum at 9.83 T less reliable than the feature at 9.7 T.
Subtraction of two experimental spectra can add additional line distortions and artifacts to the spectrum. Yet in the present case such artifacts are not obvious and, therefore, no additional baseline correction is performed. To improve the lineshape in the higher field region, a narrow-line radical contribution and the residual six-line pattern of a Mn(II)-impurity are subtracted.

Detailed description of the strategy of simulation of 9 and 275 GHz EPR spectra

As described in [21], the $\Delta m_s=2$ transition of the 9 GHz EPR spectrum is characteristic of a strongly coupled biradical or triplet state. The splitting of this signal into four lines signifies that one of the two unpaired electrons resides on the T2Cu. The second electron was assigned to a tyrosyl radical (Y108)[21]. Thus, the spectra at 9 and 275 GHz were simulated based on two coupled unpaired electrons, one on the T2Cu, and the second on the tyrosyl Y108 radical.
For the interpretation of the spectra, the effect of the magnetic parameters, A_z, **D** and J on the spectra measured at different frequencies need to be considered. For example, while the copper hyperfine and the dipolar interactions are resolved in the 9 GHz spectra, they are masked by the linewidth at 275 GHz. The g-tensor parameters of the Cu(II) T2 are obtained from a combination of 9 and 275 GHz EPR, using characteristic values of T2Cu copper centers [24] and the ones obtained from simulation of RO spectra as starting points. The g-tensor parameters of the tyrosyl radical in the 275 GHz EPR are masked by the effects of the exchange interaction J in the RI state and therefore cannot be extracted from the 275 GHz spectrum of T1D SLAC RI. Therefore, literature values are used [42], and the relative orientation of the g-tensor and the D-tensor cannot be determined.
In the g=2 region, the shape of the 9 GHz EPR spectrum is complicated by overlapping lines arising from a combination of hyperfine and dipolar interactions that have a similar magnitude, see table 1, main text.
However, since the CuT2 hyperfine interaction **A** along the z direction, A_{zCu}, causes the splitting of the $\Delta m_s=2$ transition (g=4) into four lines (see above), it can be measured with high precision. A_x and A_y components of the Cu-hyperfine tensor, with their smaller magnitude, have minimal influence on the overall spectral shape.
The dipolar tensor **D** is estimated from the distance between Y108 and the T2Cu, from the crystal structure of the protein (PDB code: 3CG8), as described in [24], and here is manually adjusted to best fit the simulation to the experimental spectrum.
To evaluate the magnitude of J, various simulation options were explored. Figures SI 8-11 illustrate the effects of different values of J on the 9 GHz spectrum: for values of J between

-16 and 10 GHz, extra lines between 0 and 280 mT occur, fig. SI 9, which do not match the experimental data (see Fig. SI 9 and 10). These additional lines are labelled as transition (3) in figure SI 11. At values of IJI higher than 10 GHz, the g=2 region of the 9 GHz EPR spectrum does not change much, figure SI 8. In the low field region, see figure SI 9, negative values of J between -10 and -16 GHz result in spectra with transitions with an intensity comparable to the half-field $\Delta m_s=2$ signal, which were not observed experimentally, see figure SI 11 for experimental spectra. Thus, values of J comprised between +10 and -16 GHz are excluded. These results enter in the analysis of the 275 GHz spectrum, as described in the main text, from which J = -19 GHz results.

Supplementary Figures

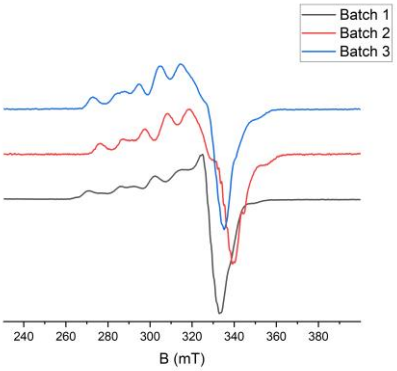

Figure SI 1. Resting state 9 GHz EPR spectra obtained from the different batches of T1D SLAC. Differences in spectra were observed before and attributed to the existence of different components in different ratios, see main text. Measurement temperature: 40K.

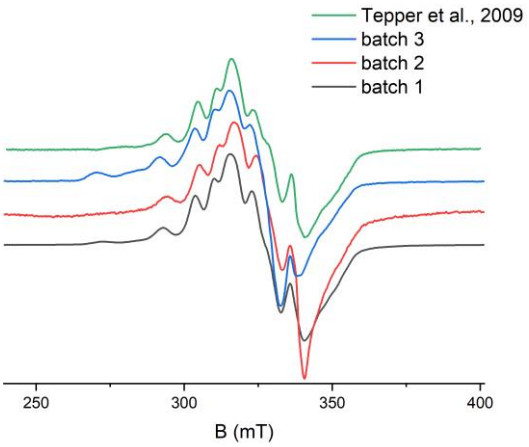

Figure SI 2. 9 GHz EPR RI state spectra as measured, obtained from the different batches of T1D SLAC in the g=2 region. The green spectrum was obtained and published by our group in 2009, and was obtained as described in [21]. Measurement temperature batch 1 to 3: 20K. Tepper et al., 2009 : 40K.

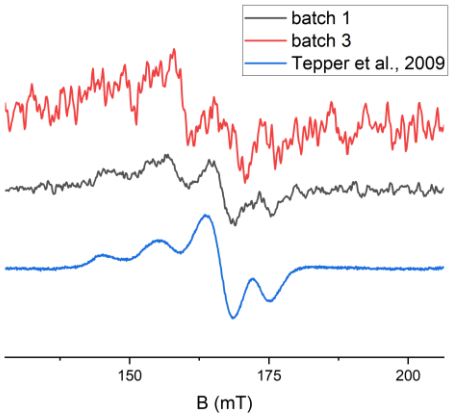

Figure SI 3. Intermediate state 9 GHz EPR spectra obtained from the different batches of T1D SLAC in the $\Delta m_s=2$ region. From batch 1 and 3 no cavity background was subtracted. For simulation the spectrum from Tepper et al., was used for its more reliable lineshape. The $\Delta m_s=2$ spectrum shown in the main text and used for simulation (blue) was published by our group in 2009, and was obtained as described in Tepper et al. [21]. The spectrum from batch 2 (not shown) was obtained on a different spectrometer, and background fluctuations do not allow to interpret this part of the spectrum of batch 2. Measurement temperature batch 1 to 3: 20K. Tepper et al., 2009: 40K.

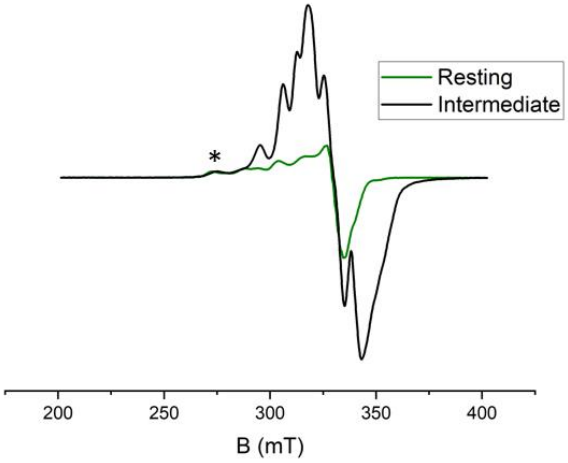

Figure SI 4. Contribution of the 9 GHz RO EPR spectrum on the RI state EPR spectrum of the same batch of SLAC. The spectra were normalized to the low field line of the A_{zz} feature of the Cu-hyperfine interaction of the resting state spectrum, marked by the asterisk. The RI state spectrum shown in the main text figure 2 results from the subtraction of the resting state spectrum (green) from the intermediate state spectrum (black), after the normalization shown in the figure.

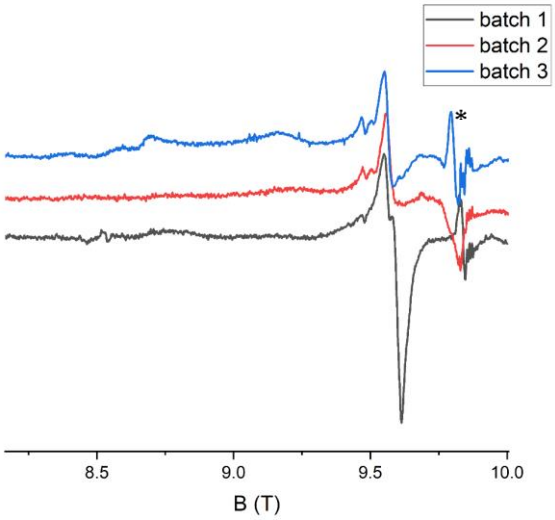

Figure SI 5. Resting state 275 GHz EPR spectra obtained from different batches of T1D SLAC. The spectra show an intense peak in the g_{xy} region (9.6 T). Lines in the g_z region between 8.5 and 9.3 T are broadened and mixed with background fluctuations. In all spectra a six-line manganese (Mn(II)) impurity is present, which overlaps with a signal from another radical contamination, marked by an asterisk. Measurement temperature: 10K.

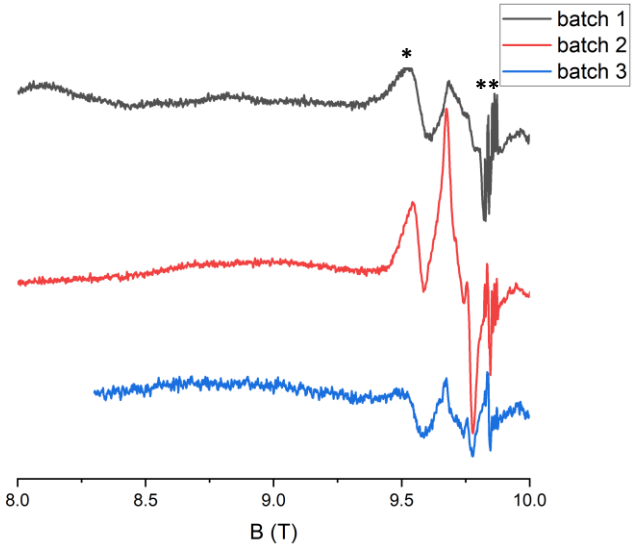

Figure SI 6. Intermediate state 275 GHz EPR spectra from the different batches of T1D SLAC. Shown are raw spectra without background correction and without resting-state subtraction. Marked by *: resting state feature. Marked by **: a six-line Mn(II) impurity, overlapping with a narrow single line radical impurity. The signal at 9.88 T is the least perturbed part the RI spectrum. Spectrum after resting-state subtraction: see figure 3 main text. Protein concentration: 3 to 5 mM. See figure SI 14 for processing steps. Measurement temperature: 10K.

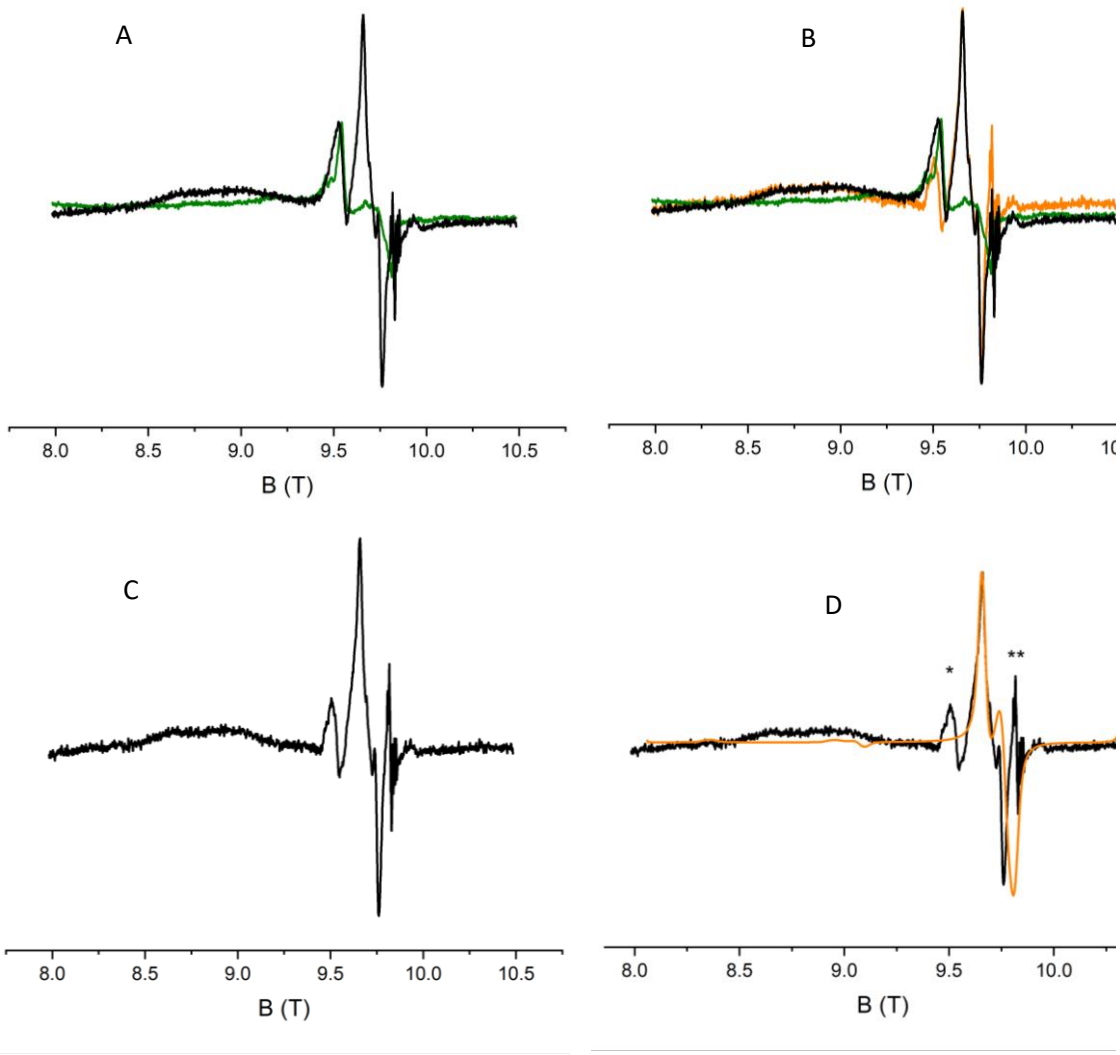

Figure SI 7 Processing of the 275 GHz EPR intermediate spectrum. A) RO spectrum (green), unprocessed RI spectrum (black). B) RO spectrum (orange), RI spectrum (green), result of subtraction (Black). C) Pure intermediate spectrum, resulting from subtraction. D) Pure RI spectrum (black) and simulation (orange). The RI and RO spectra shown are from the same batch. Spectra are normalized to the intensity of the line at B = 9.5 T of the RO state spectrum, and the manganese-impurity signal is used for field calibration of different measurements. * correspond to the residual RO spectrum in the RI spectrum. ** corresponds to the radical and manganese impurities. Artefacts after subtraction are visible in the pure RI spectrum, e.g. narrowing of the higher field line in correspondence to **.

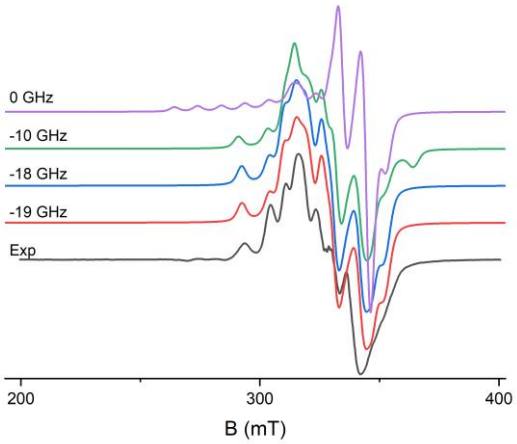

Figure SI 8. Simulated 9 GHz EPR spectra for different exchange interaction (J) values. Spectral shape in the g=2 region. For other simulation parameters see table 1 in the main text.

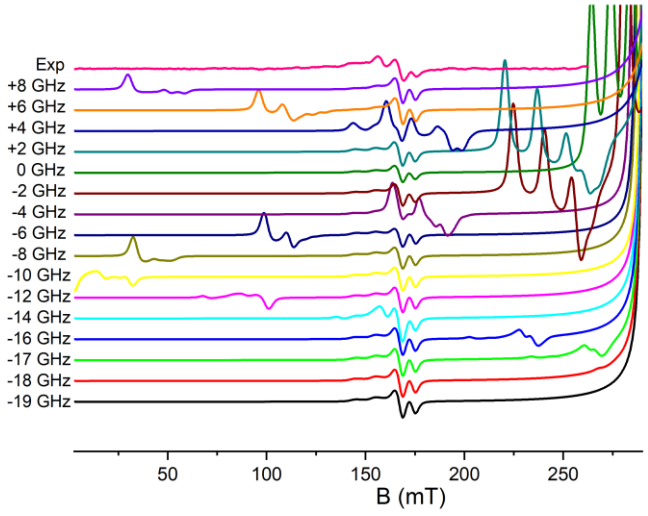

Figure SI 9. Simulated 9 GHz EPR spectra for different exchange interaction (J) values for the low field region of the spectra. Values of J comprised between +8 GHz and -17 GHz imply the presence of additional lines that are not observed experimentally, and are thereby ruled out. For others simulation parameters see table 1 in the main text.

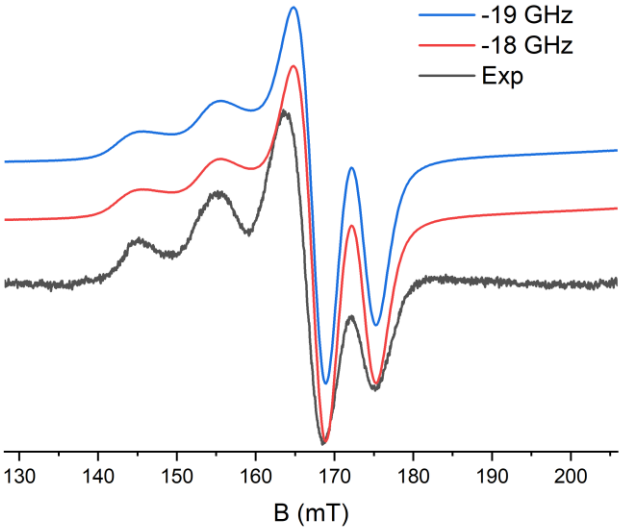

Figure SI 10. Experimental and simulated 9 GHz EPR spectra in the g = 4 region for J = -18 GHz and J = -19 GHz. Experimental spectrum: details, see main text.

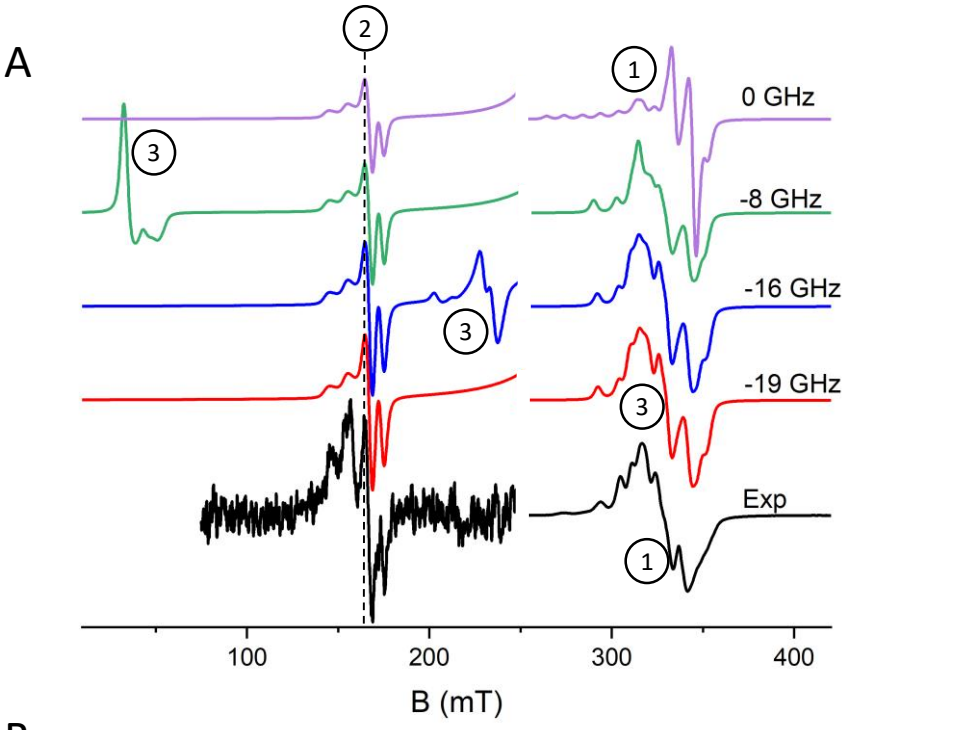
A
2
1
0 GHz
3
-8 GHz
-16 GHz
3
-19 GHz
3
Exp
1
100
200
300
400
B (mT)

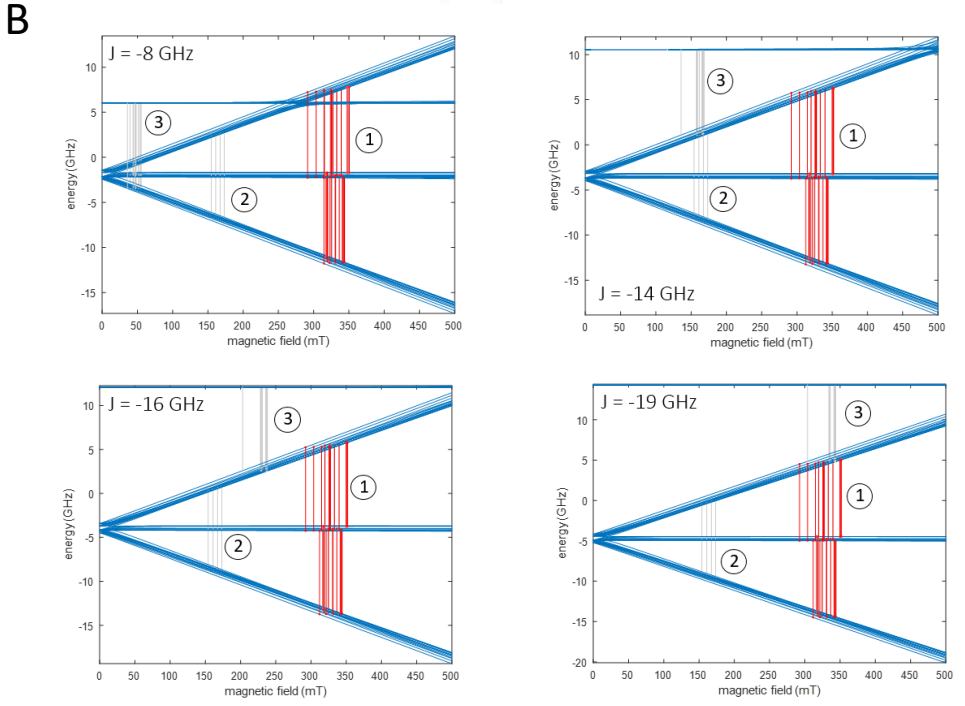
B
J = -8 GHz
J = -14 GHz
J = -16 GHz
J = -19 GHz
energy (GHz)
magnetic field (mT)

Figure SI 11. Effect of J on 9 GHz EPR spectra of the RI state. A) Experimental and simulated 9 GHz EPR spectra for different J coupling values, and B) corresponding energy levels. The amplitude of the low field (0 – 250 mT), $\Delta m_s = 2$ transition, region has been magnified by a factor of 300 for the simulation, and by a factor of 100 for the experimental spectrum. The transitions are numbered in the spectra and in the energy-levels plots : (1) transition giving the g=2 spectrum. (2) $\Delta m_s = 2$ transition, giving the g=4 spectrum. (3) Additional transitions that occur depending on the magnitude of $|J|$. Transition (3) overlaps with transition (2) for J = -14 GHz, and overlaps with transition (1) at J = -19 GHz. Simulation shows that lines marked (3) would appear in the spectrum for J = -8 GHz and J = -16 GHz. Such lines are not observed experimentally, and therefore, those values of J are ruled out (see also fig. SI 11). Blue lines: energy levels, color of the vertical transition lines shows transition probability: red : high, light grey: low (partially allowed).

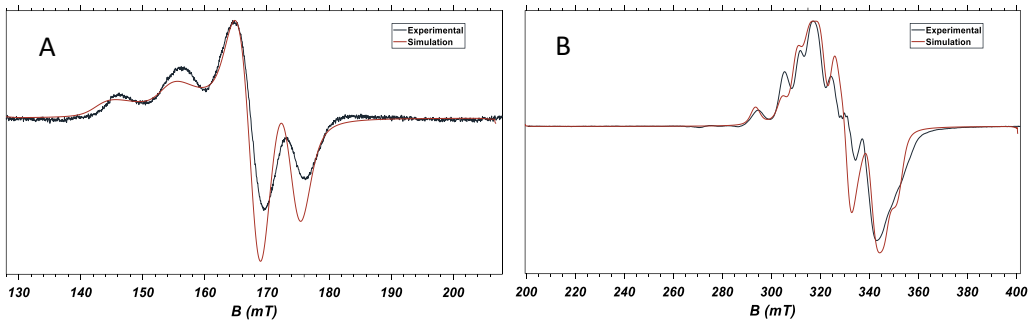

Figure SI 12. 9 GHz EPR spectrum of the reaction intermediate of T1D SLAC. A) Zoom in on the g=4 region, showing the $\Delta m_s = 2$ transition. Black : experimental spectrum, orange: simulation. A) was obtained in our lab and published in Tepper et al., 2009. B). Spectrum in the g=2 region. Black: experimental spectrum, orange: simulation. Simulation parameters: see table 1, main text. Experimental spectrum B) is presented after subtraction of the resting state spectrum obtained from the same protein batch. For details about the processing, see fig. SI 4. Measurement temperature: 20K. Tepper et al., 2009 : 40K.

References

[1] G. Vashchenko, R.T. MacGillivray, Multi-copper oxidases and human iron metabolism, Nutrients 5(7) (2013) 2289-313.
[2] K. Kaur, A. Sharma, N. Capalash, P. Sharma, Multicopper oxidases: Biocatalysts in microbial pathogenesis and stress management, Microbiol Res 222 (2019) 1-13.
[3] E.I. Solomon, A.J. Augustine, J. Yoon, O2Reduction to H2O by the multicopper oxidases, Dalton Transactions (30) (2008) 3921-3932.
[4] K. Obleser, H. Kalaus, B. Seidl, M. Kozich, C. Stanetty, M.D. Mihovilovic, An Organic Chemist's Guide to Mediated Laccase Oxidation, ChemBioChem 23(23) (2022) e202200411.
[5] T. Brugnari, D.M. Braga, C.S.A. dos Santos, B.H.C. Torres, T.A. Modkovski, C.W.I. Haminiuk, G.M. Maciel, Laccases as green and versatile biocatalysts: from lab to enzyme market—an overview, Bioresources and Bioprocessing 8(1) (2021).
[6] I. Bassanini, E.E. Ferrandi, S. Riva, D. Monti, Biocatalysis with Laccases: An Updated Overview, Catalysts, 2021.
[7] G. Janusz, A. Pawlik, U. Świderska-Burek, J. Polak, J. Sulej, A. Jarosz-Wilkołazka, A. Paszczyński, Laccase Properties, Physiological Functions, and Evolution, International Journal of Molecular Sciences, 2020.
[8] M. Sherif, D. Waung, B. Korbeci, V. Mavisakalyan, R. Flick, G. Brown, M. Abou-Zaid, A.F. Yakunin, E.R. Master, Biochemical studies of the multicopper oxidase (small laccase) from treptomyces coelicolor using bioactive phytochemicals and site-directed mutagenesis, Microbial Biotechnology 6(5) (2013) 588-597.
[9] M.u. Rahman, M.W. Ullah, J.A. Shah, S. Sethupathy, H. Bilal, S.A. Abdikakharovich, A.U. Khan, K.A. Khan, N. Elboughdiri, D. Zhu, Harnessing the power of bacterial laccases for xenobiotic degradation in water: A 10-year overview, Science of The Total Environment 918 (2024) 170498.
[10] S.M. Jones, E.I. Solomon, Electron transfer and reaction mechanism of laccases, Cell Mol Life Sci 72(5) (2015) 869-83.
[11] B.G. Malmström, B. Reinhammar, T. Vänngård, Two forms of copper (II) in fungal laccase, Biochimica et Biophysica Acta (BBA) - General Subjects 156(1) (1968) 67-76.
[12] T. Skálová, J. Dohnálek, L.H. Østergaard, P.R. Østergaard, P. Kolenko, J. Dušková, A. Štěpánková, J. Hašek, The Structure of the Small Laccase from Streptomyces coelicolor Reveals a Link between Laccases and Nitrite Reductases, Journal of Molecular Biology 385(4) (2009) 1165-1178.
[13] H. Komori, Y. Higuchi, Structural insights into the O2 reduction mechanism of multicopper oxidase, The Journal of Biochemistry 158(4) (2015) 293-298.

[14] M.C. Machczynski, E. Vijgenboom, B. Samyn, G.W. Canters, Characterization of SLAC: a small laccase from Streptomyces coelicolor with unprecedented activity, Protein Sci 13(9) (2004) 2388-97.
[15] A.E. Palmer, S.K. Lee, E.I. Solomon, Decay of the Peroxide Intermediate in Laccase: Reductive Cleavage of the O−O Bond, Journal of the American Chemical Society 123(27) (2001) 6591-6599.
[16] S. Wherland, O. Farver, I. Pecht, Multicopper oxidases: intramolecular electron transfer and O2 reduction, J Biol Inorg Chem 19(4-5) (2014) 541-54.
[17] J. Yoon, B.D. Liboiron, R. Sarangi, K.O. Hodgson, B. Hedman, E.I. Solomon, The two oxidized forms of the trinuclear Cu cluster in the multicopper oxidases and mechanism for the decay of the native intermediate, Proceedings of the National Academy of Sciences of the United States of America 104(34) (2007) 13609-13614.
[18] J. Yoon, E.I. Solomon, Electronic Structure of the Peroxy Intermediate and Its Correlation to the Native Intermediate in the Multicopper Oxidases: Insights into the Reductive Cleavage of the O−O Bond, Journal of the American Chemical Society 129(43) (2007) 13127-13136.
[19] S.-K. Lee, S.D. George, W.E. Antholine, B. Hedman, K.O. Hodgson, E.I. Solomon, Nature of the Intermediate Formed in the Reduction of O2 to H2O at the Trinuclear Copper Cluster Active Site in Native Laccase, Journal of the American Chemical Society 124(21) (2002) 6180-6193.
[20] R. Dasgupta, K. Gupta, F. Nami, H.J.M. de Groot, G.W. Canters, E.J.J. Groenen, M. Ubbink, Chemical Exchange at the Trinuclear Copper Center of Small Laccase from Streptomyces coelicolor, Biophys J 119(1) (2020) 9-14.
[21] S.M. Armand W.J.W. Tepper, Silvia Sottini, Erik Vijgenboom,, a.G.W.C. Edgar J.J. Groenen, Identification of a Radical Intermediate in the Enzymatic Reduction of Oxygen by a Small Laccase, J. Am. Chem. Soc. 131 (2009) 11680-11682.
[22] A. Gupta, I. Nederlof, S. Sottini, A.W. Tepper, E.J. Groenen, E.A. Thomassen, G.W. Canters, Involvement of Tyr108 in the enzyme mechanism of the small laccase from Streptomyces coelicolor, J Am Chem Soc 134(44) (2012) 18213-6.
[23] E.G. Panarelli, T-Cycle EPR development at 275 GHz for the study of reaction kinetics and intermediates, Doctoral dissertation, Leiden University (2018).
[24] F. Nami, Enzymatic reduction of oxygen by small laccase, a rapid freeze-quench EPR study, Doctoral dissertation, Leiden University (2017).
[25] O. Hansson, B. Karlsson, R. Aasa, T. Vänngård, B.G. Malmström, The structure of the paramagnetic oxygen intermediate in the cytochrome c oxidase reaction, The EMBO Journal 1(11) (1982) 1295-1297-1297.
[26] J.E. Morgan, M.I. Verkhovsky, G. Palmer, M. Wikström, Role of the PR Intermediate in the Reaction of Cytochrome c Oxidase with O2, Biochemistry 40(23) (2001) 6882-6892.

[27] M. Wikstrom, R.B. Gennis, P.R. Rich, Structures of the intermediates in the catalytic cycle of mitochondrial cytochrome c oxidase, Biochim Biophys Acta Bioenerg 1864(2) (2023) 148933.
[28] T.W. Jochen Müller, Eckhard Bill,, L.O.-M. Peter Hildebrandt, a.K.W. Thorsten Glaser, Why Does the Active Form of Galactose Oxidase Possess a Diamagnetic Ground State, Angew. Chem. Int. Ed. 37 (1998) 616-619.
[29] J. Stubbe, P. Riggs-Gelasco, Harnessing free radicals: formation and function of the tyrosyl radical in ribonucleotide reductase, Trends in Biochemical Sciences 23(11) (1998) 438-443.
[30] D.J. Hirsh, W.F. Beck, J.B. Lynch, L. Que, Jr., G.W. Brudvig, Using saturation-recovery EPR to measure exchange couplings in proteins: application to ribonucleotide reductase, Journal of the American Chemical Society 114(19) (1992) 7475-7481.
[31] V.A. Szalai, H. Kühne, K.V. Lakshmi, G.W. Brudvig, Characterization of the Interaction between Manganese and Tyrosine Z in Acetate-Inhibited Photosystem II, Biochemistry 37(39) (1998) 13594-13603.
[32] J. Manzerova, V. Krymov, G.J. Gerfen, Investigating the intermediates in the reaction of ribonucleoside triphosphate reductase from Lactobacillus leichmannii: An application of HF EPR–RFQ technology, Journal of Magnetic Resonance 213(1) (2011) 32-45.
[33] H.L. Achim Sokolowski, R.S. Thomas Weyhermüller, E.B. Eberhard Bothe, Peter Hildebrandt,, K. Wieghardt, Phenoxyl-copper(II) complexes: models for the active site of galactose oxidase, JBIC 2 (1997) 444-453.
[34] P.F. Richardson, R.W. Kreilick, Transition metal complexes with radical ligands: pyridyliminonitroxide radicals with copper and vanadium, Journal of Magnetic Resonance (1969) 29(2) (1978) 285-291.
[35] S.S. Eaton, K.M. More, B.M. Sawant, P.M. Boymel, G.R. Eaton, Metal-nitroxyl interactions. 29. EPR studies of spin-labeled copper complexes in frozen solution, Journal of Magnetic Resonance (1969) 52(3) (1983) 435-449.
[36] E.G. Panarelli, P. Gast, E.J.J. Groenen, Temperature-cycle electron paramagnetic resonance, Physical Chemistry Chemical Physics 22(17) (2020) 9487-9493.
[37] E.G. Panarelli, H. van der Meer, P. Gast, E.J.J. Groenen, Effective coupling of rapid freeze-quench to high-frequency electron paramagnetic resonance, Plos One 15(5) (2020).
[38] H. Blok, J.A.J.M. Disselhorst, S.B. Orlinskii, J. Schmidt, A continuous-wave and pulsed electron spin resonance spectrometer operating at 275GHz, Journal of Magnetic Resonance 166(1) (2004) 92-99.
[39] G. Mathies, H. Blok, J.A.J.M. Disselhorst, P. Gast, H. van der Meer, D.M. Miedema, R.M. Almeida, J.J.G. Moura, W.R. Hagen, E.J.J. Groenen, Continuous-wave EPR at 275GHz:

Application to high-spin Fe3+ systems, Journal of Magnetic Resonance 210(1) (2011) 126-132.
[40] S. Stoll, A. Schweiger, EasySpin, a comprehensive software package for spectral simulation and analysis in EPR, J Magn Reson 178(1) (2006) 42-55.
[41] G. Bleifuss, M. Kolberg, S. Pötsch, W. Hofbauer, R. Bittl, W. Lubitz, A. Gräslund, G. Lassmann, F. Lendzian, Tryptophan and Tyrosine Radicals in Ribonucleotide Reductase: A Comparative High-Field EPR Study at 94 GHz, Biochemistry 40(50) (2001) 15362-15368.
[42] G. Jeschke, EPR techniques for studying radical enzymes, Biochimica et Biophysica Acta (BBA) - Bioenergetics 1707(1) (2005) 91-102.

Chapter 5.
Pulsed Electron Paramagnetic Resonance on Cu(II)-Cage Compounds With Respectively Six or Eight Copper Ions

A publication of the work described in this chapter is in preparation: L. Passerini, E.O. Bobylev, F.J. de Zwart, H. Hintz, A. Godt, B. de Bruin, J.N.H. Reek and M. Huber ”Pulsed electron paramagnetic resonance on Cu(II) cage compounds with six, respectively eigth copper ions”, to be submitted.

5.1 Introduction

Complexes in which more than two units interact at nano-meter distances to generate function are important in many areas from biology to chemistry. Examples are multimeric protein (sub-) units in biochemistry [1-4] or multiple (transition) metal-ion centers in molecular catalysts [1, 5, 6]. For the latter, there has recently been a surge of interest in radical-based supramolecular systems, owing to their diverse properties and promising applications [8]. The presence of multiple spins within a confined spatial arrangement and a defined geometric structure in such systems gives rise to adjustable spin-spin interactions [10-12]. Moreover, encapsulation of paramagnetic guest molecules creates promising candidates for sensor materials [8, 10-12]. The integration of radicals and metal ions into supramolecular architectures also gives them redox properties for potential catalytic applications [6-8]. In the past, the analysis of radical-based supramolecular systems predominantly relied on continuous wave electron paramagnetic resonance (EPR) techniques [10-12]. Pulsed EPR adds the possibility of obtaining structural information, and in particular, pulsed dipolar EPR spectroscopy that provides nano-meter distance constraints is promising. Methods, such as double electron-electron resonance (DEER or PELDOR) have proven their value in many areas of chemistry and biology [13-17]. While the theory and practice of the investigation of two-spin systems, i.e. the interaction between pairs of spins, is established, as reviewed in [18, 19], cases where more than two spins interact within a nano-object still present challenges.

If more than two spins interact in the DEER sensitive distance range, the modulation depth becomes larger than in two-spin systems. For a two-spin system, the modulation depth is given by the inversion efficiency λ, whereas for multispin systems the modulation depth Δ is given by equation:

$$\Delta_N = 1 - (1 - \lambda)^{N-1} \qquad (1)$$

where N is the number of interacting spins [20]. This increase in modulation depth was used as a method for counting monomers in nanoobjects, first by Tsvetkov et al. [21, 22], in oligomers of biological systems [20, 23-25]. Additionally, ghost peaks in the distance distributions can occur. These peaks do not represent actual distances, but derive from sum- and difference-frequencies of the dipolar frequencies measured by DEER [26]. Such ghost peaks can obscure the pair-wise distances and thereby interfere with using DEER distances for structural information. Approaches proposed to identify and suppress ghost peaks are proposed in literature [26-29]. Among those, adjustment of inversion efficiency is the most common method that can be used during data acquisition, by reducing the power of the pump-pulse. Also, see von Hagens et al. [26], power scaling in processing the data is possible. This method is commonly known as “ghost suppression”, as it suppresses the ghost distances [26]. On systems containing up to eight nitroxides Valera et al. [28] showed

that while power scaling or reduction of the inversion efficiency alone are not enough, a combination of the two still allows for reliable extraction of spin-pair distances, even though the expected relative intensities of the distance peaks were not recovered [28]. Considering metal ions, there is only one study, by Edwards et al. [30], where DEER experiments were performed on a labelled proteorhodopsin hexamer, comparing nitroxide and Gd(III) based spin labels. Multispin effects in the Gd(III) labelled samples were strongly reduced with respect to nitroxides, an effect that was attributed to the naturally low inversion efficiency for Gd(III) [30].

Here we investigate multi-spin interactions in the copper(II) cages Pd12Cu6 ($Pd_{12}Cu_6L^{DMAP}_{24}$)(**Cu6**) and Pd12Cu8 ($Pd_{12}Cu_8L^{Pro}_{24}$) (**Cu8**) (fig.1), with respectively six and eight copper(II) ions. The synthesis, structural characterization and catalytic interest in these systems were described in [7]. The regular geometric structure of the copper cages and the presence of a relatively large number of Cu(II) ions in a defined arrangement make them particularly attractive, in particular, since multispin effects systems with large magnetic anisotropy are limited so far (see above) [26, 27]. Therefore, the copper cages **Cu6** and **Cu8** present an ideal system to test multi-spin effects in Cu(II) systems. It has to be noted that the Cu(II)-derivatives of the cage molecules investigated here are not as stable as the term "model compounds" may imply. Prolonged handling at room temperature causes decay, and the Cu(II) centers have a tendency to reduce to Cu(I) making them EPR inactive [7].

In the present study, the application of 9 GHz DEER on the multi-copper cages shown in figure 1 is described, revealing multispin interactions, i.e. the interaction of more than two spins. The distances confirm that for **Cu6** the structure shown in figure 1B applies. For **Cu8,** the model shown in fig.1A is consistent with the DEER data.

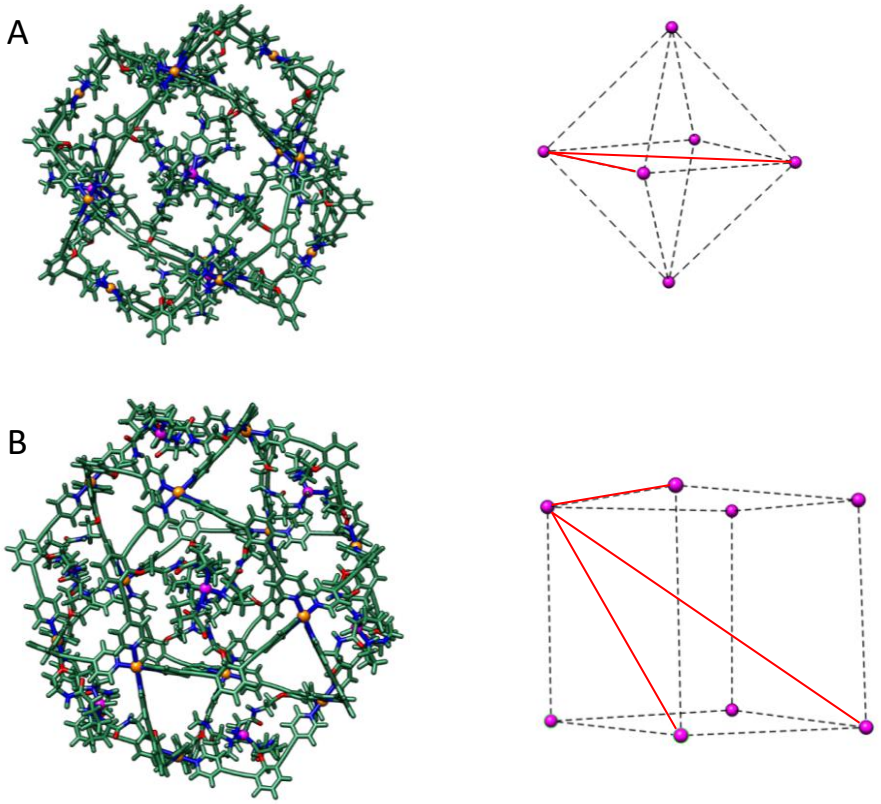

Figure 1. Structures of the Cu(II) cages studied in this work (left), and sketch of the spatial arrangement of the coordinated copper ions (right). A) **Cu6**. The copper ions are located in the six square windows of the nanosphere, forming an octahedron, giving a total of 2 different distances, highlighted in red. B) **Cu8**. The copper ions are located in the triangular windows of the nanosphere, forming a cube, giving a total of three different distances. Magenta spheres: copper ions, yellow spheres: palladium ions, green: functional groups coordinating the copper ion, red lines: highlight of the different copper distances inside the cages. For details, see [7].

5.2 Materials and Methods

EPR spectroscopy

Pulsed EPR measurements were performed at 9 GHz on an Elexsys E680 spectrometer (Bruker) using a 3 mm ER 4118 X-MD-3-W1 split-ring resonator. The cryogenic temperature of 20K was obtained with helium gas in a CF935 (Oxford Instruments) cryostat with an ITC502 temperature controller (Oxford Instruments). Samples were prepared in 3 mm outer-diameter quartz tubes, frozen and stored in liquid nitrogen before insertion into the precooled helium gas-flow cryostat.

The four-pulse DEER [4, 5] sequence $(\pi/2)_1$-τ_1- $(\pi)_1$–$(\tau_1 + t)$-$(\pi)_2$–$(\tau_2$-$t)$-$(\pi)_1$–τ_2-[echo] was employed, where subscripts 1 and 2 indicate events occurring at the observer and pump frequency, respectively. The pump and observer frequencies were separated by 75 MHz. The power of the pump pulse was adjusted to invert the echo maximally. The lengths of the pulses at the observer frequency were 16 and 32 ns for the π /2 and π pulses, respectively. The length of the pump pulse was 16 ns. In the measurements, the τ time was incremented with 8 ns steps starting at τ = 140 ns to suppress nuclear modulation. The slices were added to obtain hyperfine-modulation-free time traces and phase corrected. Regular traces were measured with a total evolution time of 2152 ns. For modulation- depth comparison, a separate experiment with shorter evolution time and a back-to-back measurement of **Cu6**, **Cu8** and **Cu2** was performed.

The DEER data were analyzed using the DeerAnalysis2019 and DeerAnalysis2023 programs [31], which are available from http://www.epr.ethz.ch/ software/index. DeerAnalysis2019 version was used for Tikhonov regularization and gaussian fitting, while DeerAnalysis2023 ws used for DEERNet analysis. Contribution of a known instrumentation artifact at 1940 ns could not be completely eliminated from the real part, therefore all traces were truncated to 1932 ns. Zero time of the traces was 88 ns. After background correction of the data using a three-dimensional background, the distance distribution was determined by Tikhonov regularization, with a regularization parameter of 125. Validation was performed using the validation tool in DeerAnalysis. For **Cu6** the white-noise contribution was varied between 0.02 and 1.5 with 10 steps, and the background start from 372 ns to 1000 ns with 20 steps. For **Cu8** the white-noise contribution was varied between 0.03 and 1.5 with 10 steps, and the background start from 372 ns to 1000 ns with 20 steps. The shaded areas in the distance distribution plots show, for a given distance, the lower and upper error bounds (two times the standard deviation) calculated over all the validation steps.

Sample preparation

Cu6 and **Cu8** were synthesized as described in [7]. **Cu2** was synthesized as described in [9]. Samples: **Cu6** and **Cu8**: solvent: 3 : 1 butylnitrile : acetonitrile, copper concentration 0.63 mM (**Cu6**) and 0.83 mM (**Cu8**). **Cu2** solvent: 50% v/v glycerol : water solution, concentration 0.6 mM

5.3 Results

In this study DEER data were acquired by 9 GHz EPR spectroscopy on the **Cu8** and **Cu6** cages. A two-copper complex (**Cu2**), structure see figure SI2, was used as reference [9]. In the following, we present the outcome of the characterization.

The DEER traces obtained for **Cu8** and **Cu6** are shown in figure 2A. The length of the traces is 2 µs, a length that is similar to the DEER evolution time obtained in similar experiments on Cu(II)-pairs in the literature [32-34]. The traces of **Cu8** and **Cu6** are clearly different from one another. Both show an initial fast decay, which suggests the presence of short distances. In **Cu6**, there is a clear modulation maximum around 450 ns, while for **Cu8** there are no clear oscillations. The difference between the two traces is even more evident in figure 2B, where the traces are shown after background subtraction.

In figure 2C and 2D the distance distributions are shown. They are obtained considering only spin-pair contributions. For **Cu6** (figure 2C) two distinct distance peaks are observed, one is centered around 1.8 nm , and a second peak with approximately the same intensity is centered around 2.6 nm (see Table 1). A peak with a small population around 3.6 nm is seen, but validation shows that this peak is not reliable. The sample **Cu8** (figure 2D) also shows two distance peaks, at roughly similar distances, yet the peak centered at 1.8 nm is broader, respectively, and a shoulder around 2 nm can be discerned, also the intensity is larger than the one of the peak around 2.8 nm. A peak with a small population around 3.8 nm is seen, but validation shows that this peak is not reliable. All relevant distances are given in table 1. The distance peaks obtained for **Cu6** are narrower than the ones obtained for **Cu8**. In general, the width of the distance peaks is maximally 0.2 nm full width at half maximum (FWHM), in line with spin pairs in other rigid copper systems reported in the literature [9].

Since modulation depth strongly depends on experimental conditions, **Cu2** [9] was used as a reference compound. It contains two Cu(II) ions at a distance of 3.3 nm. The DEER properties of this reference sample agree with those measured before [9]. In figure 3, the DEER trace of **Cu2** (green trace) is shown alongside the DEER traces of **Cu6** and **Cu8**. The modulation depth is 23 % for **Cu6**, 22 % for **Cu8**, and 13 % for **Cu2**. Higher modulation depth is associated with multispin effects, revealing that the **Cu6** and **Cu8** DEER traces show

interactions between more than two Cu(II) ions. Quantitatively, equation 1 gives the relation between the number of interacting electron spins N and the modulation depth. For the cages, this relation shows interaction of approximately three spins, a number we will discuss in detail below.

Interaction of multiple spins with distances in the DEER sensitive range not only affects the modulation depth, but can also give rise to sum- and difference-frequencies that can manifest themselves as extra peaks in the distance distribution, so called ghost peaks. In figure 4, the effects of the application of the ghost suppression tool in DeerAnalysis, see Materials and methods, on the distance distributions are shown for three interacting spins. Similar effects are seen for higher numbers of spins, see figure SI5 and SI6 in the SI. The changes in the distance distribution upon ghost suppression (figure 4) are small, and none of the peaks are completely suppressed, showing that they are not ghost peaks. For **Cu6**, the longer distance peak (around 3.8 nm) shows the largest difference, but this distance was already considered non reliable after validation. For **Cu8**, small differences are also observed for the small feature between 3.5 and 4 nm. In the latter case, it appears that the peak shifts to a different distance, suggesting even more care when interpreting this distance.

Expected distances for the Cu cages

From quantum-mechanical calculations, model structures for **Cu6** and **Cu8** were obtained [7]. For **Cu6** and **Cu8**, two possible structures were found, which differ in the location of the Cu ions and thereby the Cu-Cu distances. In figure SI1, both models are shown. As described in detail in Bobylev *et al.* [7], for **Cu6** model 1, the Cu ions are located in the six square windows of the nanosphere, creating a shape close to an octahedron, see figure 1A, whereas in model 2, four copper ions are located below a palladium center and two in the square windows of the nanosphere (see SI for comparison of models 1 and 2 for **Cu6** and **Cu8** respectively). For **Cu8,** model 1, with the Cu-ions in the triangular windows, the copper ions are located at the corners of a cube, see figure 1B and SI1, while in model 2, six copper-ions are in the square windows and two in the triangular windows, forming a distorted cube (see figure SI1). For **Cu6** and **Cu8**, the models predict different Cu-Cu distances, see table 1, suggesting that the DEER distances could help in deciding between models.

For **Cu6**, the distances found by DEER agree slightly better with model 1, in agreement with conclusions drawn from other experimental evidence in Bobylev *et al.* [7]. For **Cu8**, the distances that are predicted for the two models overlap within their uncertainty margins, largely because in model 2 the deviation from a ideal cube is quite large. The DEER distances fall within the range of both models. Model 1 predicts two distances (2.0 and 2.8 nm) that are close to the experimental ones and a long distance (3.4 nm) that is not observed. The latter distance may be difficult to observe in the DEER experiments, see discussion. In

contrast to the situation in **Cu6**, the experimental distances do not enable to distinguish between the models, see discussion.

In principle, each pair of Cu ions within the distance range of the DEER experiment is expected to contribute to the distance distributions. Considering the geometric structure of the cages according to model 1 (figure 1), each Cu(II) ion has multiple neighbors with a distance within the DEER range. The expected intensity ratios of the distance peaks are given in table 1. For **Cu6**, model 1, each Cu(II) ion has four neighbors at a distance of 1.9 nm, and one at a distance of 2.7 nm, so the expected intensity ratio of the two distance peaks would be 4:1. For **Cu8,** model 1, each Cu(II) ion is expected to have three neighbors at 2 nm, three at 2.8 nm and one at 3.4 nm, so the expected ratio of the distance peaks is 3:3:1. The same holds for model 2, as long as it can be considered an almost ideal geometrical body.

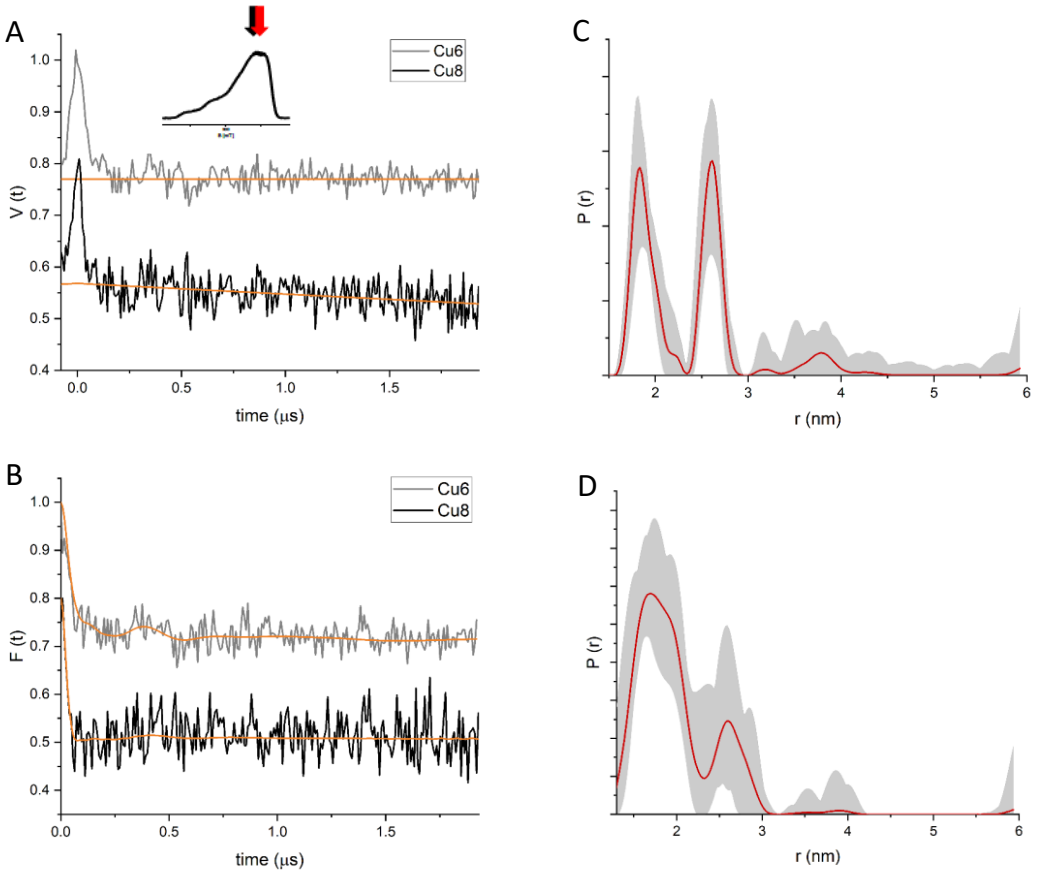

Figure 2. Results of DEER experiments of the **Cu6** and **Cu8** cages. A) Raw DEER traces. Gray: **Cu6**, black: **Cu8**. Orange: background. B) Background subtracted DEER traces with fits (orange). Gray: **Cu6** trace, black: **Cu8**. C) Distance distribution obtained for **Cu6** (red). D) Distance distribution obtained for **Cu8** (red). Maximum echo intensity (A,B) is normalized to unity, **Cu8** traces have been downshifted for better visibility. Shaded area in C) and D): standard deviation of each point in the distance distribution, by validation DEERAnalysis. Inset: field-swept-echo EPR spectrum of **Cu6**. Arrows: position of pump (red) and observer (black) frequency. V(t) : primary measured data, normalized to maximum intensity. F(t) : form factor obtained after background subtraction. For details and experimental parameters, see text.

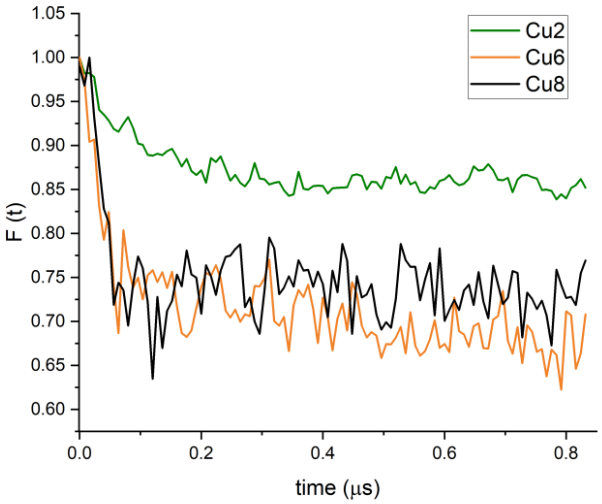

Figure 3**.** Comparison of the modulation depth of **Cu6** and **Cu8** with that of **Cu2**. DEER traces (background subtracted) obtained for **Cu6**, **Cu8** and **Cu2,** containing two Cu(II) ions at a distance of 3.3 nm. Green trace: **Cu2**, orange: **Cu6,** black: **Cu8**. Modulation depth of **Cu2** λ = 13%. In all traces maximum DEER-trace intensity is normalized to unity. For better S/N ratio, traces of **Cu6** and **Cu8** have shorter evolution time than in Fig. 2.

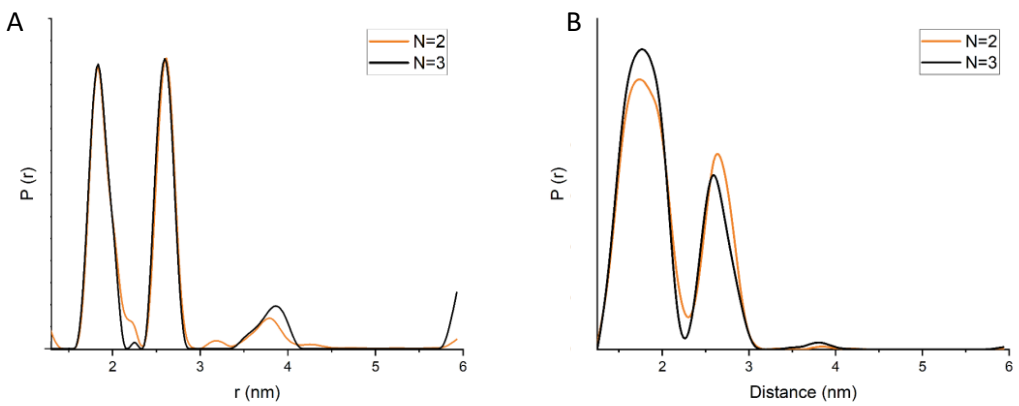

Figure 4. Effect of ghost suppression on distance distribution for three (N = 3) spins, compared with distance distribution for two (N = 2) spins. A) Effect of ghost suppression on **Cu6**. B) **Cu8**. Orange: distance distribution obtained without ghost suppression N = 2, black: distance distribution obtained with ghost suppression for N=3 spins. The areas below the P(r) curves were normalized to unity.

Table 1. DEER distances, modulation depth and model-derived distances for **Cu6** and **Cu8**. <r>: center of peak. Δ: measured modulation depth of the background-subtracted DEER traces. The expected intensity ratio is valid for both model 1 (M1) and model 2 (M2). DEER results are processed by Tikhonov regularization. Uncertainty for distances in model are derived from variations in Cu-Cu distances of

Cu6 distances from DEER	**Cu6 M1**	**Cu6 M2**	**expected intensity ratio Cu6**	**Cu6 Δ %**	**Cu8 distances from DEER**	**Cu8 M1**	**Cu8 M2**	**expected intensity ratio Cu8**	**Cu8 Δ %**
<r> (nm)	**r (nm)**	**r (nm)**		**23 ± 2**	**<r> (nm)**	**r (nm)**	**r (nm)**		**22 ± 2**
1.8	**1.8 ± 0.3**	**1.7 ± 0.3**	**4**		**1.8**	**2.0 ± 0.1**	**2.2 ± 0.6**	**3**	
2.6	**2.6 ± 0.3**	**2.7 ± 0.2**	**1**		**2.6**	**2.8 ± 0.1**	**3.1 ± 0.6**	**3**	
						3.5 ± 0.14	**3.8 ± 0.2**	**1**	

5.4 Discussion

Distance determination in multi-spin systems is an important extension to standard pair-distance determination by DEER. Up to now, such interactions were mostly investigated for nitroxide, trityl and Gd(III) systems [28, 30, 35-38]. The Cu(II)-cages, **Cu6** and **Cu8**, investigated here, represent an interesting model case that enables to extend multi-spin interactions to systems with a larger anisotropy. Two Cu-cages were investigated, comprising six (**Cu6**) and eight (**Cu8**) Cu(II) ions, respectively, in cage-like arrangements (see

figure 1). The structure of the cages was determined by a variety of techniques, as described in [7], where also their synthesis and properties are described. Here we describe the detailed investigation of these copper cages by DEER spectroscopy, to determine the distances between the Cu(II) ions and the impact of multispin interaction.

For both **Cu6** and **Cu8,** two models were proposed that differ in the location of the copper ions within the cage. For **Cu6** the measured distances are in slightly better agreement with those predicted from model 1, see table 1. That assignment agrees with other experimental results and firmly places the copper ions in the square windows of the Pd-ions, as shown in figure 1B. Whereas the distances observed in the DEER experiment agree well with those expected (table 1), the intensity of the DEER distance peaks deviate: The relative intensities of the distance peaks is 1:1, while 4:1 is expected (see table 1). Possible reasons for the too low intensity of the shorter distance peak (1.8 nm), amongst which orientation selection, are discussed in the SI. For **Cu8**, the predicted structure for model 2 deviates strongly from a cube, leading to larger deviations between Cu-Cu distances that would be identical in the cube. As a result, the model distances do not allow to discriminate between model 1 and model 2 for **Cu8**. Also, the overall lower signal-to-noise ratio of the **Cu8**-DEER traces, compared to **Cu6**, contributes to the difficulty. One causal factor is the shorter T_2 relaxation time of **Cu8** compared to **Cu6** (see SI). Comparison to model 1 (table 1) shows that the two shorter distances are not too far from the expectation from model 1, a third, longer distance, is missing (table 1). Even though the distance at 3.4 nm represents a single Cu-Cu pair and therefore could have a lower contribution to the distance distribution, at the expected ratio of 3:3:1 (table 1) it should still be seen. An explanation for the absence of the long distance peak for **Cu8** (3.4 nm in model 1) could be the uncertainty in the background correction in combination with the relatively short evolution time. In view of the deviations of model, is model 2 perhaps a better model? As model 2 does not account for the dominant distance of 1.7 nm measured (table 1), this does not seem to be the case. This leads to a preference for model 1, however with much less confidence than for **Cu6**, especially since also other experimental results [7] could not discriminate between the two models for **Cu8**. Possible scenarios for **Cu8** could be that the copper ligands, e.g. the pyrrolidine ligands [7], have different orientations, leading to a spread in copper positions and thereby broader distance distributions, or a coexistence of the two **Cu8** model structures, which would result in a superposition of the respective distances. Both possibilities could also lead to the larger width and more asymmetric shape of the distance peaks in **Cu8** compared to **Cu6**. Summarizing, all peaks observed in the distance distributions in **Cu6** and **Cu8** are accounted for by the expected pairwise distances. The distances found for **Cu6** and **Cu8** are reliable, since ghost suppression does not abolish any of the distance peaks, revealing that all

distance peaks of **Cu6** and **Cu8** are real. Additionally, as all peaks observed correspond to distances expected for the Cu-cages, full suppression of individual peaks is not likely.
The larger modulation depth of **Cu6** and **Cu8** compared to the reference compound (see results, Fig. 4) clearly shows that more than two spins interact, however, the number of interacting spins is lower than six (**Cu6**) resp. eight (**Cu8**), and several sources can contribute to the lower number. The uncertainty in the number of interacting spins derives from the signal-to-noise ratio of the DEER data (fig. 3) of both, the Cu-cages, and the reference compound (**Cu2**). Other effects, such as orientation selection and chemical factors, for example reduction of some of the Cu(II) centers in the cages, are difficult to quantify, but they would all lower the number of interacting spins, as described in the SI. Experimentally, some of these factors could be tackled, however, given the fragility of these samples this was not feasible (for details, see SI). Also, short phase memory time, T_m causes problems. Consequently, both Cu-cages display multispin properties, yet, the factors described result in a number of interacting spins that is significantly lower than expected, considering that there are six, respectively eight Cu centers in the two cages.
Both, theoretical studies of multispin effects [26-28] and experimental results [23, 36, 39] described in the literature, showed rather strong multispin effects on DEER distance distributions. In view of these results, the effects shown in figure 4 and figure SI5 and SI6 are weak. An obvious difference is that most of the systems described in the literature so far are nitroxide based. Nitroxides have a smaller spectral anisotropy than the Cu(II) centers investigated here, resulting in a higher pump-pulse-inversion efficiency λ for nitroxides compared to Cu(II). A clear indication of the small λ of the Cu(II) systems investigated here is the modulation depth Δ of only 13 % for **Cu2**, a two-Cu(II) system with λ = Δ, whereas for two-spin interactions in nitroxides modulation depths of around 50 % are standard at 9.5 GHz DEER [18]. Low pump-pulse-inversion efficiency also translates to low multispin excitation and thereby low ghost-peak intensities, as Edwards et al. have shown [30]. In the latter work, nitroxides had stronger ghost-peak contributions than Gd(III) labels, in agreement with the larger spectral anisotropy of Gd(III) with respect to nitroxides [30]. Evidently, this is also the case for the copper cages. Additionally, it was shown that multispin effects can be suppressed by lowering the inversion efficiency and power scaling [26-28].
The relative intensities of the distance peaks differ from those expected from the model, see above. One explanation could be that the intensitites are affected by ghost-peak effects. For example, Valera *et al.* [28] found that not in all cases ghost-peak suppression recovers the expected distance-peak intensities. Also, orientation selection could play a role, see SI, however, no quantitative estimate can be given at this point.
In conclusion, the two copper cages **Cu6** and **Cu8**, show that multispin effects can also be tackled in Cu(II)-based systems and that DEER is an excellent tool to obtain structure

information in multi-copper systems. This extends the reach of DEER for multispin systems, whether biological or chemical, be it for catalysis systems or those of interest for material sciences.

Supplementary Information

Meaning of geometric interpretation, Cu8: cube, Cu6: octahedron

The description of the arrangement of the Cu-ions in the cages as a cube (**Cu8**) or an octahedron (**Cu6**) facilitates the description of the arrangement of the Cu-ions, but does not imply that the ions form an idealized geometric body. The uncertainty range for the distances obtained from the models (Table 1, main text) gives the range of distances of individual pairs of Cu-ions. In an ideal cube or octahedron all distances between the specific types of Cu-ions should be identical. However, especially the model 2 structures show clear deviations from the shapes, as seen in figure SI1, where the distortions already can be seen in the figure.

The corners of polyhedra also have specific relations between distances: In a cube, the relation between the shortest distance (distance ***a***) along the edge of the cube and the face-diagonal (distance ***b***) is $\boldsymbol{b} = 1/\sqrt{2}\,\boldsymbol{a}$, the same as the ratio between the shorter and the longer distance in an octahedron. As a result, the distances in **Cu6** and **Cu8** are expected to follow this ratio.

Overview of measurement

The DEER traces presented here can be compared to those shown in Bobylev *et al.* [7]. For **Cu6**, increasing the accumulation time and optimizing the pulse-excitation resulted in a better signal-to-noise ratio, increasing the confidence level for the distance-distribution shape compared to the traces shown in figure 8 and 10 of [7], while leading to the same distances as before. For **Cu8**, several attempts to improve the signal-to-noise ratio in a similar way did not improve the data due to a combination of factors, suggesting that the shorter T_m time or other chemical factors cause the lower signal-to-noise ratio compared to what can be achieved for **Cu6**. In [7] DEER was one of several methods to verify the structure of the cages, so the focus was on the distances only. In the present manuscript, the number of interacting spins is determined by a direct comparison with a two-copper model compound (**Cu2**) enabling detailed analysis of this point in the multi-copper systems investigated. Additionally several different analysis methods were applied (Gaussian analysis of DEER traces, and DeerNet), see below, to quantitate the reliability of the analysis. Most of the differences observed with respect to [7], such as that the second distance peak in the **Cu8** distance distribution centered at 2.6 nm, see figure 2, is reliable, result in a higher confidence in the interpretation and are due to the better signal to noise ratio of the data.

Reproducibility was checked by measuring samples multiple times, and also measuring samples that had not been measured before. In between measurements, the EPR tubes with

the samples were stored in liquid nitrogen, and introduced into the precooled resonator, to avoid accidental warming of the samples as much as possible.

Possible orientation selection effects in the DEER traces

As mentioned in the main text, orientation-selection effects can lead to a reduction of the copper-copper interaction observed by DEER, which reduces the modulation depth, i.e. the total number of spins interacting (see discussion main text). Also, orientation selection can affect specific pairs of spins more strongly than others, which would cause a deviation of the relative intensity of the distance peaks from the expected intensities given in table 1, main text. In the DEER experiments, both the pump- and the observer frequencies were positioned in the perpendicular region of the EPR spectrum, see figure 2 main text and figure SI3. Therefore, spin pairs in which the parallel component, i.e. g_{zz}, of the g-tensor of one Cu(II) is parallel to the perpendicular component, i.e. the g_{xx}-g_{yy} plane, of the other Cu(II) will not contribute to the DEER effect, because for these pairs only one of the two partners are excited. The actual orientation of g-tensors of pair could also be in between the extremes, leading to partial excitation of a pair, for example. Consequently, the relative orientation of the g-tensors of two coppers in the cages determines how much these two Cu(II) centers contribute to the DEER effect. This can lead to reduced or absent DEER effects for specific pairs. As the g-tensor directions of the Cu(II)-centers in the Cu-cages are not known, the contribution of this effect cannot be estimated. Experimentally, orientation effects can be determined by setting the pump-pulse to a parallel and the observer pulse to a perpendicular position in the EPR spectrum, and vice versa, however, for Cu(II), the limited bandwidth of the resonator does not allow this. Other approaches have been used as well, see [40-43], however, in the present case, the sensitivity was not sufficient to measure meaningful DEER traces in the parallel region of the spectrum, as would be needed to use such an approach. Thus, orientation-selection effects can effectively lower the number of spins observed, and can lead to a difference in the relative intensity of distance peaks from those expected, see below.

Applying different analysis methods for DEER data

Different analysis methods for the DEER data were tested to (i) determine the reliability of the analysis described in the main text and (ii) to investigate if other interpretations are compatible with the data.

(i) The DeerNet analysis (figure SI 9 and 10) shows that also the shape of the distance distribution is robust and agrees with the Tikhonov analysis, as confidence levels and shape agree. For using DeerNet, unfortunately, the signal-to-noise ratio (12 for **Cu6** and 9 for **Cu8**) is at or below the limit of the S/N-ratio recommended in DeerNet. So in this case, the

advantage of the DeerNet program, namely that processing of baseline and form factor is user-invention free [44, 45], cannot be fully harnessed: The simulated form-factor contribution, especially for **Cu8**, figure SI 10A, is less smooth than we would chose. The DEERNet option to do Tikhonov analysis shown in Fig. SI 9B and 10B can be directly compared to that in Fig. 2B, main text, showing that a smaller regularization parameter selected in the user-adjusted Tikhonov regularization smoothens out some of the features that we interpret as noise. So we see that in this very specific case, while DeerNet confirms the overall distance distribution, and unambigously quantifies trace parameters such as the signal-to-noise ratio, it cannot be used as the only method of data analysis.
(ii) Analysis of the data with Gaussian distance distributions enables to change distance parameters, such as center-distance and -width of the distance peaks individually. Here we checked if the distance peaks could have different widths, however, as figure SI7 and SI8 show, the optimum solution is similar to the Tikhonov one.
Also, we tested if different relative weights of the distance peaks were compatible with the data, given that the expected intensity of the distance peaks (see Tab. 1, main text) deviates from those found in Tikhonov analysis.
We found that for **Cu6**, changing the weight by more than 25 %, maintaining the width constant, results in significant deviation from the experimental DEER curve (data not shown), revealing that the deviation of the relative weights of the respective distances from the expected intensity ratios of the distance peaks (table 1, main text) is outside the experimental uncertainty. In the case of **Cu8**, also simulating with two Gaussian distance peaks is possible, (data not shown), probably attributable to the intrinsically low population of the third distance peak at 3.4 nm. For these tests, the distance and the width of the distance peaks were kept within a narrow range, so it cannot be excluded that larger variations of the relative weights of the distance peaks would be possible if the other parameters are changed more extensively. Due to the overall low signal-to-noise ratio of the data we did not expect unambiguous solutions.

Modulation depth and the relative intensities of the distance peaks

Deviations of the intensity of the distance peaks (figure 2, main text) from the expected intensities (Table 1 main text) can be due to incomplete ghost-peak supression in multispin systems as described in the main text. Specific factors can also enter: For **Cu6**, instead of the expected ratios of 4:1 (1.8 nm relative to 2.6 nm peak, figure 2) the distance peak at 1.8 nm is somehwat broadened, but not four times more intense than the distance peak at 2.6 nm. One reason could be a less favorable orientation selection for the Cu-pairs at the shorter distance, resulting in a smaller probability to excite just these pairs, and thereby causing lower intensity of the specific distance peak, see above. Also, the model predicts that the

distance between some Cu-pairs may be as short as 1.5 nm. For such short distances, the excitation bandwidth of the pulses would not be sufficient, resulting in a smaller contribution of these distances, and thereby, again, a smaller intensity for the distance peak at 1.8 nm. We tested this with the limited-bandwidth-excitation feature in DeerAnalysis but found only small changes, so it is probably not the main factor contributing. For **Cu8**, similar arguments than for **Cu6** can be made. In addition, the overall broader lines in the distance distribution could be an indication that, as seen in model 2, multiple conformations contribute and that the superposition of those conformations of the cage smear out the distance peaks.

Why not all spins in the cages are observed

Several factors contribute to the uncertainty of the number of interacting spins determined: Measurement and interpretation of the modulation depth requires that sample and reference are measured with precisely the same conditions. Therefore, measurements were performed in the same experimental run, to minimize day to day variations, and with shorter evolution times to improve signal-to-noise ratios. Also, the spectra of sample and reference must have similar anisotropies. As figure SI3 shows, the EPR spectra of the Cu-cages and the reference compound almost overlap, showing that this condition is fulfilled. Several other factors, such as orientation selection (see above) and partial reduction the Cu-ions in the cages [7] , can lead to a smaller number of spins measured than expected. Another factor that can reduce modulation depth is a contribution of short distances, since for short distances, the excitation bandwidth of the pulses is not sufficient to excite the dipolar interaction. As a result, pairs at very short distances, roughly below 1.6 nm at our experimental conditions, would contribute less, or not at all to the modulation depth. This may contribute here, as the DEER time traces (figure 2, main text) show a fast initial decay, suggesting a contribution of spin-pairs at short distances, and, for **Cu6**, the models show distances can be as short as 1.5 nm. Also, orientation selection, described above, can cause specific pairs of spins to contribute less to the modulation depth than others. As several of the factors described reduce the modulation depth, the measured value can be considered as a lower limit.

Supplementary figures

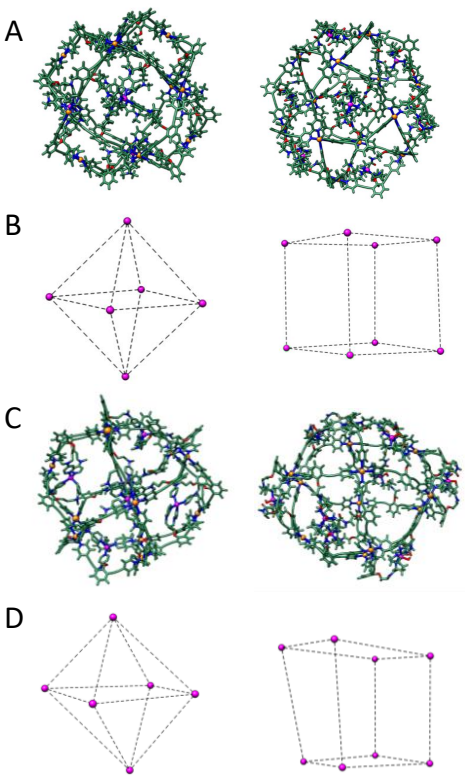

Figure SI.1. Model structures of copper cages. A) Model 1 structures. B) Relative position of the copper ions in model 1. C) Model 2 structures. D) relative position of the copper ions in model 2. Left: **Cu6**, right: **Cu8**. Orange: Palladium, Magenta: Copper ions. See main text and Bobylev *et al.* [7].

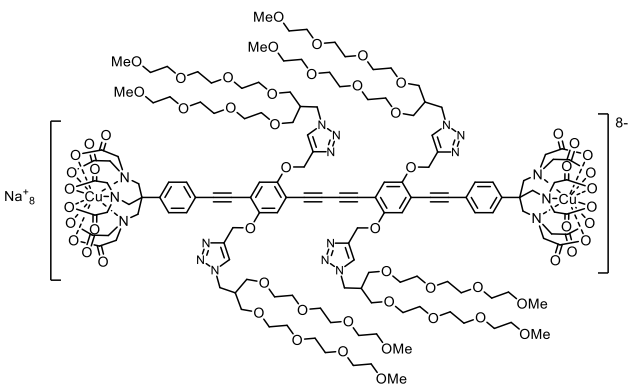

Figure SI.2. Structure of **Cu2**, used as a two copper reference. For details, see main text.

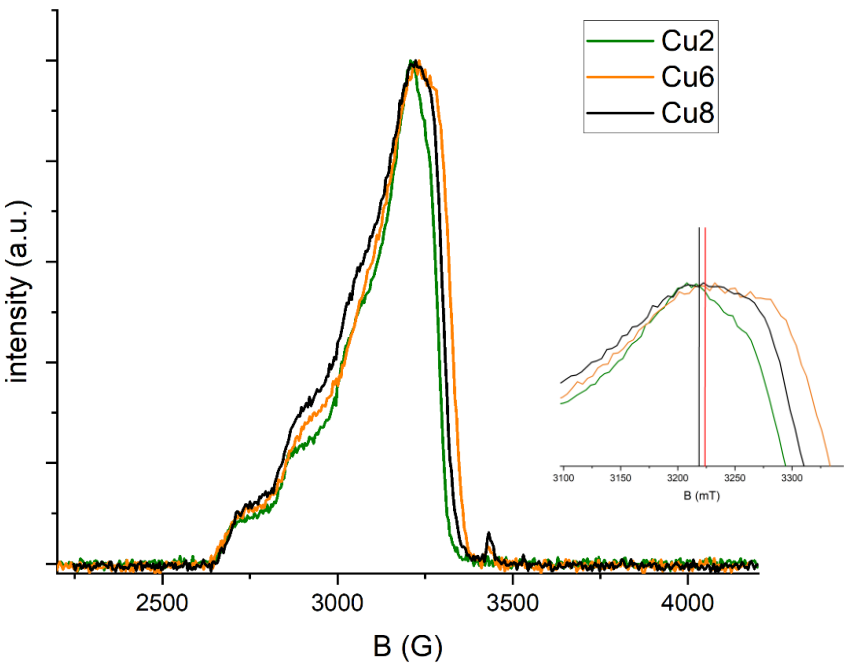

Figure SI.3. Field swept echo detected EPR spectra of all compounds. Green: **Cu2**, orange: **Cu6**, black: **Cu8**. Spectra were baseline corrected and normalized to maximum intensity. Overall similarity of spectra suggests that excitation in DEER is similar, but differences in orientation selection cannot be excluded (see text). The lines in the inset indicate position of the pump (red) and observer (black) pulses.

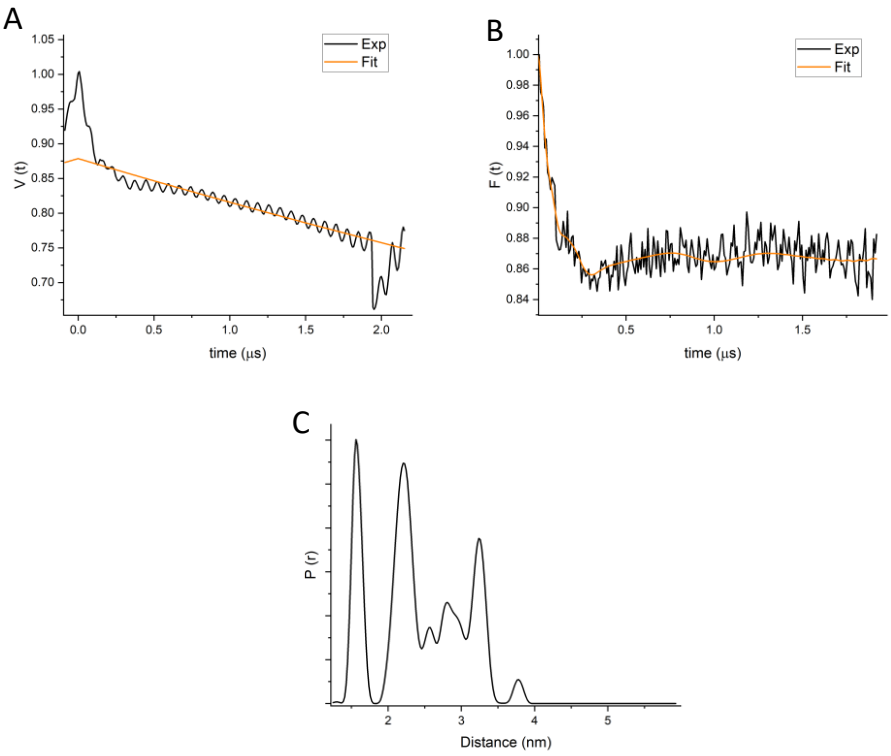

Figure SI.4. Results of DEER experiments with **Cu2**. A) Raw DEER trace (black) background (orange). B) Background subtracted DEER trace (black) with fit (orange). Maximum echo intensity (A,B) is normalized to unity. V(t) : primary measured data, normalized to maximum intensity. F(t) : form factor obtained after background subtraction. For details and experimental parameters, see text. C) Distance distribution obtained for **Cu2:** expected distance is 3.3 nm. It was shown in Keller *et al.* [9] that several peaks of the distance distribution derive from contributions of weak exchange-coupling, for which we do not correct here. Peak at 1.5 nm: possible artifact for non-completely suppressed proton modulation.

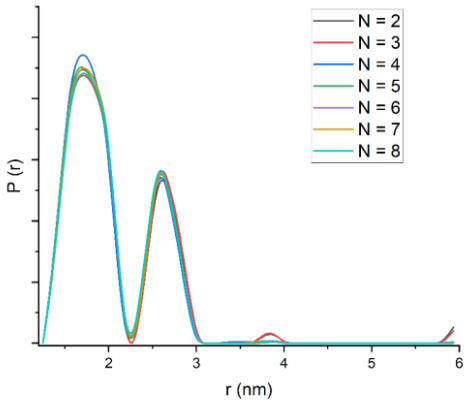

Figure SI.5. Effect of ghost suppression on **Cu8** distance distribution, from N = 2 to to N = 8, eight interacting Cu(II). For details, see Materials and Methods section and main text.

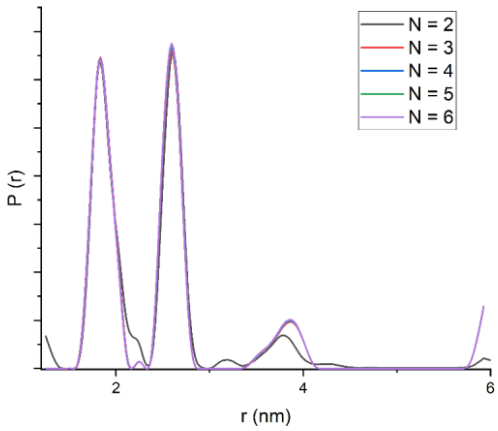

Figure SI.6. Effect of ghost suppression on **Cu6** distance distribution, from N = 2 to N = 6. For details, see Materials and Methods section and main text.

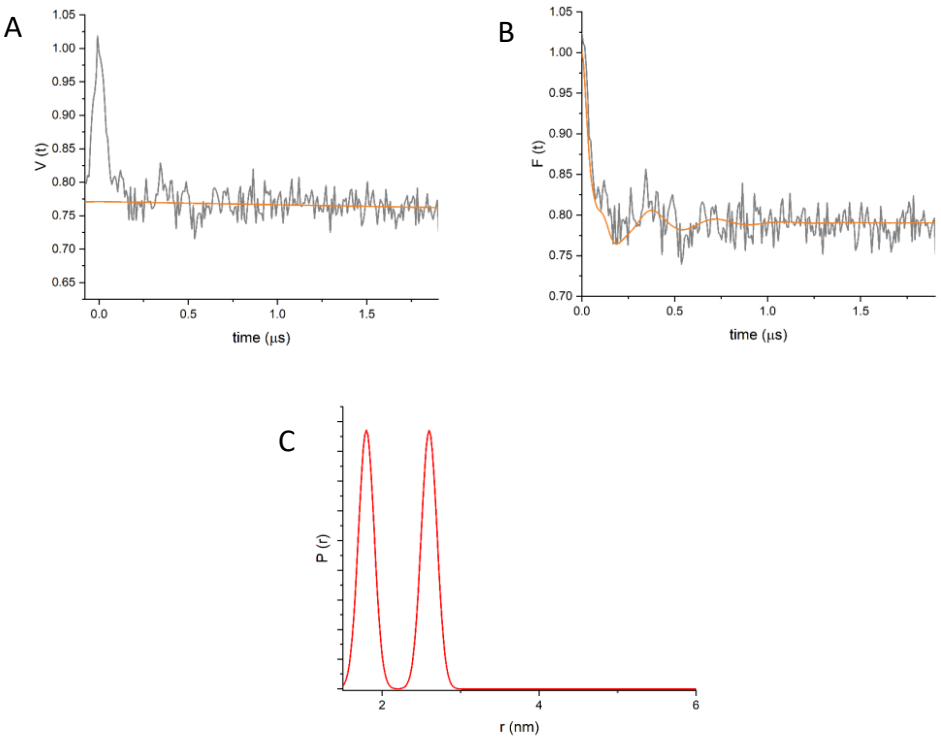

Figure SI.7. **Cu6** data analyzed with two-Gaussian fitting in DeerAnalysis. A) DEER trace (grey) and background (orange), B) background subtracted trace (grey) and fit (orange) C) distance distribution. N=2 spins, and two Gaussian peaks centered at 1.8 and 2.6 nm. Manually changing the width or center of the Gaussians did not significally improve the agreement with the data. For details, see text.

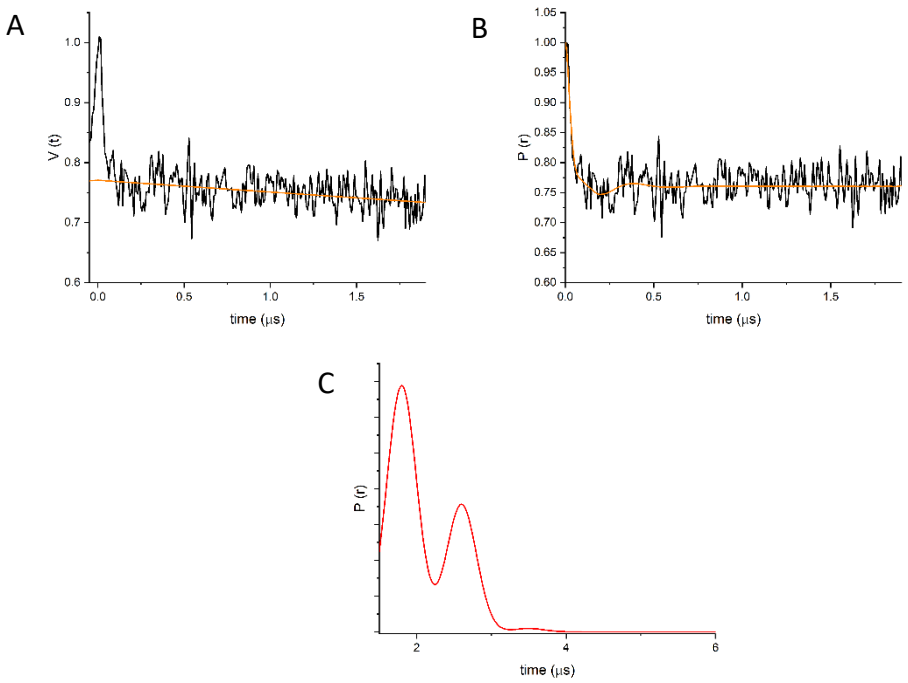

Figure SI.8. **Cu8** data analyzed with three-Gaussian fitting in DeerAnalysis. A) DEER trace (black) and background (orange), B) background subtracted trace (black) and fit (orange) C) distance distribution. N=2 spins, and three Gaussian peaks centered at 1.8, 2.6 and 3.5 nm. Manually changing the width or center of the Gaussians did not significally improve the agreement with the data. For details, see text.

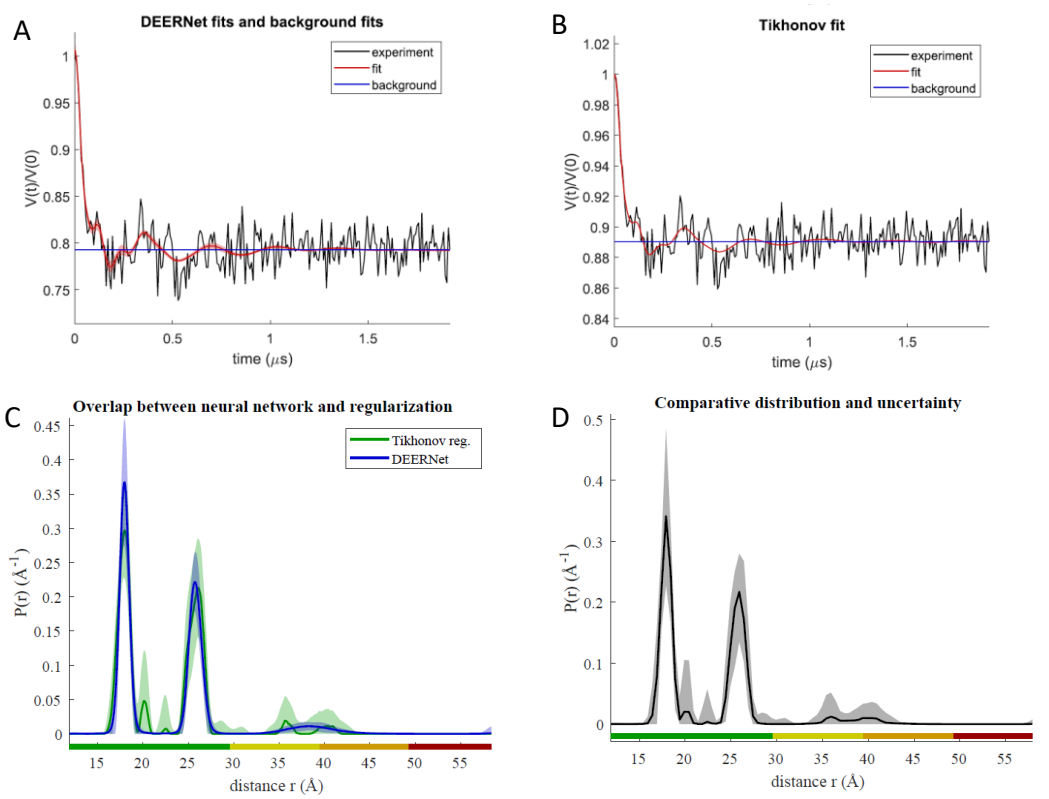

Figure SI.9. **Cu6** data analyzed with DEERNet tool in DeerAnalysis 2023. A) Deer trace (black), background (blue), fit (red) from DEERNet. B) Deer trace (black), background (blue), fit (red) from Tikhonov regularization. C) distance distribution, comparison between DEERNet (blue) and Tikhonov regularization (green). D) Comparative distribution from C). Shaded area in C) and D): uncertainty margins. The colors on the abscissa axis of the distance distribution indicate reliability of distance peaks: green: shape of distance distribution is reliable, yellow: mean distance and width are reliable, orange: mean distance is reliable, red: distance may be detectable, but cannot be quantified. Compared to the Tikhonov results shown in the main text (Figure 2), the regularization parameters is larger, which we consider an over-interpretation of the data.

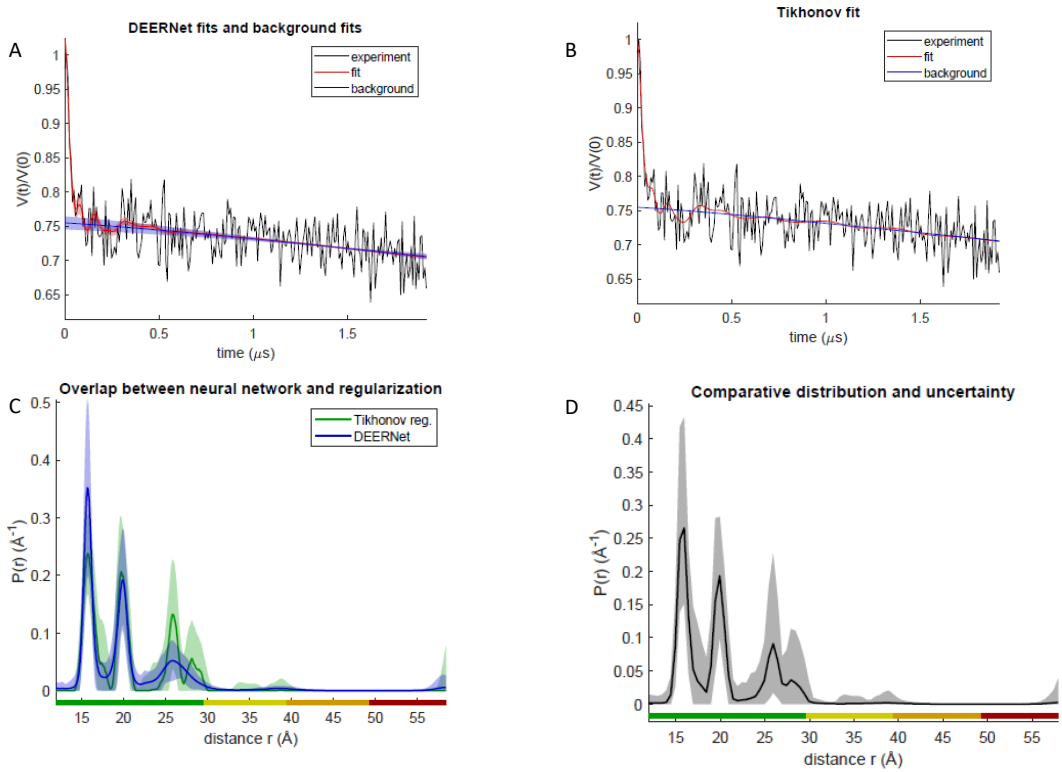

Figure SI.10. **Cu8** data analyzed with DEERNet tool in DeerAnalysis 2023. A) Deer trace (black), background (blue), fit (red) from DEERNet. B) Deer trace (black), background (blue), fit (red) from Tikhonov regularization. C) distance distribution, comparison between DEERNet (blue) and Tikhonov regularization (green). D) Comparative distribution from C). Shaded area in C) and D): uncertainty margins. The colors on the abscissa axis of the distance distribution indicate reliability of distance peaks: green: shape of distance distribution is reliable, yellow: mean distance and width are reliable, orange: mean distance is reliable, red: distance may be detectable, but cannot be quantified. Overall, DEERNET confirms results presented in main text. In contrast to the Tikhonov results shown in figure 2 (main text), the main peak at 1.7 nm is split into two peaks (1.6 and 2.0 nm), however, the data are at the lower end of the recommened signal to noise ratio for DeerNet. Compared to the Tikhonov results shown in the main text, the regularization parameters is larger, which we consider an over-interpretation of the data. Overall, DEERNet confirms results presented in main text.

Table SI 1 Measured relaxation time constants for the cages **Cu6** and **Cu8**. T_m: phase-memory time. T_1: spin-lattice-relaxation time. The T_m relaxation was measured with the two-pulse sequence (π/2)-τ- (π)- τ-[echo] with an initial τ of 200 ns and 4 ns step increments. The T_1 relaxation was measured with the inversion-recovery sequence (π)- T-(π/2)-τ- (π)- τ-[echo]. The τ value was kept constant at 200 ns, starting T value was 400 ns with 40 ns step increments. 16 ns length for π/2 pulses and 32ns for π pulses were used. The T_m and T_1 time constants were obtained through exponential fitting. Measurement temperature: 30K.

	Cu6	**Cu8**
T_m (ns)	**522 ± 11**	**302 ± 7**
T_1 (µs)	**8.7 ± 0.4**	**15.4 ± 0.5**

References

[1] M.J. Wiester, P.A. Ulmann, C.A. Mirkin, Enzyme mimics based upon supramolecular coordination chemistry, Angew Chem Int Ed Engl 50(1) (2011) 114-37.
[2] T. Brugnari, D.M. Braga, C.S.A. dos Santos, B.H.C. Torres, T.A. Modkovski, C.W.I. Haminiuk, G.M. Maciel, Laccases as green and versatile biocatalysts: from lab to enzyme market—an overview, Bioresources and Bioprocessing 8(1) (2021).
[3] R. Guo, J. Gu, S. Zong, M. Wu, M. Yang, Structure and mechanism of mitochondrial electron transport chain, Biomed J 41(1) (2018) 9-20.
[4] P. Brzezinski, A. Moe, P. Adelroth, Structure and Mechanism of Respiratory III-IV Supercomplexes in Bioenergetic Membranes, Chem Rev 121(15) (2021) 9644-9673.
[5] M. Ruben, J.M. Lehn, P. Muller, Addressing metal centres in supramolecular assemblies, Chem Soc Rev 35(11) (2006) 1056-67.
[6] L. Chen, Z. Guo, X.G. Wei, C. Gallenkamp, J. Bonin, E. Anxolabehere-Mallart, K.C. Lau, T.C. Lau, M. Robert, Molecular Catalysis of the Electrochemical and Photochemical Reduction of CO2 with Earth-Abundant Metal Complexes. Selective Production of CO vs HCOOH by Switching of the Metal Center, J Am Chem Soc 137(34) (2015) 10918-21.
[7] E.O. Bobylev, L. Passerini, F.J. de Zwart, D.A. Poole, S. Mathew, M. Huber, B. de Bruin, J.N.H. Reek, Pd12MnL24 (for n = 6, 8, 12) nanospheres by post-assembly modification of Pd12L24 spheres, Chemical Science 14 (2023) 11840-11849.
[8] B. Huang, L. Mao, X. Shi, H.B. Yang, Recent advances and perspectives on supramolecular radical cages, Chem Sci 12(41) (2021) 13648-13663.
[9] K. Keller, I. Ritsch, H. Hintz, M. Hülsmann, M. Qi, F.D. Breitgoff, D. Klose, Y. Polyhach, M. Yulikov, A. Godt, G. Jeschke, Accessing distributions of exchange and dipolar couplings in stiff molecular rulers with Cu(II) centres, Phys Chem Chem Phys 22(38) (2020) 21707-21730.
[10] Y. Ozaki, M. Kawano, M. Fujita, Engineering noncovalent spin-spin interactions in an organic-pillared spin cage, Chem Commun (Camb) (28) (2009) 4245-7.
[11] K. Nakabayashi, Y. Ozaki, M. Kawano, M. Fujita, A self-assembled spin cage, Angew Chem Int Ed Engl 47(11) (2008) 2046-8.
[12] W.L. Jiang, Z. Peng, B. Huang, X.L. Zhao, D. Sun, X. Shi, H.B. Yang, TEMPO Radical-Functionalized Supramolecular Coordination Complexes with Controllable Spin-Spin Interactions, J Am Chem Soc 143(1) (2021) 433-441.
[13] S.A.D. K. M. SALIKHOV, AND A. M. RAITSIMRING, The Theory of Electron Spin-Echo Signal Decay Resulting from Dipole-Dipole Interactions between Paramagnetic Centers in Solids, jOURNAL OF MAGNETIC RESONANCE 42 (1981) 255 - 276.
[14] M. Pannier, S. Veit, A. Godt, G. Jeschke, H.W. Spiess, Dead-time free measurement of dipole-dipole interactions between electron spins. 2000, J Magn Reson 213(2) (2011) 316-25.
[15] F.D. Breitgoff, K. Keller, M. Qi, D. Klose, M. Yulikov, A. Godt, G. Jeschke, UWB DEER and RIDME distance measurements in Cu(II)-Cu(II) spin pairs, J Magn Reson 308 (2019) 106560.
[16] M.U. Irene M. C. van Amsterdam, Gerard W. Canters, and Martina Huber, Measurement of a Cu-Cu Distance of 26 A by a Pulsed EPR Method, Angew. Chem. Int. Ed 42(1) (2003) 62-64.

[17] M.M. Roessler, M.S. King, A.J. Robinson, F.A. Armstrong, J. Harmer, J. Hirst, Direct assignment of EPR spectra to structurally defined iron-sulfur clusters in complex I by double electron-electron resonance, Proc Natl Acad Sci U S A 107(5) (2010) 1930-5.
[18] G. Jeschke, DEER distance measurements on proteins, Annu Rev Phys Chem 63 (2012) 419-46.
[19] O. Schiemann, C.A. Heubach, D. Abdullin, K. Ackermann, M. Azarkh, E.G. Bagryanskaya, M. Drescher, B. Endeward, J.H. Freed, L. Galazzo, D. Goldfarb, T. Hett, L. Esteban Hofer, L. Fabregas Ibanez, E.J. Hustedt, S. Kucher, I. Kuprov, J.E. Lovett, A. Meyer, S. Ruthstein, S. Saxena, S. Stoll, C.R. Timmel, M. Di Valentin, H.S. McHaourab, T.F. Prisner, B.E. Bode, E. Bordignon, M. Bennati, G. Jeschke, Benchmark Test and Guidelines for DEER/PELDOR Experiments on Nitroxide-Labeled Biomolecules, J Am Chem Soc 143(43) (2021) 17875-17890.
[20] D.M. Bela E. Bode , Jorn Plackmeyer , Gerd Durner, Thomas F. Prisner, Olav Schiemann, Counting the monomers in nanometer-sized oligomers by pulsed electron-electron double resonance, JACS 129 (2007) 6736-6745.
[21] A.D.Milov, Yu.D.Tsvetkov, F.Formaggio, M.Crisma, C.Toniolo, a. J.Raap, The Secondary Structure of a Membrane-Modifying Peptide in a Supramolecular Assembly Studied by PELDOR and CW-ESR Spectroscopies, J. Am. Chem. Soc. 123 (2000) 3784-3789.
[22] A. D. Milov, Yu. D. Tsvetkov, a.J. Raap, Aggregation of Trichogin Analogs in Weakly Polar Solvents: PELDOR and ESR Studies, Appi. Magn. Reson 19 (1998) 215-226.
[23] M.J. Junk, H.W. Spiess, D. Hinderberger, DEER in biological multispin-systems: a case study on the fatty acid binding to human serum albumin, J Magn Reson 210(2) (2011) 210-7.
[24] E.R. Georgieva, P.P. Borbat, H.D. Norman, J.H. Freed, Mechanism of influenza A M2 transmembrane domain assembly in lipid membranes, Sci Rep 5 (2015) 11757.
[25] P.S. Kerry, H.L. Turkington, K. Ackermann, S.A. Jameison, B.E. Bode, Analysis of influenza A virus NS1 dimer interfaces in solution by pulse EPR distance measurements, J Phys Chem B 118(37) (2014) 10882-8.
[26] T. von Hagens, Y. Polyhach, M. Sajid, A. Godt, G. Jeschke, Suppression of ghost distances in multiple-spin double electron-electron resonance, Phys Chem Chem Phys 15(16) (2013) 5854-66.
[27] M.S. Gunnar Jeschke, Miriam Schulteb and Adelheid Godt, Three-spin correlations in double electron–electron resonance, Phys Chem Chem Phys 11(31) (2009) 6580-6591.
[28] K.A. Silvia Valera, Christos Pilotas, Hexian Huang, James H. Naismith, Bela E. Bode, Accurate Extraction of Nanometer Distances in Multimers by Pulse EPR, ChemPubSoc Europe 22 4700 - 4703.
[29] K. Ackermann, B.E. Bode, Pulse EPR distance measurements to study multimers and multimerisation, Molecular Physics 116(12) (2018) 1513-1521.
[30] D.T. Edwards, T. Huber, S. Hussain, K.M. Stone, M. Kinnebrew, I. Kaminker, E. Matalon, M.S. Sherwin, D. Goldfarb, S. Han, Determining the oligomeric structure of proteorhodopsin by Gd3+ -based pulsed dipolar spectroscopy of multiple distances, Structure 22(11) (2014) 1677-86.

[31] V.C. G. Jeschke, P. Ionita, A. Godt, H. Zimmermann, J. Banham, C. R. Timmel, D. Hilger, and H. Jung, DeerAnalysis2006 - a Comprehensive Software Package for Analyzing Pulsed ELDOR Data, Applied Magnetic Resonance 30 (2006) 473 - 498.
[32] S. Ghosh, M.J. Lawless, H.J. Brubaker, K. Singewald, M.R. Kurpiewski, L. Jen-Jacobson, S. Saxena, Cu2+-based distance measurements by pulsed EPR provide distance constraints for DNA backbone conformations in solution, Nucleic Acids Res 48(9) (2020) e49.
[33] D.M. Engelhard, A. Meyer, A. Berndhauser, O. Schiemann, G.H. Clever, Di-copper(ii) DNA G-quadruplexes as EPR distance rulers, Chem Commun (Camb) 54(54) (2018) 7455-7458.
[34] J.E. Lovett, A.M. Bowen, C.R. Timmel, M.W. Jones, J.R. Dilworth, D. Caprotti, S.G. Bell, L.L. Wong, J. Harmer, Structural information from orientationally selective DEER spectroscopy, Phys Chem Chem Phys 11(31) (2009) 6840-8.
[35] A. Meyer, J.J. Jassoy, S. Spicher, A. Berndhäuser, O. Schiemann, Performance of PELDOR, RIDME, SIFTER, and DQC in measuring distances in trityl based bi- and triradicals: exchange coupling, pseudosecular coupling and multi-spin effects, Physical Chemistry Chemical Physics 20(20) (2018) 13858-13869.
[36] K. Ackermann, C. Pliotas, S. Valera, J.H. Naismith, B.E. Bode, Sparse Labeling PELDOR Spectroscopy on Multimeric Mechanosensitive Membrane Channels, Biophysical Journal 113(9) (2017) 1968-1978.
[37] A. Meyer, D. Abdullin, G. Schnakenburg, O. Schiemann, Single and double nitroxide labeled bis(terpyridine)-copper(II): influence of orientation selectivity and multispin effects on PELDOR and RIDME, Phys Chem Chem Phys 18(13) (2016) 9262-71.
[38] L. Fabregas-Ibanez, V. Mertens, I. Ritsch, T. von Hagens, S. Stoll, G. Jeschke, Dipolar pathways in multi-spin and multi-dimensional dipolar EPR spectroscopy, Phys Chem Chem Phys 24(37) (2022) 22645-22660.
[39] A. Giannoulis, R. Ward, E. Branigan, J.H. Naismith, B.E. Bode, PELDOR in rotationally symmetric homo-oligomers, Mol Phys 111(18-19) (2013) 2845-2854.
[40] A.M. Bowen, M.W. Jones, J.E. Lovett, T.G. Gaule, M.J. McPherson, J.R. Dilworth, C.R. Timmel, J.R. Harmer, Exploiting orientation-selective DEER: determining molecular structure in systems containing Cu(ii) centres, Physical Chemistry Chemical Physics 18(8) (2016) 5981-5994.
[41] B.E. Bode, J. Plackmeyer, T.F. Prisner, O. Schiemann, PELDOR Measurements on a Nitroxide-Labeled Cu(II) Porphyrin: Orientation Selection, Spin-Density Distribution, and Conformational Flexibility, The Journal of Physical Chemistry A 112(23) (2008) 5064-5073.
[42] T.F. Prisner, A. Marko, S.T. Sigurdsson, Conformational dynamics of nucleic acid molecules studied by PELDOR spectroscopy with rigid spin labels, Journal of Magnetic Resonance 252 (2015) 187-198.
[43] A.M. Bowen, C.E. Tait, C.R. Timmel, J.R. Harmer, Orientation-Selective DEER Using Rigid Spin Labels, Cofactors, Metals, and Clusters, in: C.R. Timmel, J.R. Harmer (Eds.), Structural Information from Spin-Labels and Intrinsic Paramagnetic Centres in the Biosciences, Springer Berlin Heidelberg, Berlin, Heidelberg, 2013, pp. 283-327.
[44] J. Keeley, T. Choudhury, L. Galazzo, E. Bordignon, A. Feintuch, D. Goldfarb, H. Russell, M.J. Taylor, J.E. Lovett, A. Eggeling, L. Fábregas Ibáñez, K. Keller, M. Yulikov, G. Jeschke, I.

Kuprov, Neural networks in pulsed dipolar spectroscopy: A practical guide, Journal of Magnetic Resonance 338 (2022) 107186.
[45] S.G. Worswick, J.A. Spencer, G. Jeschke, I. Kuprov, Deep neural network processing of DEER data, Science Advances 4(8) eaat5218.

.

Summary

Electron paramagnetic resonance (EPR) spectroscopy has long been a valuable tool to study biological systems. In enzymes, proteins that catalyze chemical reactions, EPR enables direct insight into the electronic and geometric structure of the active site and the reaction mechanism. Moreover, the advent of site-directed spin labeling (SDSL), a technique that places (spin) probes on specific sites on proteins, further expanded the utility of EPR, allowing for the investigation of protein dynamics and structural conformations, especially with advances in EPR techniques and tailored spin labels. This thesis explores the application of EPR spectroscopy to biological systems, tackling both technical and biochemical challenges.

Chapter 2 investigates a long-overlooked side reaction in site-directed spin labeling: the dimerization of the nitroxide spin label MTSL. Protein labeling consists of the incubation of a mixture of protein and label solution. Under common labeling conditions, two MTSL-molecules combine to form a dimer side product that limits labeling efficiency and leads to waste of the spin probe. By combining EPR and mass spectrometry, a technique that allows measuring the molecular mass and predict the chemical composition of compounds in solution, the structure and formation mechanism of the dimer are elucidated. The results reveal that dimerization results in a dimer covalently linked by a disulfide bond. The process is irreversible in the sense that it does not allow for recovery of the spin label. This side reaction, long observed through its EPR signature but never fully understood, is now clearly characterized and rationalized, shedding light on a persistent issue in the field of spin labeling.

Chapter 3 uses EPR to explore the aggregation of the protein α-Synuclein (αS), a process that occurs in neurons and that is connected to Parkinson's disease. The toxic species in this disease are believed to be the oligomeric intermediates, forming at the early stages of αS aggregation. Such intermediates are transient and structurally heterogeneous, which makes them difficult to study. Using SDSL-EPR, αS mutants were labeled at specific residues and monitored during aggregation. In combination with a standard assay commonly used to monitor αS aggregation, the study shows that EPR allows monitoring the aggregation in situ, and captures structural changes during the formation of intermediates and final aggregates. This capability is especially valuable given that traditional assays cannot detect intermediate species. The approach offers a promising path for dissecting the molecular mechanisms of amyloid formation and for obtaining structural information on the aggregate species.

Chapter 4 addresses the challenges of studying short-lived reaction intermediates in enzymes. These are transient states that appear while an enzyme is performing a reaction, and sometimes lasts only a few seconds, or even milliseconds, making them challenging to study. Rapid freeze-quench (RFQ) techniques, which involve rapid freezing of a reaction mixture, are often used to trap and stabilize intermediates, as most reactions stop at low temperature. However, adapting this approach to some EPR techniques, necessary for characterization of the intermediates, is challenging, because a capillary of only 0.3 mm

outside diameter has to be filled with the reaction mixture at low temperature and transferred into the spectrometer without warming up. This chapter presents a reproducible method for low temperature preparation and loading of samples into a very high field, 275 GHz, EPR spectrometer without exposing them to heat, thereby preserving the intermediate state. The approach is demonstrated using the small laccase enzyme SLAC during its reaction with molecular oxygen. The enzyme is prepared under nitrogen atmosphere, mixed with an oxygen saturated solution and rapidly frozen. The solution is loaded in a capillary and then into the EPR spectrometer, while maintaining it at low temperature, which keeps the reaction from happening. The method is proved to work and a reproducible spectrum is obtained from different protein batches. The resulting EPR spectra, in combination with conventional EPR techniques and simulations, finally provide a full picture of the electronic structure of SLAC reaction intermediate.

Chapter 5 applies an EPR technique, called DEER, to two supramolecular complexes containing respectively six, eight Cu(II) ions. DEER is typically used for measuring dipolar interactions between two sites, in this case the Cu(II) ions, to determine the distance between them. However, applying DEER to metal ions introduces new difficulties which makes the signal more difficult to obtain. The systems studied here, with multiple Cu(II) ions, also feature multiple interactions, which can lead to artifacts in the measured distances and errors in structure determination. This chapter provides a comprehensive analysis of these challenges, showing that despite weak signals and spectral complications, reliable distances can still be extracted, that agree with modeling and confirm the structure of the molecules under study. The work demonstrates for the first time that complex multi-copper systems can be analyzed using DEER, extending the method's applicability to enzymes and catalysts containing multiple metal centers.

This thesis solves some long standing problems in EPR and provides promising methods to tackle (bio)chemical problems in the future.

Samenvatting

Elektronenspinresonantie (EPR) spectroscopie is al lange tijd een waardevol hulpmiddel voor het bestuderen van biologische systemen. In enzymen – eiwitten die chemische reacties katalyseren – maakt EPR directe inzichten mogelijk in de elektronische en geometrische structuur van het actieve centrum en in het reactiemechanisme. De komst van *site-directed spin labeling* (SDSL), een techniek die spinlabels op specifieke posities van eiwitten aanbrengt, heeft de toepasbaarheid van EPR verder uitgebreid. Dit maakt onderzoek naar eiwitdynamica en structurele conformaties mogelijk, met name dankzij de vooruitgang in EPR-technieken en op maat gemaakte spinlabels. Dit proefschrift onderzoekt de toepassing van EPR-spectroscopie op biologische systemen, waarbij zowel technische als biochemische uitdagingen worden aangepakt.

Hoofdstuk 2 onderzoekt een lang over het hoofd geziene nevenreactie bij SDSL: de dimerisatie van het nitroxide-spinlabel MTSL. Eiwitlabeling wordt uitgevoerd door een mengsel van eiwit- en labeloplossing te incuberen. Onder gangbare labelomstandigheden kunnen twee MTSL-moleculen een dimeer vormen dat de labelingsefficiëntie vermindert en leidt tot verspilling van het spinlabel. Door EPR te combineren met massaspectrometrie – een techniek die het mogelijk maakt om de moleculaire massa en chemische samenstelling van stoffen in oplossing te bepalen – worden de structuur en het vormingsmechanisme van het dimeer opgehelderd. De resultaten tonen aan dat dimerisatie via een disulfidebrug tot een covalent gekoppeld dimeer leidt. Dit proces is onomkeerbaar in de zin dat het label niet kan worden teruggewonnen. Deze nevenreactie, die al decennialang via haar EPR-signaal werd waargenomen maar nooit volledig werd begrepen, is nu duidelijk gekarakteriseerd en verklaard. Dit werpt licht op een hardnekkig probleem binnen het vakgebied van spinlabeling.

Hoofdstuk 3 onderzoekt met behulp van EPR de aggregatie van het eiwit α-Synucleïne (αS), een proces dat in neuronen plaatsvindt en dat in verband wordt gebracht met de ziekte van Parkinson. Er wordt aangenomen dat de toxische deeltjes bij deze ziekte oligomere intermediairen zijn, die zich in de vroege stadia van αS-aggregatie vormen. Deze transiënte en structureel heterogene intermediairen zijn moeilijk te bestuderen. Met behulp van SDSL-EPR werden αS-mutanten op specifieke residuen gelabeld en gevolgd tijdens de aggregatie. Door gebruik te maken van een standaard fluorescentie-assay die doorgaans wordt gebruikt om αS-aggregatie te monitoren, toont deze studie aan dat EPR het mogelijk maakt om de aggregatie *in situ* te volgen en om structurele veranderingen tijdens de vorming van intermediairen tot aggregaten vast te leggen. Dit is bijzonder waardevol, aangezien traditionele assays deze intermediairen niet kunnen detecteren. Deze aanpak vormt een veelbelovende methode om de moleculaire mechanismen van amyloïdevorming te bestuderen en om informatie over de structuur van aggregaten te verkrijgen.

Hoofdstuk 4 richt zich op de uitdagingen die zich voordoen bij het bestuderen van kortlevende reactie-intermediairen in enzymen. Dit zijn overgangstoestanden die ontstaan terwijl een enzym een reactie uitvoert en die soms slechts enkele seconden of zelfs

milliseconden duren, wat de studie ervan uitdagend maakt. *Rapid freeze-quench* (RFQ)-technieken, waarbij een reactiemengsel snel wordt ingevroren, worden vaak gebruikt om deze tussenproducten te vangen en te stabiliseren, aangezien de meeste reacties bij lage temperatuur stoppen. De toepassing van RFQ op bepaalde EPR-technieken is een uitdaging, omdat een capillair van slechts 0,3 mm buitendiameter moet worden gevuld met een reactiemengsel bij lage temperatuur en daarna in een spectrometer moet worden overgebracht zonder opwarming. Dit hoofdstuk presenteert een reproduceerbare methode om monsters bij lage temperatuur voor te bereiden en in een zeer hoog veld EPR-spectrometer (275 GHz) te laden zonder ze bloot te stellen aan warmte, om de vorming van intermediairen te voorkomen. Deze methode wordt aangetoond door gebruik te maken van het *small laccase*-enzym SLAC, dat reageert met zuurstof. Het enzym wordt onder stikstofatmosfeer bereid, gemengd met een zuurstofverzadigde oplossing en snel ingevroren. De oplossing wordt in een capillair overgebracht en vervolgens in de EPR-spectrometer geplaatst, waarbij de temperatuur laag wordt gehouden om verdere reactie te voorkomen. Deze methode blijkt te werken en levert reproduceerbare spectra op uit verschillende batches. De verkregen EPR-data, gecombineerd met conventionele technieken en simulaties, geven uiteindelijk een volledig beeld van de elektronische structuur van het SLAC-reactie-intermediair.

Hoofdstuk 5 behandelt de toepassing van DEER (*double electron-electron resonance*), een EPR-techniek, op twee supramoleculaire complexen die respectievelijk zes en acht Cu(II)-ionen bevatten. DEER wordt met name gebruikt om dipolaire interacties en de afstand tussen twee paramagnetische centra te meten, in dit geval Cu(II)-ionen. Het gebruik van DEER bij metaalionen brengt echter extra uitdagingen met zich mee, onder andere zwakkere signalen en snellere relaxatie. De systemen die in dit hoofdstuk worden bestudeerd, bevatten meerdere Cu(II)-ionen en dus ook meerdere interacties, wat kan leiden tot artefacten in de gemeten afstanden en fouten in structuurbepaling. Dit hoofdstuk biedt een uitgebreide analyse van deze uitdagingen en toont aan dat, ondanks zwakke signalen en spectrale complicaties, betrouwbare afstanden kunnen worden verkregen die overeenkomen met structurele modellen. Het onderzoek toont voor het eerst aan dat complexe multi-kopersystemen met DEER kunnen worden geanalyseerd, en dat de toepasbaarheid van deze methode kan worden uitgebreid naar enzymen en katalysatoren met meerdere metaalcentra.

Dit proefschrift lost enkele langbestaande problemen in de EPR op en biedt veelbelovende methodes voor de studie van (bio)chemische problemen in de toekomst.

Acknowledgements

First and foremost, I would like to thank my supervisor, Dr. Martina Huber, for giving me the opportunity to pursue my PhD in her group. I am grateful for her guidance, feedback and support throughout the years, without which this thesis would not have been possible.
I thank Prof. Edgar Groenen for the long and fruitful scientific discussions, and for guiding me through the interpretation of high-frequency EPR spectra. I also thank Prof. Peter Gast for training me in the use of the high-field spectrometer and for always being available when help was needed.
This work would not have been achievable without the exceptional support of the technical staff at Leiden University. I am deeply grateful to the Electronics Department — especially Harry Visser, Renè Overgauw, and Peter Veldhuizen — for their constant assistance and availability. Without their expertise and dedication, the spectrometers would not have functioned properly, and much of the work in this thesis would not have been possible. A special thanks goes to Jos Disselhorst, whose expertise with the J-band spectrometer was essential and whose passion for microwave technology was truly inspiring. I also extend my sincere thanks to the Fine Mechanics Department, in particular Harmeen van der Meer, for his valuable work on the J-band spectrometer insert. Many of the protein samples measured in this thesis were prepared by Lionel Ndamba, who was always ready to produce a new batch whenever I asked. Without his contribution, this work would have taken twice as long. These years also required the use of quite some liquid helium and nitrogen, which were always available — even on short notice — thanks to Wilfred van der Geest.
I am also very grateful to Henriette van Leeuwen, who helped me find a house when I first arrived and patiently guided me through all bureaucratic and administrative matters whenever needed.
Over the years, I had the pleasure of several fruitful collaborations. I wish to thank Ehider, Anna and Sylvestre Bonnet for the interesting cobalt samples they provided. Thanks also to Felix de Zwart, Joost Reek, and Bas de Bruin for letting me use their spectrometer when ours were down and for providing the copper cages — a fascinating sample that led to the results presented in Chapter 5. I am also grateful to Mark Overhand, Karthick Gupta, and Rene Dekkers for their help in understanding the reaction studied in Chapter 2, and for the hours spent interpreting complex NMR spectra. Thanks to Anne Wentinck and Djim de Ridder for teaching me about amyloid disaggregation and the interesting project we started — I wish you great success in the experiments to come!
Although I was the last PhD student remaining on the 8th floor, it was truly an honor to be part of the MONOS group. The daily interactions with Michel Orrit taught me a great deal — not only through our conversations, but also through observing his group and listening to his insights and remarks during talks and conferences. I especially want to thank Robert, Jacco, Theo, Pryianshi, Subhasis, Jacqui, Nasrin, Xuxing, Patrick, Eduardo and Amin for their company and discussions during lunch and coffee breaks. Thanks also to Liru, who was a wonderful colleague in the biochemistry lab.

Over these four years, I had the pleasure of supervising several exceptional students and guests who greatly contributed to the projects. I warmly thank Luciana, Resi, David, Nina, Ryan, Claudia, and Fabio.
Finally, I would like to express my deepest gratitude to my family for their unwavering support and encouragement throughout this journey.

Curriculum Vitae

Leonardo Passerini

Leonardo Passerini was born on May 17th, 1994, in Trento, Italy.

He obtained a BSc in Biology (2017) and an MSc in Industrial Biotechnology (2019) from the University of Padua. His Master's thesis was titled *"Biochemical and Spectroscopic Approach for the Study of Iron Binding to Frataxin."*

In 2020, he held a research grant at the Department of Chemistry, University of Padua.

From 2021 to 2025, he carried out his PhD in Physics in the MONOS group at Leiden University. His PhD thesis was titled *"Electron Paramagnetic Resonance Approaches to Study Biologically Relevant Reactions: Examples from Amyloid Aggregation to Enzymes."*

In 2025, he joined the Laboratory of Molecular Magnetism at the University of Florence as a postdoctoral researcher.

List of Publications

[1] D. Doni, **L. Passerini**, G. Audran, S.R.A. Marque, M. Schulz, J. Santos, P. Costantini, M. Bortolus, D. Carbonera, Effects of Fe2+/Fe3+ Binding to Human Frataxin and Its D122Y Variant, as Revealed by Site-Directed Spin Labeling (SDSL) EPR Complemented by Fluorescence and Circular Dichroism Spectroscopies, International Journal of Molecular Sciences, 2020, *21*, 9619. https://doi.org/10.3390/ijms21249619.

[2] D. Doni, G. Rigoni, E. Palumbo, E. Baschiera, R. Peruzzo, E. De Rosa, F. Caicci, **L. Passerini**, D. Bettio, A. Russo, I. Szabò, M.E. Soriano, L. Salviati, P. Costantini, The displacement of frataxin from the mitochondrial cristae correlates with abnormal respiratory supercomplexes formation and bioenergetic defects in cells of Friedreich ataxia patients, The FASEB Journal 35(3) (2021) e21362.

[3] D.M. Klein, **L. Passerini**, M. Huber, S. Bonnet, A Stable Alkylated Cobalt Catalyst for Photocatalytic H2 Generation in Liposomes, ChemCatChem 14(20) (2022) e202200484.

[4] E. Zurlo, **L. Passerini**, P. Kumar, M. Huber, In Situ Continuous Wave Electron Paramagnetic Resonance Investigation of the Amyloid Aggregation of Parkinson's Protein Alpha-Synuclein—the Second Spin-Label Position, Applied Magnetic Resonance 53(7) (2022) 1133-1150.

[5] E.O. Bobylev, **L. Passerini**, F.J. de Zwart, D.A. Poole, S. Mathew, M. Huber, B. de Bruin, J.N.H. Reek, Pd12MnL24 (for n = 6, 8, 12) nanospheres by post-assembly modification of Pd12L24 spheres, Chemical Science 14 (2023) 11840-11849.

[6] E.A. Polanco, L.V. Opdam, **L. Passerini**, M. Huber, S. Bonnet, A. Pandit, An artificial metalloenzyme that can oxidize water photocatalytically: design, synthesis, and characterization, Chemical Science 15(10) (2024) 3596-3609.

[7] M. Saberi, R. Dekkers, **L. Passerini**, M. Huber, M. Overhand, M. Ubbink, Terminal spin labeling of xylotriose strongly affects interactions in the active site of xylanase BcX, Journal of Biomolecular NMR 79(2) (2025) 99-113.